BioMed Research International

Biometrics and Biosecurity 2014

Guest Editors: Tai-hoon Kim, Sabah Mohammed, Wai-Chi Fang, and Carlos Ramos

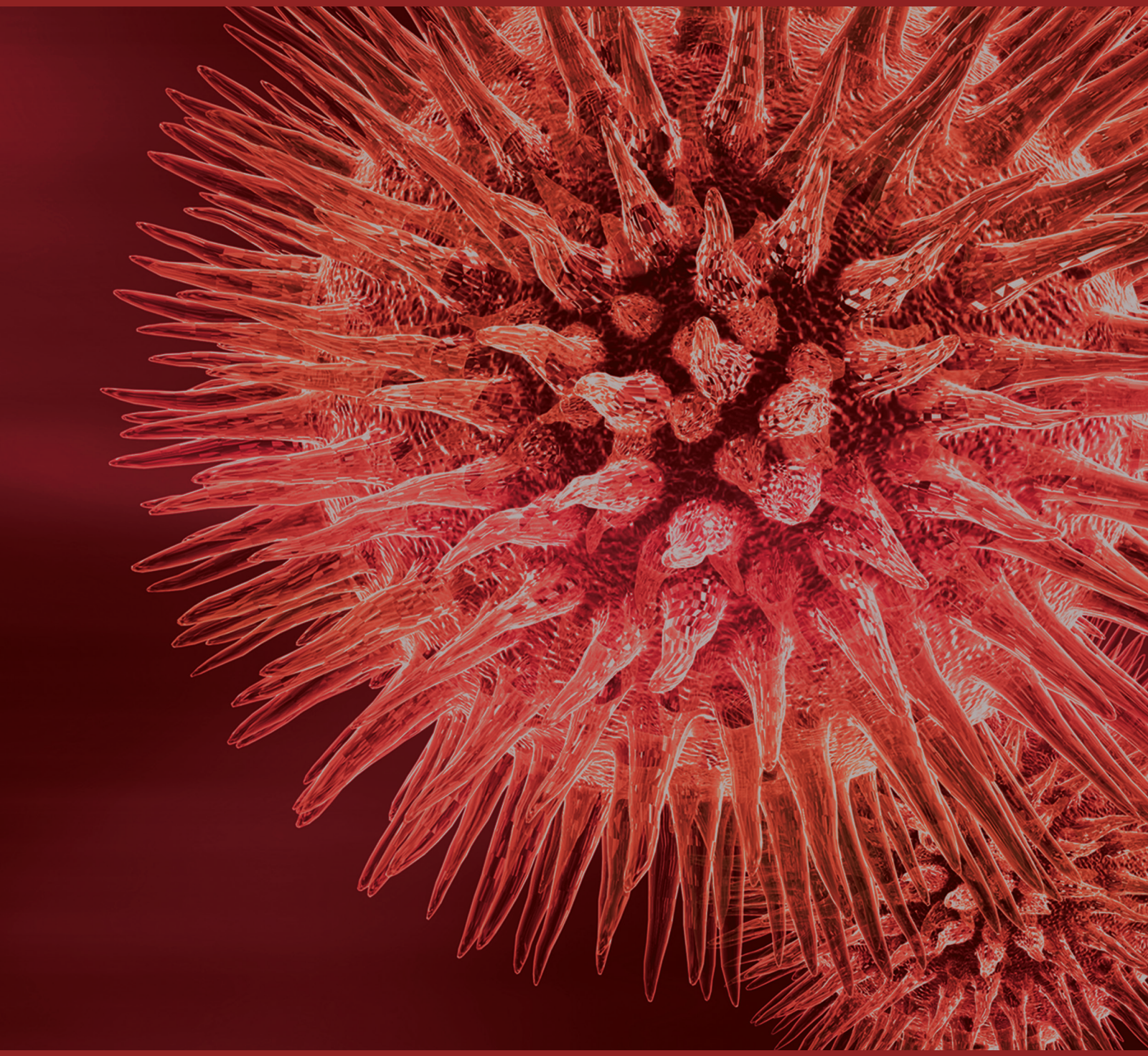

Biometrics and Biosecurity 2014

BioMed Research International

Biometrics and Biosecurity 2014

Guest Editors: Tai-hoon Kim, Sabah Mohammed,
Wai-Chi Fang, and Carlos Ramos

Contents

Hindawi Publishing Corporation
BioMed Research International
Volume 2015, Article ID 812697, 2 pages
http://dx.doi.org/10.1155/2015/812697

Editorial
Biometrics and Biosecurity 2014

Tai-hoon Kim,[1] Sabah Mohammed,[2] Wai-Chi Fang,[3] and Carlos Ramos[4]

[1] *University of Tasmania, Centenary Building, Room 350, Private Bag 87, Hobart, TAS 7001, Australia*
[2] *Lakehead University, 955 Oliver Road, Thunder Bay, ON, Canada P7B 5E1*
[3] *National Chiao Tung University, 1001 University Road, Hsinchu 300, Taiwan*
[4] *ISEP/IPP, Rua Dr. António Bernardino de Almeida 431, 4200-072 Porto, Portugal*

Correspondence should be addressed to Tai-hoon Kim; taihoonn@empal.com

Received 15 February 2015; Accepted 15 February 2015

This issue contains several articles that come from various countries, among which we mention German, Brazil, Korea, and Japan.

Biometrics and Biosecurity focused on the various aspects of advances in biometrics and biosecurity. This special issue will provide a chance for academic and industry professionals to discuss recent progress, problems, and solutions in the area of biometrics and its application, biosecurity measures, and biosafety protocols, including development, implementation, strategies, and policies.

As a novel approach to perform user authentication, authors proposed a multimodal biometric system that uses faces and gestures obtained from a single vision sensor in the paper "A Multimodal User Authentication System Using Faces and Gestures." Unlike typical multimodal biometric systems using physical information, the proposed system utilized gesture video signals combined with facial images.

The purpose of the paper "Quantification of Hepatorenal Index for Computer-Aided Fatty Liver Classification with Self-Organizing Map and Fuzzy Stretching from Ultrasonography" was to show that HRI is an important and informative diagnostic attribute in multiclass fatty liver classification because of such quantification. This encouraged authors to develop reliable automatic diagnostic software if it is combined with other sets of useful textual or statistical features and other powerful machine learning algorithms in the future.

The aim of the paper "Towards a Food Safety Knowledge Base Applicable in Crisis Situations and Beyond" was to verify that a framework established for efficient and transparent conduction of exposure assessments in the food sector could also be applied in case of bio- and agroterroristic crisis situations. For this, data and models on tenacity of highly pathogenic agents were collected and applied in sample scenarios together with knowledge on relevant food production processes.

In "Establishing Standards for Studying Renal Function in Mice through Measurements of Body Size-Adjusted Creatinine and Urea Levels" authors showed that creatinine clearance measurements should be adjusted according to the body surface area, which was calculated based on the weight and length of the animal. Authors' findings will facilitate standardization and optimization of methodology as well as understanding of renal and other biochemical data obtained from mice.

In the paper "Biometrics Analysis and Evaluation on Korean *Makgeolli* using Brainwaves and Taste Biological Sensor System" authors conducted sensory evaluation, whereas a maximum of nine points were accumulated by purchasing eight types of rice wine. The contribution of this paper was to overcome the disadvantages of the sensory evaluation with the usage of the suggested taste biological sensor system.

In the paper "A Multi-layer secure Biomedical Data Management System for Remotely Managing a Very Large Number of Diverse Personal Healthcare Devices" a multilayered remote PHD management system for a very large number of PHDs was proposed. Some experiments, including the stress test, were carried out to show that the system proposed in this paper performed very well even when a very large number of PHDs were 30 used.

Acknowledgments

Achieving such high quality of papers would have been impossible without the huge work that was undertaken by the Editorial Board members and External Reviewers. We take this opportunity to thank them for their great support and cooperation.

Tai-hoon Kim
Sabah Mohammed
Wai-Chi Fang
Carlos Ramos

Hindawi Publishing Corporation
BioMed Research International
Volume 2015, Article ID 941053, 17 pages
http://dx.doi.org/10.1155/2015/941053

Research Article

A Multilayer Secure Biomedical Data Management System for Remotely Managing a Very Large Number of Diverse Personal Healthcare Devices

KeeHyun Park and SeungHyeon Lim

Keimyung University, Daegu 704-701, Republic of Korea

Correspondence should be addressed to KeeHyun Park; khp@kmu.ac.kr

Received 12 September 2014; Accepted 2 January 2015

Academic Editor: Sabah Mohammed

In this paper, a multilayer secure biomedical data management system for managing a very large number of diverse personal health devices is proposed. The system has the following characteristics: the system supports international standard communication protocols to achieve interoperability. The system is integrated in the sense that both a PHD communication system and a remote PHD management system work together as a single system. Finally, the system proposed in this paper provides user/message authentication processes to securely transmit biomedical data measured by PHDs based on the concept of a biomedical signature. Some experiments, including the stress test, have been conducted to show that the system proposed/constructed in this study performs very well even when a very large number of PHDs are used. For a stress test, up to 1,200 threads are made to represent the same number of PHD agents. The loss ratio of the ISO/IEEE 11073 messages in the normal system is as high as 14% when 1,200 PHD agents are connected. On the other hand, no message loss occurs in the multilayered system proposed in this study, which demonstrates the superiority of the multilayered system to the normal system with regard to heavy traffic.

1. Introduction

As awareness and interest in health issues have become widespread and the number of elderly persons has grown over recent years, the concept of healthcare has shifted from disease diagnosis and treatment to disease prevention. As a result, the utilization of Personal Healthcare Devices (PHDs) has increased substantially [1–8]. Moreover, due to the rapid technical development of various systems and the advent of the ubiquitous era, it is expected that PHD utilization will continue to increase.

However, the proliferation of PHDs will bring with it a new problem, effective remote device management for a very large number of PHDs. As one of several types of mobile healthcare devices, PHDs need to be managed closely and accurately. There are many reasons to have PHDs managed by systems or healthcare organizations. First of all, PHDs are healthcare devices, and poor management of PHDs could cause very serious healthcare problems. Secondly, most PHD users are elderly patients who may have problems handling their PHDs skillfully. Therefore, it is most appropriate for healthcare organizations or healthcare systems to take care of PHD management work for PHD users. However, when the number of PHDs to be managed is very large, another problem occurs. This is the fact that there would most likely be a bottleneck problem [9, 10] in a PHD management system, which in turn would cause a serious performance problem. In addition, whenever biomedical data is processed, security issues related to the data inevitably arise. The biomedical data of a user must be securely protected and cannot be accessed/altered by an unauthorized person, as this is a serious invasion of privacy.

Therefore, in this paper, multilayer secure biomedical data management architecture for managing a very large number of diverse personal health devices is proposed. The system has the following characteristics: first, the system is designed in a hierarchical fashion to lessen the bottleneck problem that might be caused by requests from a very large number of diverse PHDs. Second, the system supports international standard communication protocols to achieve

interoperability. Two protocols, ISO/IEEE 11073 protocol and OMA DM (device management) protocol, which were proposed as international standard communication protocols for PHD communication and remote device management, respectively, are extended and implemented in the system. Third, the system is integrated in the sense that both a PHD communication system and a remote PHD management system work together as a single system. Finally, the system proposed in this paper provides user/message authentication processes to securely transmit biomedical data measured by PHDs based on the concept of a biomedical signature.

Some experiments, including the stress test, were conducted to show that the system proposed in this study performs very well even when a very large number of PHDs are used. Moreover, after locating the bottlenecks, it was found that there was still room to improve the system performance, and two modifications of the system were performed in this study, database division and delayed write. It is found that the system performance was much improved after these two modifications were applied.

Moreover, message loss is considered to be a very serious issue in health related systems such as the one discussed in this study. Through the experiments, it is found that the loss ratio of the ISO/IEEE 11073 messages in the normal system (e.g., the system without any gateways) is quite high in heavy traffic, while no message loss occurs in the multilayered system proposed in this study, which demonstrates the superiority of the multilayered system to the normal system in regard to heavy traffic.

The remainder of this paper is organized as follows. Section 2 describes some related studies, Section 3 explains the multilayered remote PHD management system for a very large number of PHDs proposed in this paper, Section 4 discusses security considerations for the system, and Section 5 shows the results of some experiments using the system constructed in this study, along with a discussion based on the results. In addition, two modification schemes to improve performance are explained. Finally, Section 6 draws some conclusions and discusses some possible directions for future research.

2. Related Studies

2.1. ISO/IEEE Communication Protocol. The ISO/IEEE 11073 communication protocol [3–5] was proposed by an ISO/IEEE committee as an international standard to provide interoperability for health and medical services in ubiquitous environments (especially using PHDs). PHDs are small-sized healthcare devices which can be used at home without the direct intervention of medical personnel. Examples of PHDs are physical activity monitors, blood pressure monitors, glucose meters, and medication dispensers [3–6, 8]. A PHD-related system defined by ISO/IEEE consists of agents and managers. An agent is a program installed in the PHD. A manager is a program installed in a server (e.g., a laptop computer or a PC) which receives/processes biomedical data from PHDs to provide a user's health information to medical personnel. The sequence of the ISO/IEEE 11073 communication protocol is shown in Figure 1 [3]. The sequence of the protocol consists of session establishment ("Association Request" and "Association Response" in the figure), data transmission, and session release ("Association Release Request" and "OMA DM communication protocol Association Release Response" in the figure).

2.2. OMA DM Communication Protocol. The OMA DM communication protocol was proposed by OMA (Open Mobile Alliance) as an international standard for the remote management of mobile devices [11]. Since then, the protocol has become used very widely [12–15]. However, attempts to apply the protocol to manage PHDs have been rare. An OMA DM-related system consists of clients (DM agents) and servers (DM managers). A DM agent, installed in a mobile device, executes device management operations issued by a DM manager. Objects managed by DM agents or DM managers are grouped together to form DM trees, whose nodes are called management objects. The sequence of the original OMA DM communication protocol is shown in Figure 2 [11]. The sequence of the protocol consists of a setup phase and a management phase. In the setup phase, authentication and device (agent) information are exchanged between a DM agent and a DM manager. In the management phase, management commands and their status reports are exchanged.

2.3. Integrated Gateway for PHDs. In [16], an integrated gateway for diverse PHDs was proposed, as shown in Figure 3. This gateway receives measurements from diverse PHDs and conveys them to a remote monitoring server. It provides two kinds of transmission modes: immediate transmission and integrated transmission. The former mode operates if a measurement exceeds a predetermined threshold, or in the event of an emergency. In the latter mode, the gateway retains the measurements instead of forwarding them. When the reporting time comes, the gateway extracts all the stored measurements, integrates them into one message, and transmits the integrated message to the monitoring server. In this study, only three PHDs (e.g., an activity monitor, a medication dispenser, and a pulse oximeter) were used, and therefore there is no need to be concerned about the bottleneck problems that can create severe degradations in system performance. Furthermore, the study did not work on remote PHD management.

In [17], a message processing scheme for an integrated PHD gateway in an integrated PHD management system that serves diverse PHDs is proposed. On receiving the ISO/IEEE-based health messages generated by PHDs, the integrated PHD gateway performs some integration work to send an integrated message to the integrated PHD management server. Also, when the integrated PHD gateway receives the OMA DM-based PHD management messages from the server, the gateway performs some separation work to send the messages to the related PHDs separately.

Located between PHDs and the integrated PHD management server, integrated PHD gateways transform the ISO/IEEE 11073 based messages into OMA DM based messages and vice versa. The ISO/IEEE 11073 communication protocol is used to transmit health messages measured by

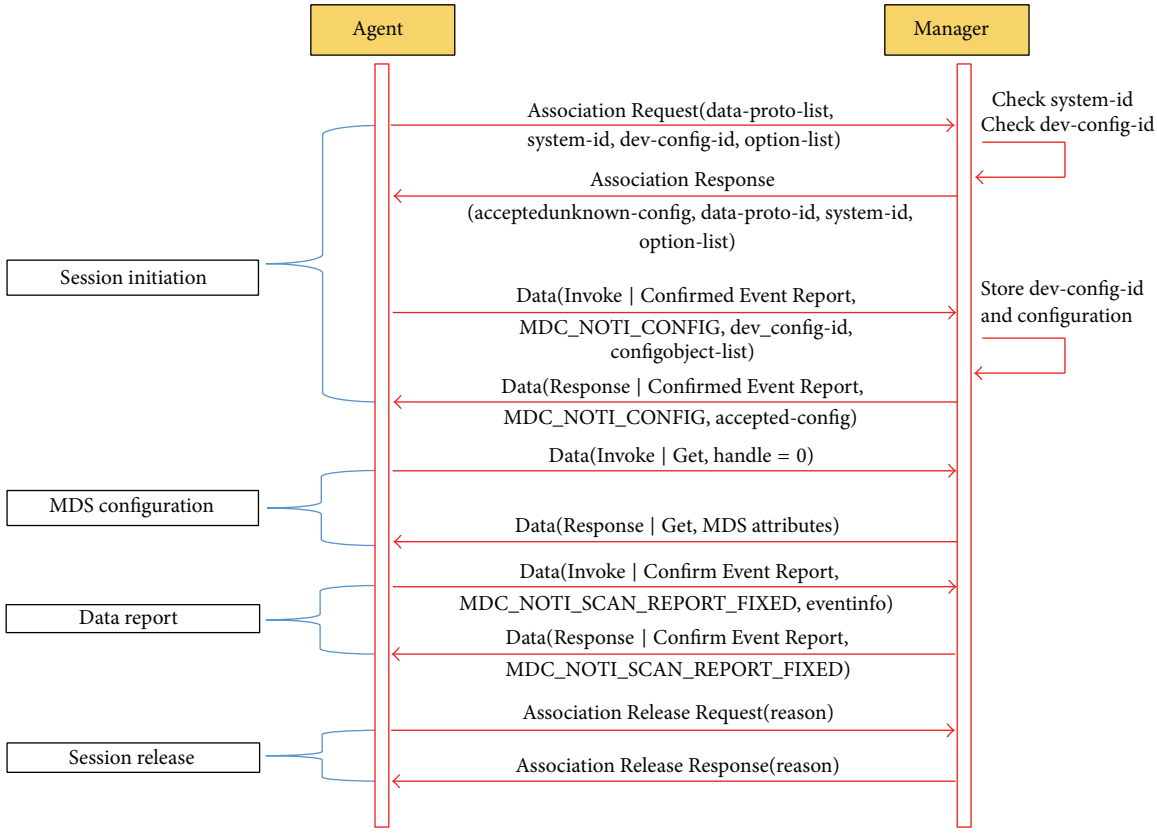

Figure 1: ISO/IEEE 11073 communication protocol sequence.

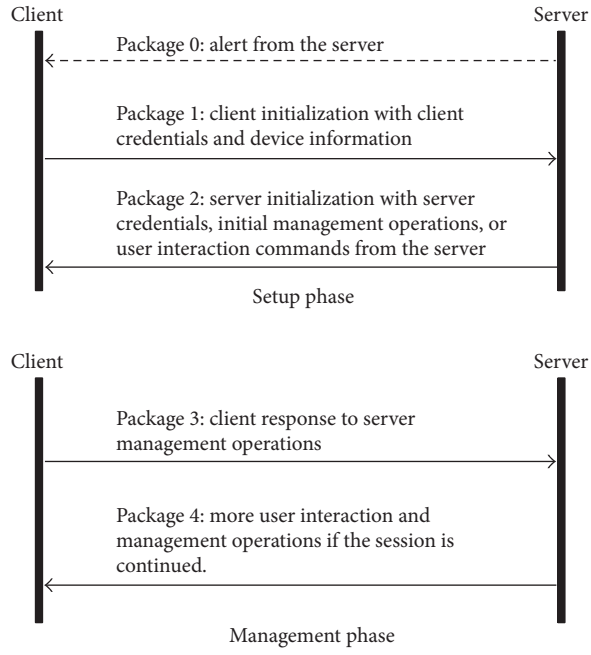

Figure 2: OMA DM communication protocol sequence.

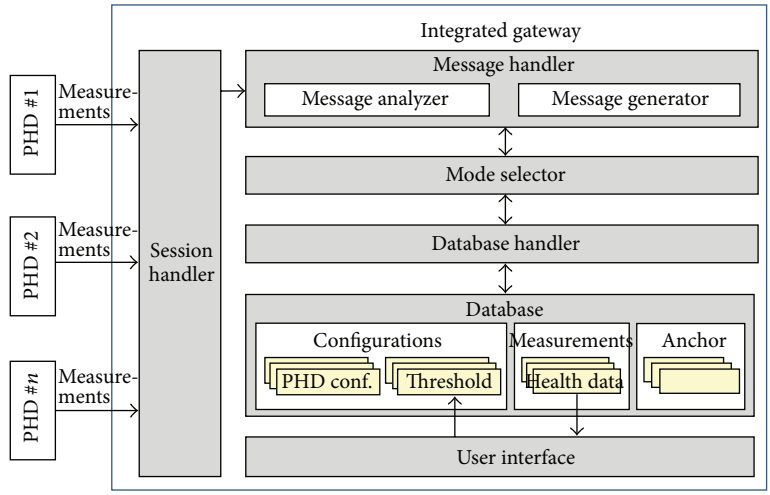

Figure 3: Structure of the integrated gateway in [16].

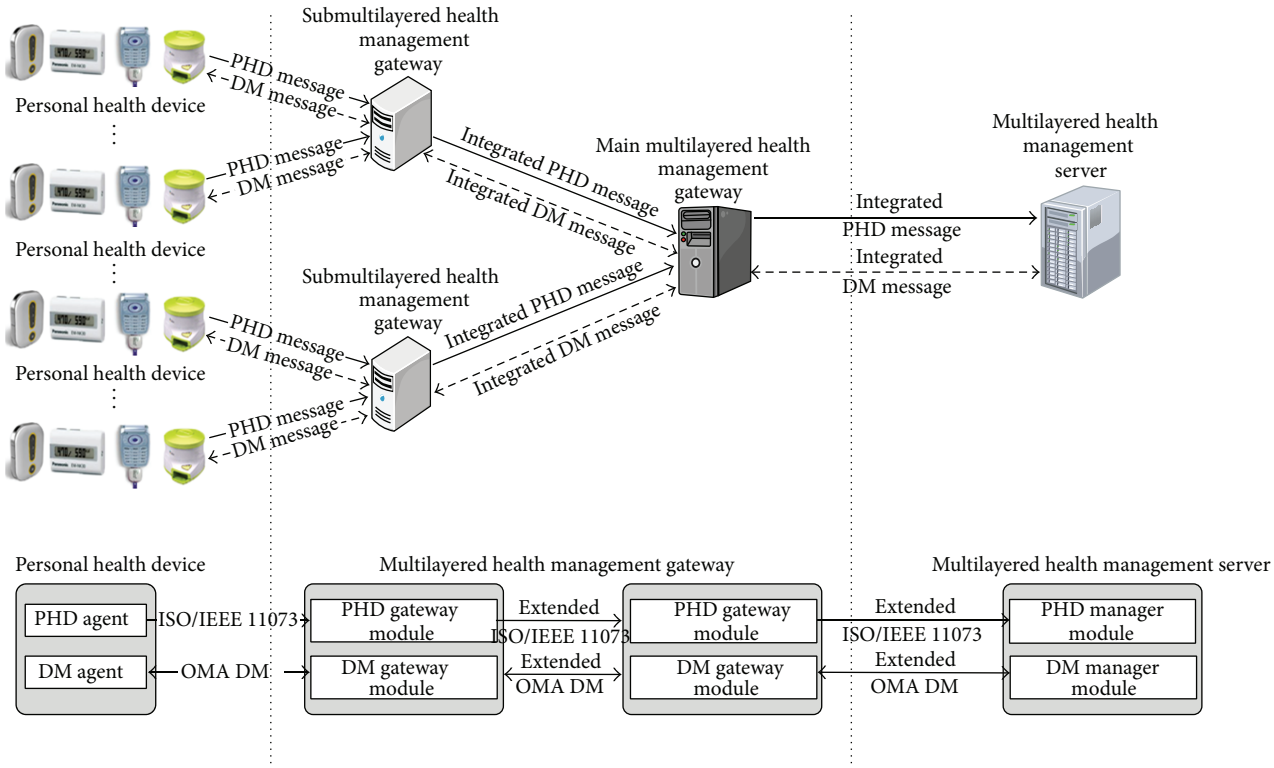

Figure 4: Structure of secure biomedical data management system with a very large number of PHDs.

a PHD to the integrated PHD management server via the related integrated PHD gateway. The OMA DM communication protocol is used to transmit device management commands issued by the integrated PHD management server to a PHD via the related integrated PHD gateway. This study also used only three PHDs, and therefore there is no need to be concerned about the bottleneck problems that can create severe degradations in system performance. Therefore, the system proposed in [15] may not be used in a scenario in which there are a very large number of PHDs. A single gateway system was used in this study.

3. Secure Biomedical Data Management System

3.1. System Overview. Figure 4 shows the secure biomedical data management system for a very large number of PHDs

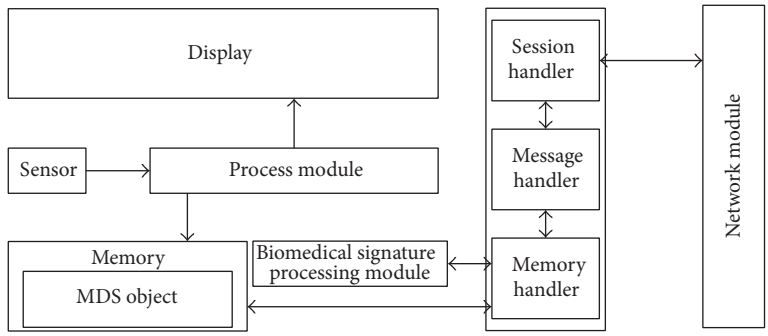

Figure 5: Structure of the PHD and the PHD agent.

that is proposed in this paper. The secure biomedical management system has the following components:

(i) PHD and PHD agent: as defined by ISO/IEEE 11073, a PHD agent, installed in a PHD, captures a user's biomedical signals, processes the signals to form health data, and sends the data to the multilayered health information server, via the multilayered health management gateways related to the PHD. In addition, the PHD agent executes remote management commands issued by the multilayered health information management server via the gateways. Then, the PHD agent sends status reports to the server via the gateways. The health data and health information are delivered in ISO/IEEE 11073 messages, while the management commands and status reports are delivered in OMA DM messages. In this study, PHD agents can handle not only ISO/IEEE 11073 messages but also OMA DM messages.

(ii) Multilayered health management gateways and their programs: these gateways receive health data or status reports from PHD agents and process them to produce health/management information in order to send the information to the server. In addition, they receive remote management commands to send to the PHD agents from the server. To reduce communication traffic, the gateways do not try to send the data as soon as the data arrives. The gateways accumulate the data from the PHD agents for a while to integrate the data in order to form a single (extended) ISO/IEEE 11073 or OMA DM message. Also, the gateways disintegrate a single (extended) ISO/IEEE 11073 or OMA DM message, received from the server, to distribute separate messages to individual PHD agents. In Figure 4, a 2-layered gateway system is presented, but the system is designed and constructed to support more than 2 layers of the gateways to distribute heavy traffic loads over the entire system when the number of active PHD agents at once is very large. In this study, the ISO/IEEE 11073 protocol is extended in the sense that the concept of the gateway is added to service a very large number of PHDs without causing a severe degradation in system performance.

(iii) Multilayered health management server and its programs: this server receives health information/status reports from the PHD agents via the gateways and processes them for medical personnel. The server also issues remote management commands for PHD agents. The management commands implemented in this study are ADD, REPLACE, and DELETE.

3.2. PHD Agent. As mentioned earlier, the PHD agent in the PHD captures a user's health data to send to the server via gateways. As shown in Figure 5, the PHD agent consists of a session handler, a message handler, a memory handler, and a biomedical signature processing module.

(i) Session handler establishes/releases a communication session between a PHD agent and a gateway to which the agent is connected, using the network module in the PHD.

(ii) Message handler creates ISO/IEEE 11073 messages using health data stored in the memory of the PHD and sends the messages to the session handler.

(iii) Memory handler accesses health data from the memory of the PHD for the message handler. It also stores new health data in the memory.

(iv) Biomedical signature processing module generates a hash value based on new biomedical data of a user measured by a PHD. The hash value will be used by the health management server to authenticate the new biomedical data.

Figure 6 shows the sequence diagram of messages in a PHD agent.

3.3. DM Agent. Figure 7 shows the structure of the DM agent of the PHD. The DM agent receives remote management commands from the server via the gateways, executes the commands, and sends status reports to the server. The DM agent consists of a session handler, a message handler, a message parser, a message generator, and a tree-manager.

(i) Session handler is similar to the session handler of the PHD agent.

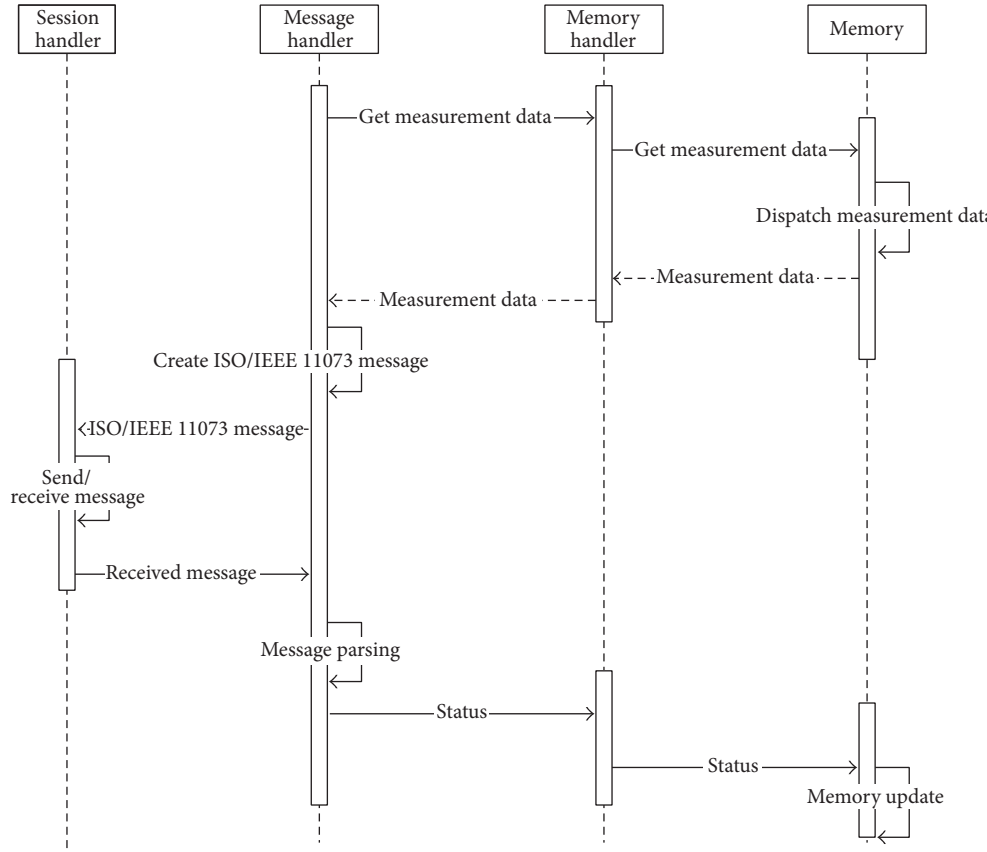

Figure 6: Sequence diagram of messages in a PHD agent.

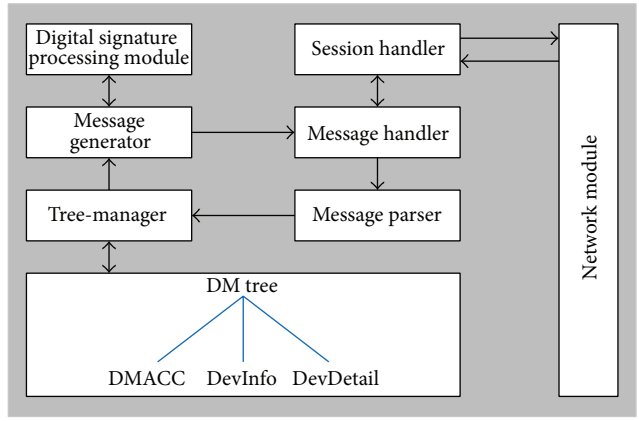

Figure 7: Structure of the DM agent.

(ii) Message handler receives OMA DM messages from the session handler to execute remote management commands.

(iii) Memory handler accesses a DM tree from the memory of the PHD for the message handler. It also stores an updated DM tree in the memory.

(iv) Message parser receives OMA DM messages from the message handler and parses the messages to extract remote management commands to execute.

(v) Tree-manager updates the DM tree in the DM agent according to the results of the remote command execution.

(vi) Message generator generates OMA DM messages to include the results/status of the remote command execution. The generated OMA DM messages (or packages) are sent to the server. Figure 8 shows the structure of the package templates for OMA DM messages. All of the fields except for the dark colored

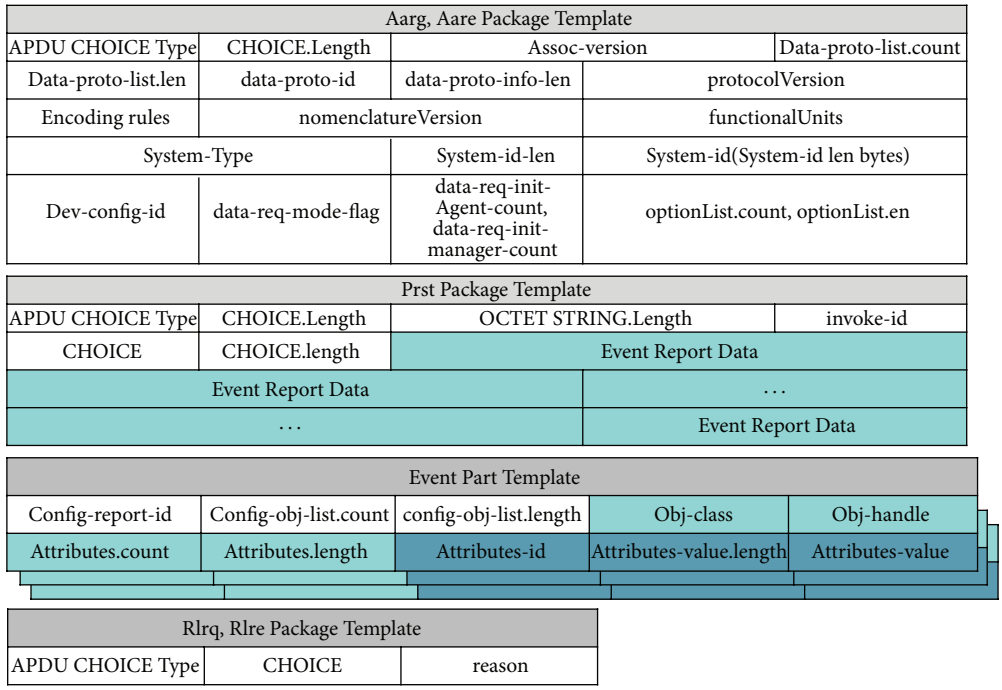

Figure 8: Structure of package templates.

fields remain unchanged during the session. Therefore, when a message is generated, it uses a template to reduce message generation time.

Figure 9 shows the sequence diagram of messages in a DM agent.

3.4. Multilayered Health Management Gateway. Figure 10 shows the structure of the multilayered health management gateway. The gateway consists of 2 modules: a PHD gateway module and a DM gateway module.

3.4.1. PHD Gateway Module. The PHD gateway module receives separate ISO/IEEE 11073 messages from the PHD agents of the PHDs. The gateway updates its own database to store measured health data and integrates the data into a single integrated message to send to the gateway in the higher layer or the server. On the other hand, when the gateway module receives an integrated ISO/IEEE 11073 messages from the gateway in the higher layer or the server, the gateway module updates its own database and disintegrates the message into several separate ISO/IEEE 11073 messages to send to PHDs or the gateways in the lower layer. The gateway module consists of a session handler, a message handler, and a database handler.

(i) Session handler controls sessions between the PHD and the gateway in the higher layer or the server.

(ii) Message handler processes ISO/IEEE 11073 messages received from the PHD or the gateway in the lower layer or the server and generates an integrated ISO/IEEE 11073 message to send to the gateway in the higher layer or the server. It is important to note that the messages transmitted have many parts in common. Therefore, when a message is generated, it uses a template to reduce message generation time.

(iii) Database handler accesses/stores health data from/to the database. The gateway identifies the MDS (Medical Device System) configuration of the connected PHD by examining the Configuration ID and the System ID, which specifies the characteristics of the PHD. According to the MDS configuration, the received health data is classified in the database.

Figures 11(a) and 11(b) show the sequence diagrams of message reception (a) and message integration (b) in a PHD gateway.

3.4.2. DM Gateway Module. Upon receiving the separate OMA DM messages from the PHDs or the gateways in the lower layer, the DM gateway module integrates the received messages into a single integrated message, updates its own DM tree, and sends the message to the gateway in the higher layer or the server. On the other hand, when the DM gateway module receives an integrated OMA DM message from the gateway in the higher layer or the server, the gateway module updates its own DM tree and disintegrates the message into several separate OMA DM messages to send to PHDs or the gateways in the lower layer. The gateway module consists of a session handler, a tree-manager, and a database handler. The components of the DM gateway module are very similar to those of the DM agent, and thus an explanation of these will be omitted.

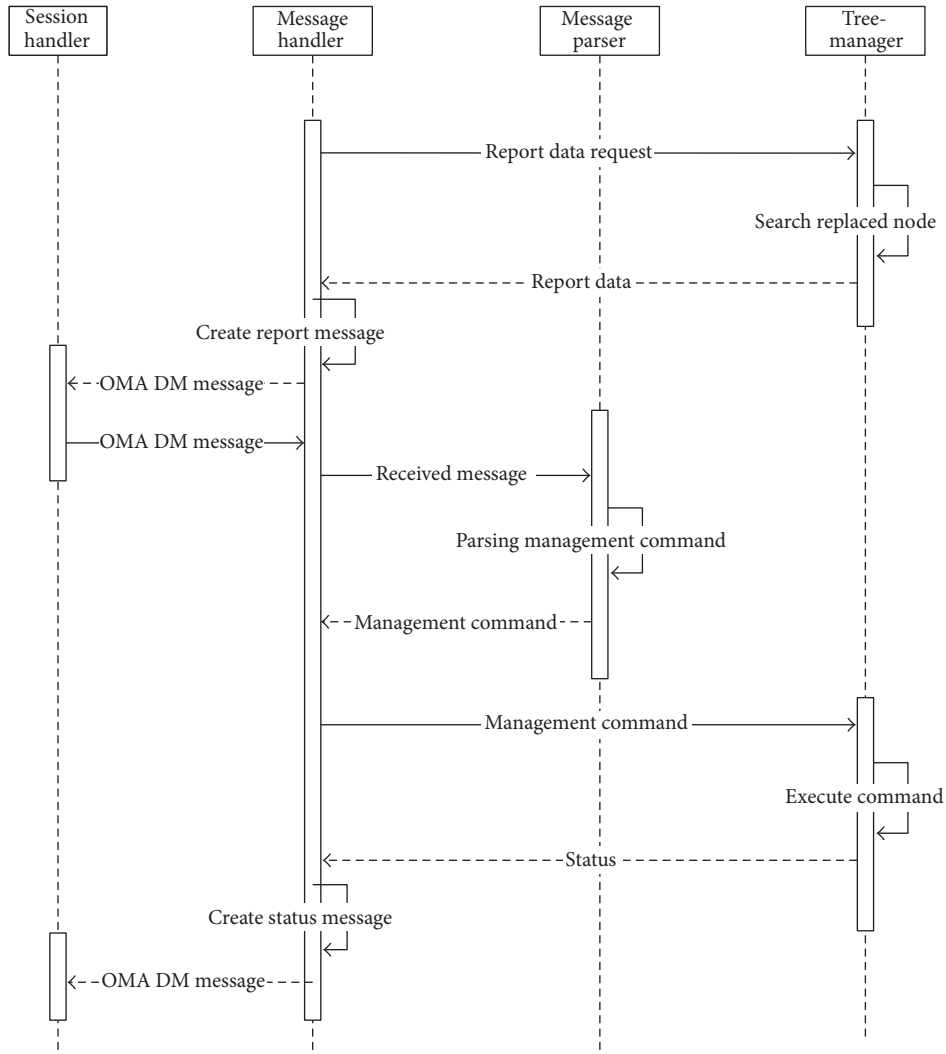

Figure 9: Sequence diagram of messages in a DM agent.

Figure 12 shows the sequence diagram of messages in a DM gateway.

3.5. Multilayered Health Management Server. Figure 13 shows the structure of the multilayered health management server. Medical personnel or system managers monitor a PHD user's health information, issue remote management commands, and receive reports through the server. The components of the server are very similar to those of the gateway, and thus an explanation of these will be omitted.

Figures 14 and 15 show the sequence diagrams in a PHD manager module and a DM manager module in the server, respectively.

4. Security Considerations

4.1. Biomedical Signature. Whenever biomedical data is processed, security issues related to the data inevitably arise. In this paper, the concept of the biomedical signature is proposed to address this issue. The biomedical signature is used to authenticate users as well as messages transmitted between a PHD and a monitoring server. The biomedical status of a user is characterized by the user's biomedical signature. The biomedical signature of a user is a hash value calculated from the highest values and the lowest values of the biomedical data, which is obtained by the PHDs the user carries for a certain period of time.

In other words, BM-signature (n, t), the biomedical signature of user n during most the recent t months, is defined as follows.

BM-signature (n, t) = hash_auth(a string of (Hbp, Lbp, Hgc, Lgc,. . ., Hk, Lk)), where hash_auth is a hash function for authentication. Hk (Lk) is the highest (the lowest) value of k-type biomedical data of user n measured in the recent t months using his/her PHD, while bp and gc represent blood pressure and glucose, respectively. For example, let us assume that the highest and the lowest values of biomedical data of user n during the last one month are as follows.

The highest (lowest) values of blood pressure, glucose, pulse rate, and body fat percentage are 120 (80), 110 (70),

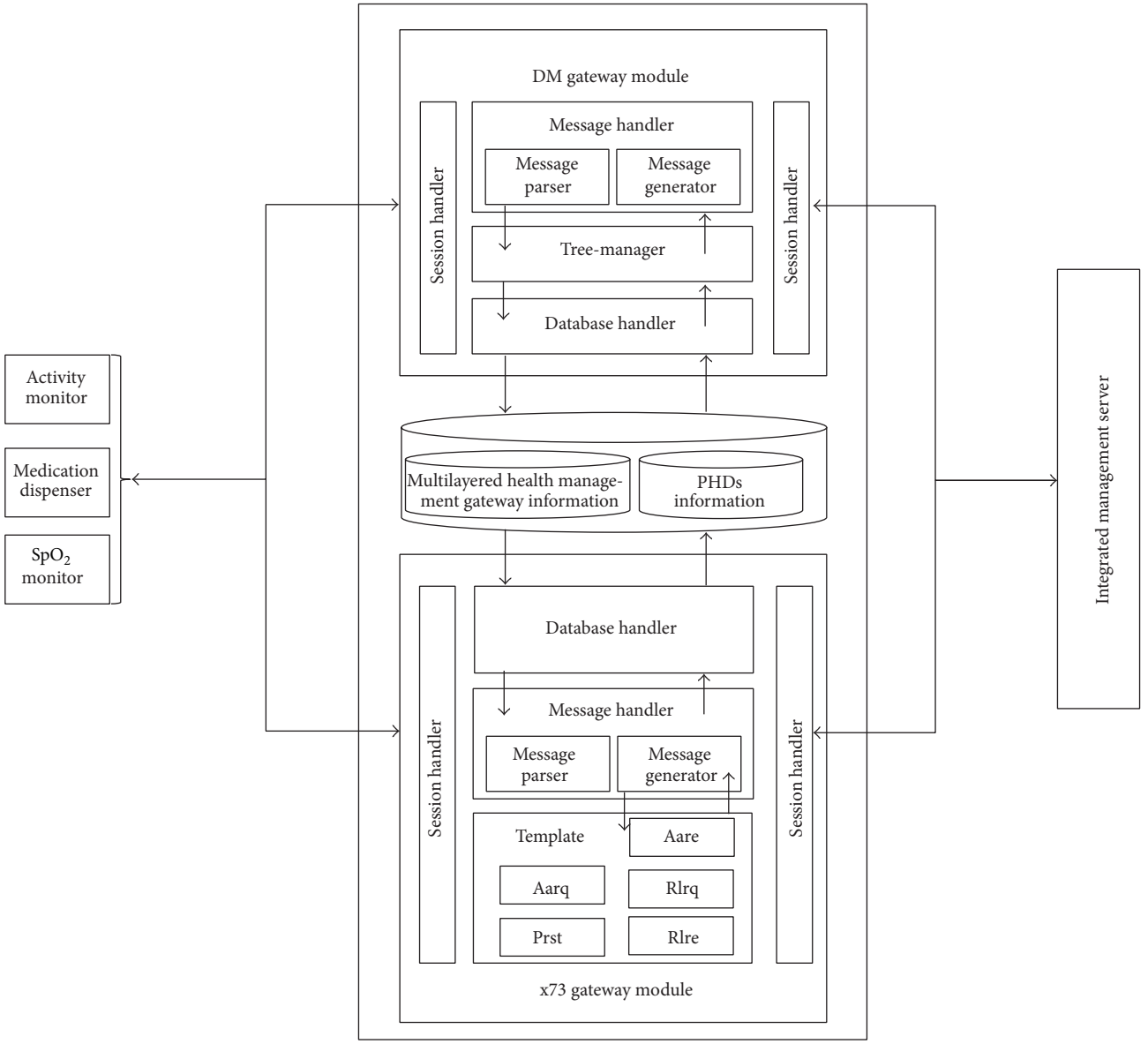

Figure 10: Structure of the multilayered health management gateway.

100 (60), and 20 (15), respectively. SHA512 [18] is assumed to be used for a hash function.

Then BM-signature $(n, 1)$ = SHA512(120, 80, 110, 70, 100, 60, 20, 15).

Then, the BM-signature proposed in this paper for authentication has the following properties:

(i) Since the possibility of having the same biomedical data between any two users measured during the recent time interval is very low, BM-signature (n, t) is almost unique and represents very well the characteristics of the biomedical data of user n during the recent t months. It can be said that as the number of biomedical data used for authentication increases, the degree of uniqueness increases.

(ii) Since BM-signature (n, t) varies as time changes, BM-signature (n, t) may have the time stamp property [18], which is considered one of the essential properties to defend against active attacks. As t increases, the BM-signature acquires a more perfect time stamp property.

4.2. Authentication. The biomedical data of a user must be securely protected and cannot be accessed/altered by an unauthorized person, as this can cause a serious invasion of privacy. For this reason, the system proposed in this paper provides user/message authentication processes to securely transmit the biomedical data measured by PHDs. Figures 16 and 17 show the authentication processes for the sender side and receiver side, respectively. In Figure 16, new biomedical

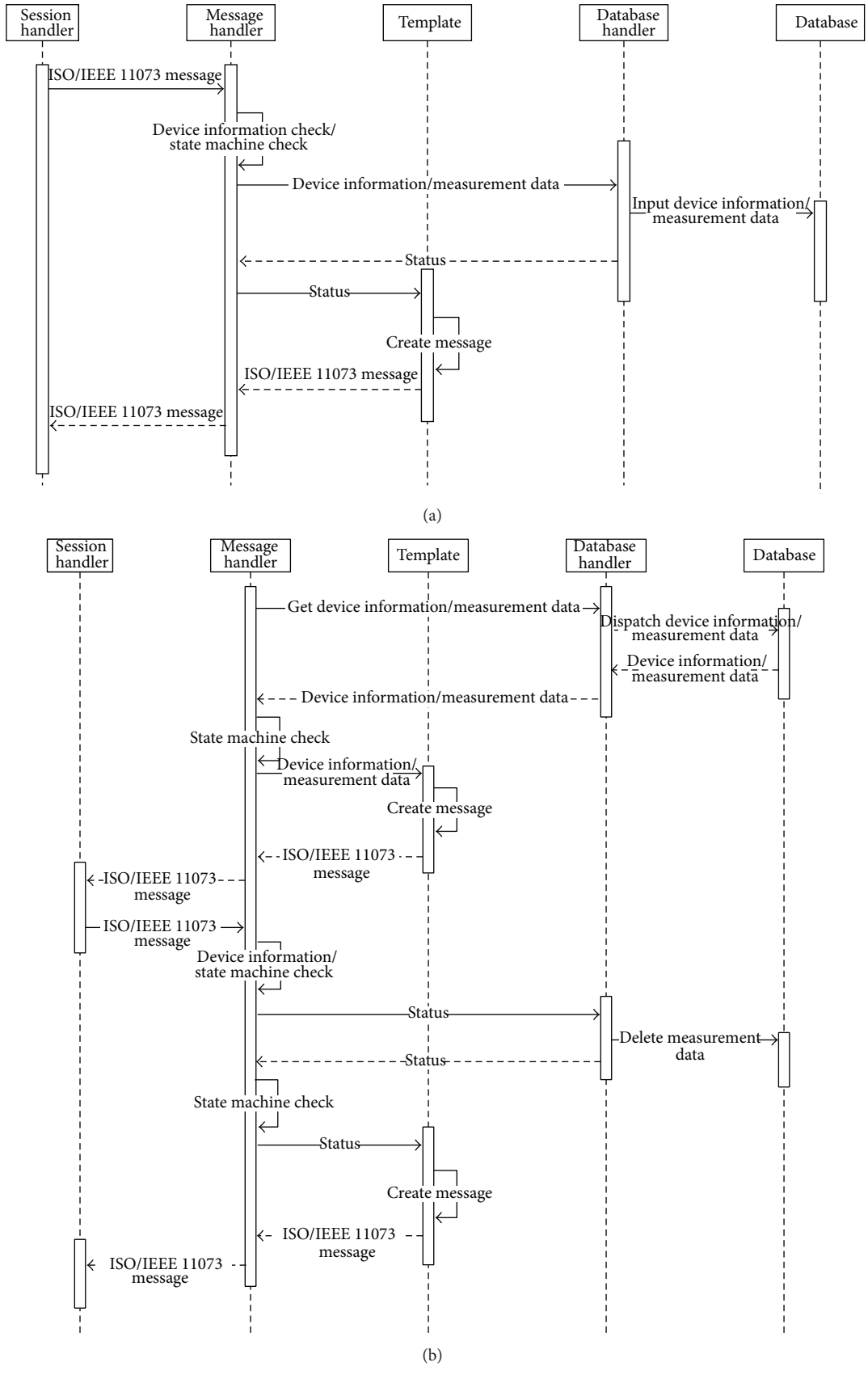

Figure 11: (a) Sequence diagrams of message reception in a PHD gateway. (b) Sequence diagrams of message integration in a PHD gateway.

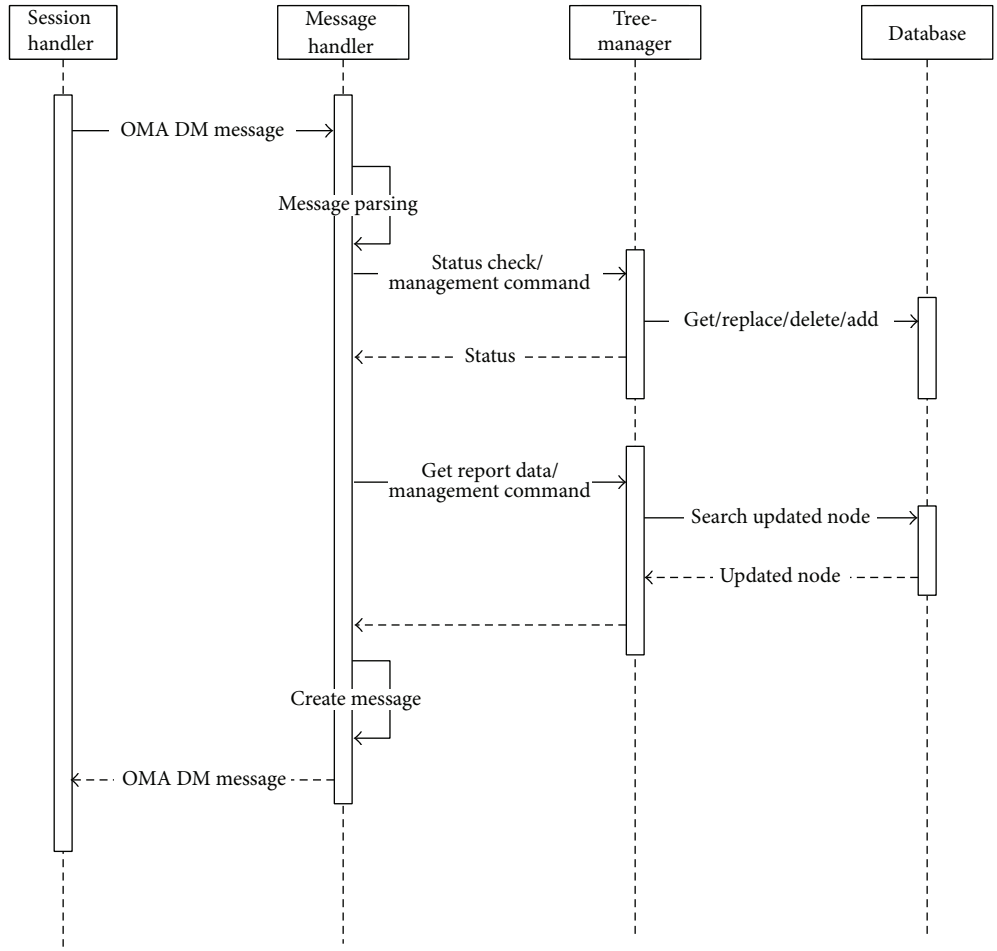

Figure 12: Sequence diagram of messages in a DM gateway.

data of a user (sender) measured by a PHD is given to the SHA512 hash algorithm to produce a 512-bit hash value that will be used to authenticate the new biomedical data by the receiver (the health management server). Since the SHA512 algorithm needs an initial value to be executed, the BM-signature of the user is used as the initial value. Thus, a message sent consists of the new biomedical data and the hash value of the data. Finally, the message is encrypted with the user password as the encryption key before it is sent. DES (Data Encryption Standard) encryption algorithm [18] is used in this paper.

Upon receiving the message sent by the sender (user), the receiver authenticates the received message, as shown in Figure 17. First of all, the received message is decrypted by using the DES decryption algorithm with the decryption key (user password), which is the same as the encryption key, in order to get the biomedical data and its hash value from the message. Next, the receiver executes the SHA512 algorithm to produce the message's hash value in order to compare the newly calculated hash value by the receiver with the hash value contained in the received message. If the two hash values are the same, the receiver decides that the received message has been authenticated. In other words, the receiver is sure that the receiving message is sent by the user who claims to be the sender and that the message has been unaltered during transmission. If the two have values that are not the same, the authentication fails and the receiver rejects the message.

5. Results and Discussion

5.1. Experiment Environments. The secure biomedical data management system explained above is constructed and tested in the experiment environments shown in Table 1. The executable code sizes of the PHD agent and DM agent are 439 KB and 179 KB, respectively, which indicates the PHD used in this study has sufficient room for two embedded agents.

5.2. Experiments. Some experiments are performed to show that the system proposed in this study works as designed. Because it is assumed that the system proposed in this study has a very large number of PHDs, a stress test is needed to make sure that the system is stable in heavy loaded environments. For the experiments, a 4-layered system (including

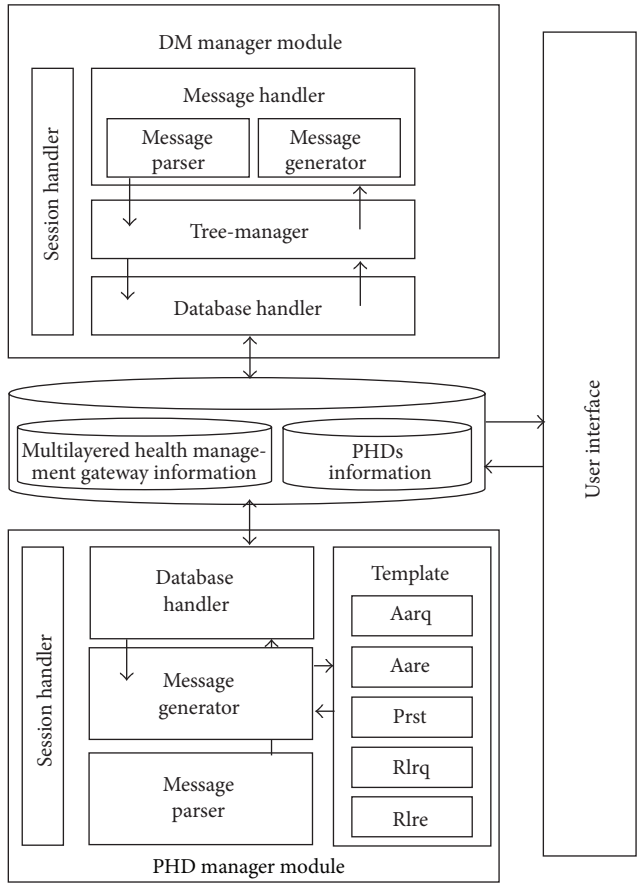

Figure 13: Structure of the multilayered health management server.

Table 1: Experiment environments.

Category	Multilayered health management server	Multilayered health management gateways	PHD
CPU	Intel core i7-3770 (3.4 Ghz)	Intel core i5-650 (3.2 Ghz)	Intel core i3-2367M (1.4 Ghz)
Main memory	8 GB	4 GB	2 GB
Hard disk type	SSD	SSD	HDD
Operating system	Windows 7	Windows 7	Windows 7
Language	C#	C#	C#

2 layers of gateways) is constructed. For a stress test, up to 1,200 threads are made to represent the same number of PHD agents. In addition, it is necessary to find the bottlenecks to improve the overall system performance.

Figure 18 shows the execution times in the subgateway (i.e., the gateway in the lower layer) as the number of PHD agents increase. The subgateway is connected to up to three hundred PHD agents. The execution time in the PHD module of the subgateway increases exponentially as the number of PHD agents increases, while the execution time in the OMA DM module remains practically unchanged. This is because the structures of the databases that store the health data (of PHD module) and the management data (of DM module) are different.

Figure 19 shows the execution times in the main gateway (i.e., the gateway in the higher layer) as the number of PHD agents increases. The main gateway is connected to two subgateways which connect to up to three hundred PHD agents each, having up to six hundred PHD agents connecting to the main gateway. The execution time in the PHD module of the main gateway increases exponentially as the number of PHD agents increases, while the execution time in the OMA DM module increases proportionally.

Figure 20 shows the execution times in the server as the number of PHD agents increases. The server is connected to two main gateways that connect to up to six hundred PHD agents each, having up to 1,200 PHD agents connecting to the main gateway. The execution time in the PHD module of

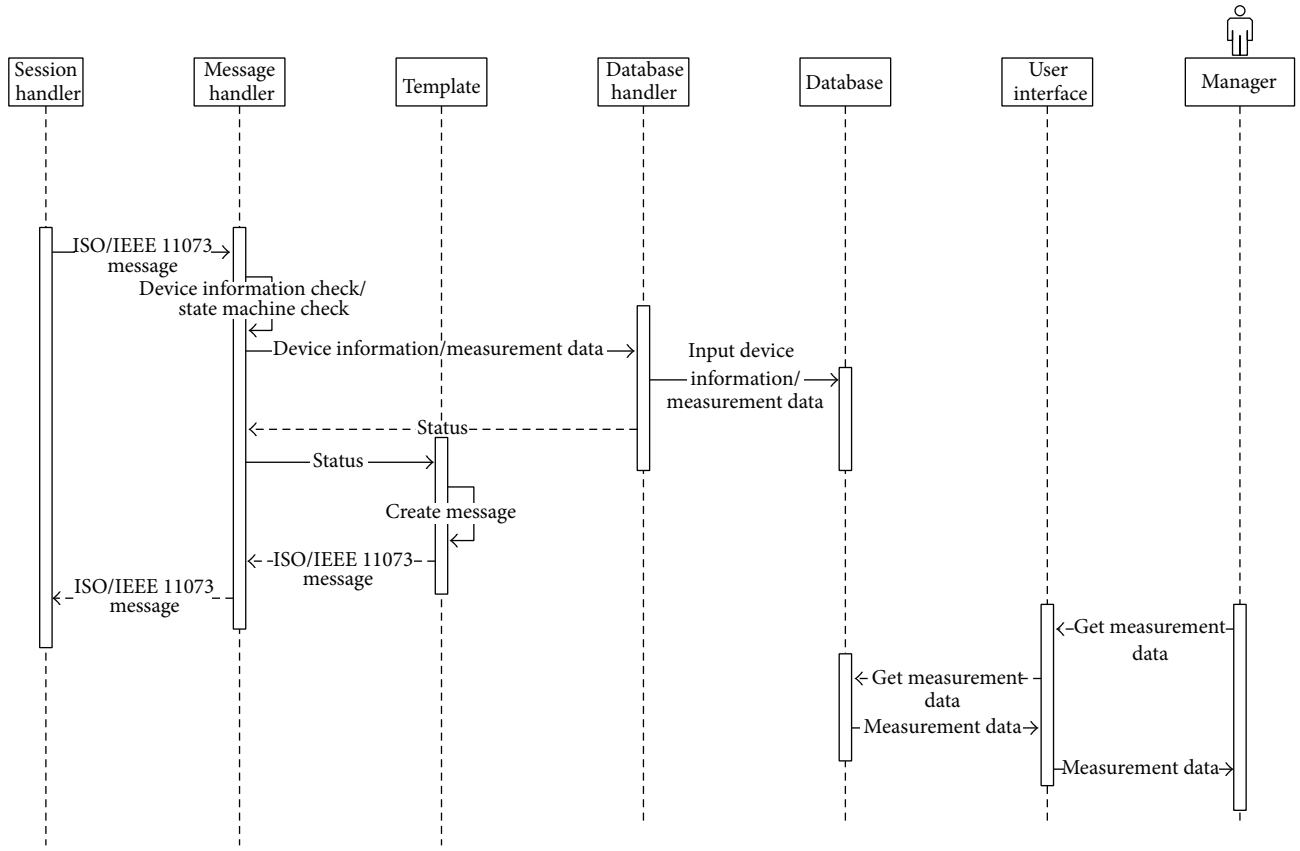

Figure 14: Sequence diagrams in a PHD manager module in the server.

the server increases exponentially as the number of PHD agents increases, while the execution time in the OMA DM module increases proportionally.

Because the ISO/IEEE 11073 messages are much more sensitive than the OMA DM messages to the number of PHD agents connected at once, one more experiment is performed to find out how many ISO/IEEE 11073 messages are lost at the server. When communication traffic becomes heavy, the number of messages that arrive but are rejected by the server becomes large. Loss of messages is considered a serious matter in health management systems. Figure 21 shows the ISO/IEEE 11073 message loss ratios by the server as the number of PHD agents increases. The loss of ISO/IEEE 11073 messages occurs when more than 500 PHDs are connected at the same time in the normal system (i.e., without any gateways at all). The loss ratio of the ISO/IEEE 11073 messages in the normal system is as high as 14% when 1,200 PHD agents are connected. On the other hand, no message loss occurs in the multilayered system proposed in this study, which demonstrates the superiority of the multilayered system to the normal system with regard to heavy traffic.

5.3. Performance Improvement

5.3.1. Bottlenecks. An attempt was made to find bottlenecks in the system constructed in this study in order to improve the performance of the system.

(i) PHD gateway module in the gateway and the server: almost 80% of the execution time in the gateway and the server is spent accessing/updating their own databases. Because the databases used in this study do not support parallel database operations, all of database requests must be executed in a critical section, which means that all of the requests are executed sequentially.

(ii) DM gateway module in the gateway and the server: it is found that almost 90% of the execution time in the gateway and the server is spent updating their DM trees. Unlike the PHD module, the DM module uses a hierarchical database based on XML files, which is thought to be the appropriate database type to store DM trees. As a result, execution times for tree searching and updating take up most of the execution times in the gateway and the server.

5.3.2. Bottleneck Alleviation

(1) Bottleneck Alleviation at PHD Gateway and the Server. The system uses four databases: DataInfo, DataReportingInfo, DeviceInfo, and Mapping. Among the databases, it is found that the execution time for accessing/updating DataReportingInfo database is the longest. The database keeps health data measured by PHDs. Therefore, in this study, the system is

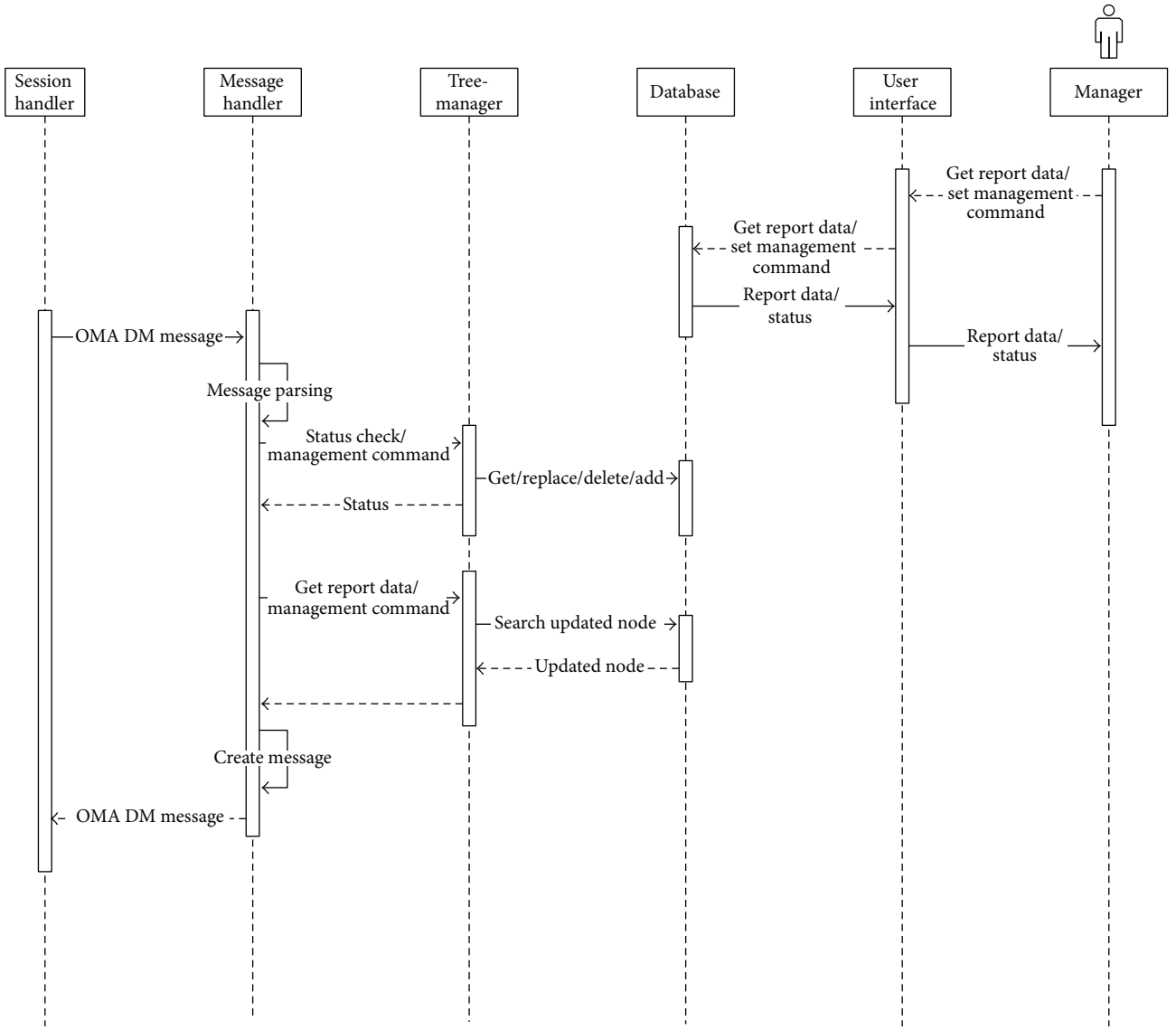

Figure 15: Sequence diagrams in a DM manager module in the server.

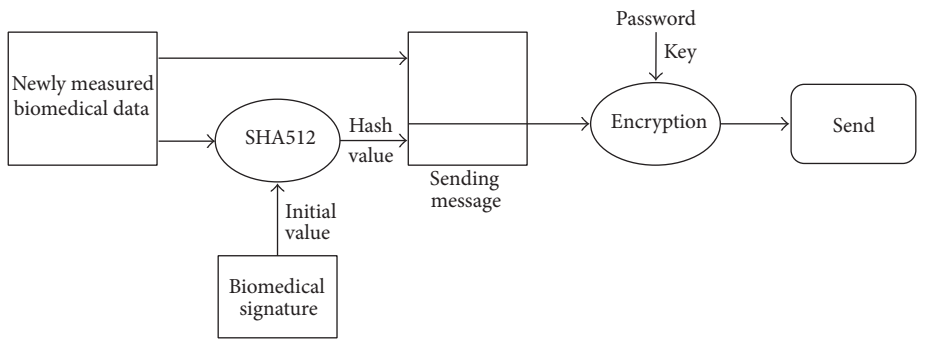

Figure 16: Authentication process for sender side.

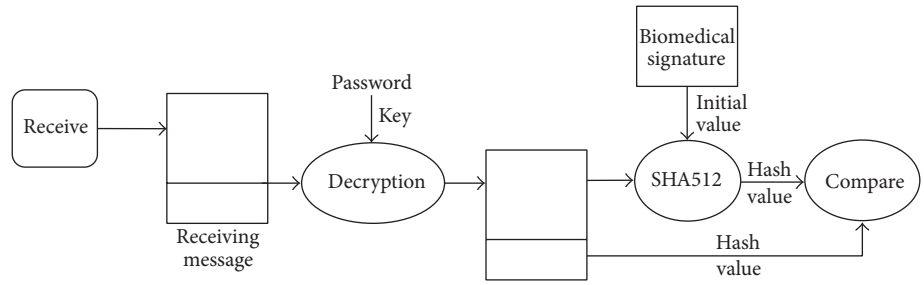

Figure 17: Authentication process for receiver side.

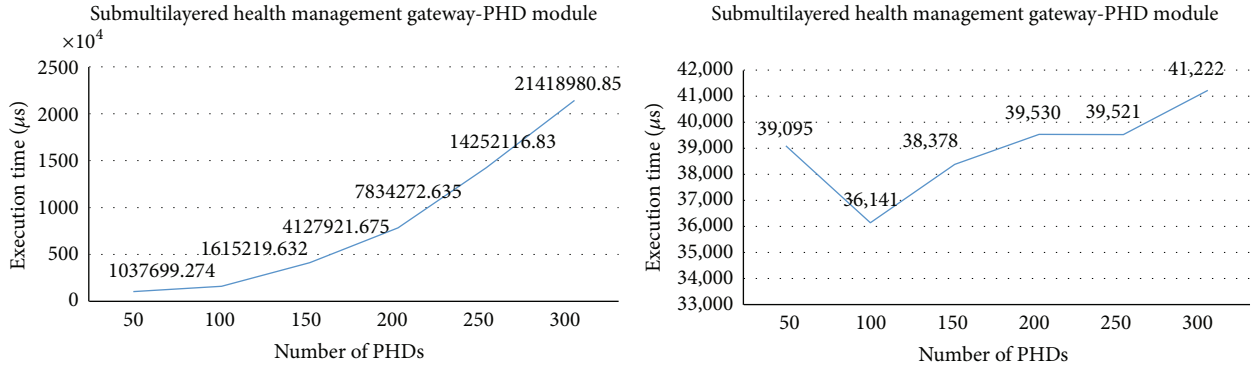

Figure 18: Execution times in the subgateway.

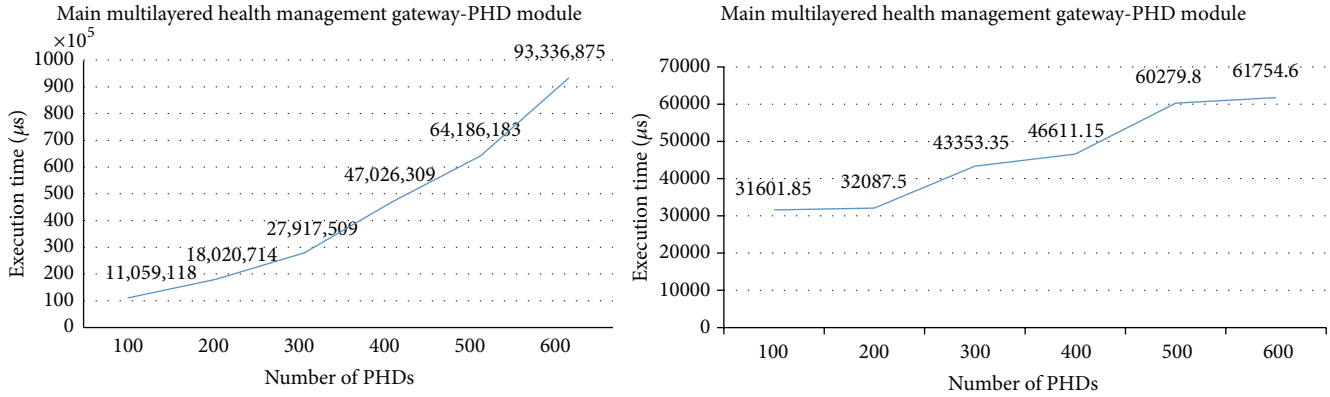

Figure 19: Execution times in the main gateway.

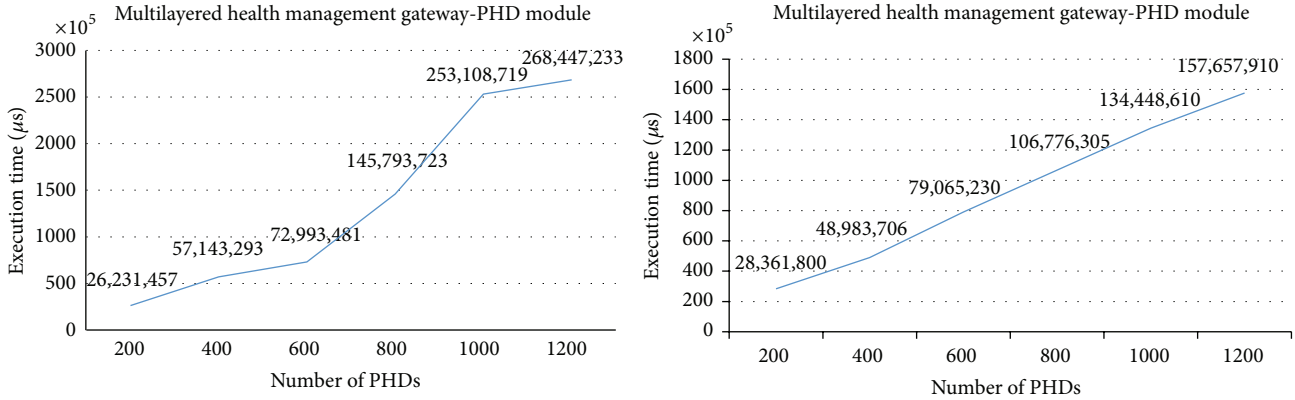

Figure 20: Execution times in the server.

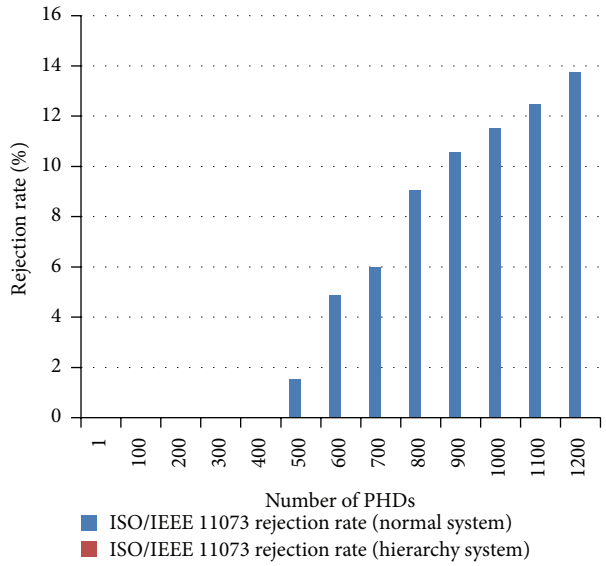

Figure 21: ISO/IEEE 11073 message loss ratios by the server.

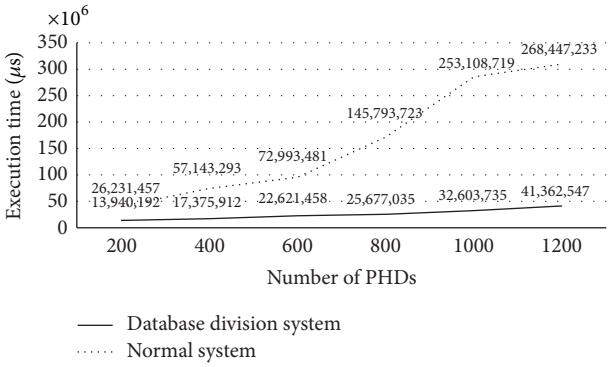

Figure 22: Performance improvement by the database division scheme.

modified in such a way that the DataReportingInfo database is divided into as many PHD databases as the number of PHD types used (three in the experiment). Likewise, databases for the subgateways and the main gateway are also divided according to the number of subgateways connecting to the main gateway.

Figure 22 shows the average execution times at the server for ISO/IEEE 11073 messages. The dotted line in the graph represents the waiting times at the server with one DataReportingInfo database, as was explained earlier. The solid line represents the execution times at the server, with DataReportingInfo database divided into three. As shown in the figure, the database division scheme greatly improves the system performance when the database is divided according to the connected PHD types. The relative performance improvement ratios with 200 and 1,200 PHDs areas are as high as 46.85% and 84.59%, respectively, 73.25% on average in the graph.

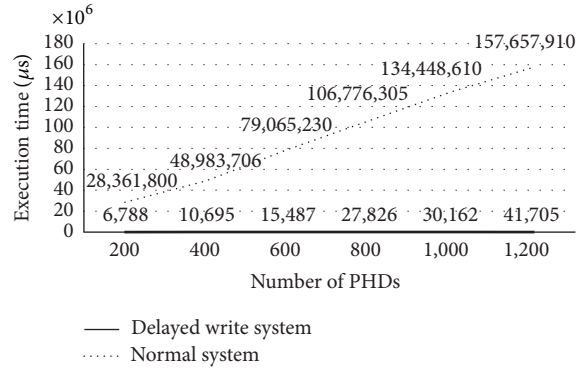

Figure 23: Performance improvement by the delayed write scheme.

(2) Bottleneck Alleviation at DM Gateway and the Server. This study uses the delayed write scheme to reduce the average execution times for tree searching and updating operations in the gateway and the server. To reduce the DM tree searching time, a hash table is constructed to eliminate frequent I/O interrupts, instead of direct access to the DM trees. In addition, the XML database is cached by the tree-manager module. In this experiment, the delayed write operation of the cached XML database is performed every 10 minutes or every time the number of connected PHDs at the same time falls below one hundred.

Figure 23 shows the average execution times at the server for OMA DM messages. The dotted line in the graph represents the execution times at the server without the delayed write operation, while the solid line represents the execution times at the server with the cached DM trees and the delayed write operation. As shown in the figure, the delayed write scheme greatly improves the system performance when there is a delayed write operation of the cached DM trees. The relative performance improvement ratio is as high as 99.99%, on average, in the graph.

6. Conclusions and Future Research

In this study, a multilayered remote PHD management system for a very large number of PHDs is proposed. The system has the following characteristics: first, the system is designed in a hierarchical fashion to lessen the bottleneck problem which might be caused by the requests from a very large number of PHDs. For the experiments explained earlier, a 4-layered hierarchical system including 2 layers of gateways is constructed. Second, the system is proposed to manage diverse PHDs remotely. The system has a separate database for every type of PHD to shorten database access times. Third, the system supports international standard communication protocols to achieve interoperability. Two protocols, the ISO/IEEE 11073 protocol and the OMA DM protocol, which were proposed as international standard communication protocols for PHD communication and remote device management, respectively, are extended and implemented in the system. Fourth, the system is integrated in the sense that both a PHD communication system and

a remote PHD management system work together as a single system. Gateways between PHDs and servers are designed to handle the integration tasks in the system.

Some experiments, including the stress test, are carried out to show that the system proposed in this study performs very well even when a very large number of PHDs are used. After locating the bottlenecks, it is found that there is still room to improve the system performance, and two modifications of the system were performed in this study: database division and delayed write. It is found that the system performance is greatly improved after these two modifications are applied.

Moreover, message loss is considered to be a very serious matter in health related systems such as the one outlined in this study. From the experiments, it is found that the loss ratio of ISO/IEEE 11073 messages in the normal system (e.g., the system without any gateways) is quite high when there is heavy traffic, while no message loss occurs in the multilayered system proposed in this study, demonstrating the superiority of the multilayered system to the normal system in situations of heavy traffic.

However, the multilayered system is not completely flawless. One flaw that the system might harbor is poor fault-tolerance. When some of the gateways fail, more complicated recovery schemes are needed. Therefore, efficient recovery/backup schemes or protocols will be studied to enhance the fault-tolerance of the system.

Conflict of Interests

The authors declare that there is no conflict of interests regarding the publication of this paper.

Acknowledgment

This research was supported by the Basic Science Research Programs through the National Research Foundation of Korea (NRF), funded by the Ministry of Education, Science and Technology (nos. 2012-013549 and NRF-2015R1D1A3A03019278).

References

[1] E. Broadbent, R. M. Q. Stafford, and B. A. MacDonald, "Acceptance of healthcare robots for the older population: review and future directions," *International Journal of Social Robotics*, vol. 1, no. 4, pp. 319–330, 2009.

[2] T.-H. Kim, R.-S. Chang, C. Ramos, and S. Mohammed, "Advanced sensor technology and applications in industrial control system," *International Journal of Distributed Sensor Networks*, vol. 2013, Article ID 516412, 2 pages, 2013.

[3] ISO/IEEE, *Health Informatics Point-of-Care Medical Device Communication Standard for Medical Device Communications*, ISO/IEEE, 2008.

[4] ISO/IEEE, Health Informatics-Personal Health Device Communication, IEEE Std. 11073-10443, Device Specialization-Physical Activity Monitor, 2008, http://standards.ieee.org.

[5] Health Informatics-Personal Health Device Communication, IEEE Std. 11073-20601 Optimized Exchange Protocol, 2008, http://standards.ieee.org.

[6] J. Pak and K. Park, "UbiMMS: an ubiquitous medication monitoring system based on remote device management methods," *The Journal of Healthcare Information Management*, vol. 41, no. 1, pp. 26–30, 2012.

[7] K. H. Park and J. G. Pak, "An integrated gateway for various PHDs in U-healthcare environments," *Journal of Biomedicine and Biotechnology*, vol. 2012, Article ID 954603, 7 pages, 2012.

[8] J. G. Pak and K. H. Park, "Advanced pulse oximetry system for remote monitoring and management," *Journal of Biomedicine and Biotechnology*, vol. 2012, Article ID 930582, 8 pages, 2012.

[9] E. Choi, "Performance test and analysis for an adaptive load balancing mechanism on distributed server cluster systems," *Future Generation Computer Systems*, vol. 20, no. 2, pp. 237–247, 2004.

[10] G. Franks and M. Woodside, "Performance of multi-level client-server systems with parallel service operations," in *Proceedings of the 1st International Workshop on Software and Performance (WOSP '98)*, pp. 120–130, 1998.

[11] OMA, *Device Management Protocol*, 2014, http://openmobilealliance.org.

[12] J. Lee, S. Suk, and B. Jung, "WiBro device management system based on OMA DM protocol," *KNOM Review*, vol. 10, no. 2, pp. 1–11, 2007.

[13] J.-M. Kang, H.-T. Ju, M.-J. Choi, J. W.-K. Hong, and J.-G. Kim, "OMA DM-based remote software fault management for mobile devices," *International Journal of Network Management*, vol. 19, no. 6, pp. 491–511, 2009.

[14] J. Kim, H. Ju, M. Choi, and J. W. Hong, "OMA DM-based remote software debugging of mobile devices," in *Managing Next Generation Networks and Services*, pp. 51–61, 2007.

[15] H.-K. Ryu, S.-R. Cho, S. Piao, and S.-H. Kim, "The design of remote vehicle management system based on OMA DM protocol and AUTOSAR S/W architecture," in *Proceedings of the 7th International Conference on Advanced Language Processing and Web Information Technology (ALPIT '08)*, pp. 393–397, July 2008.

[16] K. Park and J. Pak, "An integrated gateway for various PHDs in U-healthcare environments," *Journal of Biomedicine and Biotechnology*, vol. 2012, Article ID 954603, 7 pages, 2012.

[17] K. H. Park and S. Lim, "Message processing at integrated PHD gateways for servicing various PHDs," *International Journal of Multimedia and Ubiquitous Engineering*, vol. 9, no. 3, pp. 367–374, 2014.

[18] W. Stallings, *Cryptography and Network Security: Principles and Practice*, Pearson, New York, NY, USA, 5th edition, 2011.

Hindawi Publishing Corporation
BioMed Research International
Volume 2015, Article ID 830809, 11 pages
http://dx.doi.org/10.1155/2015/830809

Research Article

Towards a Food Safety Knowledge Base Applicable in Crisis Situations and Beyond

Alexander Falenski, Armin A. Weiser, Christian Thöns, Bernd Appel, Annemarie Käsbohrer, and Matthias Filter

Federal Institute for Risk Assessment, Diedersdorfer Weg 1, 12277 Berlin, Germany

Correspondence should be addressed to Alexander Falenski; alexander.falenski@bfr.bund.de

Received 26 September 2014; Accepted 24 November 2014

Academic Editor: Sabah Mohammed

In case of contamination in the food chain, fast action is required in order to reduce the numbers of affected people. In such situations, being able to predict the fate of agents in foods would help risk assessors and decision makers in assessing the potential effects of a specific contamination event and thus enable them to deduce the appropriate mitigation measures. One efficient strategy supporting this is using model based simulations. However, application in crisis situations requires ready-to-use and easy-to-adapt models to be available from the so-called food safety knowledge bases. Here, we illustrate this concept and its benefits by applying the modular open source software tools PMM-Lab and FoodProcess-Lab. As a fictitious sample scenario, an intentional ricin contamination at a beef salami production facility was modelled. Predictive models describing the inactivation of ricin were reviewed, relevant models were implemented with PMM-Lab, and simulations on residual toxin amounts in the final product were performed with FoodProcess-Lab. Due to the generic and modular modelling concept implemented in these tools, they can be applied to simulate virtually any food safety contamination scenario. Apart from the application in crisis situations, the food safety knowledge base concept will also be useful in food quality and safety investigations.

1. Introduction

In pandemic crisis situations, timely and scientifically based exposure assessments are of crucial importance for all involved stakeholders (Regulation (EC) 178/2002) [1]. These exposure assessments are even more important in crisis scenarios in which the human population is at high risk. As could be witnessed in recent years during international foodborne disease outbreaks, tools and methodologies supporting efficient exposure assessments including the tracing back and forward of contaminated commodities are essential [2]. In an outbreak, risk assessors have to respond quickly to questions that crisis managers raise to support their decision-making processes. In order to empower risk assessors in their work predictive modelling software tools can provide valuable support, for example, by creating situation-specific models and running simulations for different contamination scenarios.

As a proof-of-principle scenario, the intentional contamination of a beef salami production facility with ricin was selected. Ricin is a toxin produced by the plant *Ricinus communis*. Its seeds are used for the production of over 1,100,000 tonnes of castor oil annually for various products, for example, paints, coatings, or polymers machines [3]. Because ricin is water soluble, it could be extracted from the remnants of the oil production for deliberate contamination of foods. The ricin content of the seeds makes up 1–5% [4, 5] or up to 1.5% in the castor cake after oil extraction [3, 6].

The toxin has been investigated in biological weapon programmes of the USA, Canada, and Iraq [7, 8]. It was presumably used in the assassination of the Bulgarian dissident Georgi Markov in 1978 [9] and was also found in a letter addressed to the White House in 2003 [10]. Ricin is classified as category B biological weapon [11].

The toxin acts as a protein synthesis inhibitor. In humans, the lethal oral dose is estimated to be 1–20 mg/kg body

weight with symptoms like abdominal pain, vomiting, and diarrhoea [12]. Ricin is pH stable over a wide range [13]. For inactivation, high temperatures are needed. Pasteurization at 72°C for 15 seconds or at 89°C for 1 second did not fully inactivate ricin in infant milk formula [14]. Neither did the steaming of castor beans at 80°C for 40 minutes inactivate the toxin [15].

In the case of an intentional contamination of a food production chain, risk assessors need to estimate the consumers' exposure to the agent based on the amount of the contaminant that ends up in the final product. Additionally, the amount of agent introduced into the production chain needs to be estimated. Also, to be able to inactivate the agent in production machineries and intermediate products, it is necessary to know whether there are effective detergents for this purpose.

The aim of this research was to verify that a framework established for efficient and transparent conduction of exposure assessments in the food sector could also be applied in case of bio- and agroterroristic crisis situations. For this, data and models on tenacity of highly pathogenic agents were collected and applied in sample scenarios together with knowledge on relevant food production processes [16].

2. Material and Methods

2.1. Literature Review. A literature research on publications describing experimental data or models on the inactivation of ricin in food matrices was performed using the online databases PubMed (PM, http://www.ncbi.nlm.nih.gov/pubmed) and Web of Science (WoS, http://apps.webofknowledge.com) with standard settings. Publications were searched using the search string "ricin ((stability food) OR (inactivation food) OR beverage OR inactivation OR (models food) OR (predictive models))." Database searches were performed in January and February 2014 according to the PRISMA statement for systematic reviews [17].

To gather information about the inactivation of ricin in foods, data and mathematical models were reviewed from the literature. All was stored in the internal database of the open-source modelling tool PMM-Lab (see Section 2.2).

Information on food processing chains was gathered from publications in scientific journals and from German text books about industrial and manual processing of beef or milk [18, 19]. Additionally, information on processing chains was collected via interviews of manufacturers and experts.

2.2. Food Safety Knowledgebase. The food safety knowledgebase consists of three components:

(1) A collection of data and information on food production process parameters (FoodProcess knowledge base);

(2) A collection of data and predictive models on relevant pathogenic agents (predictive model knowledge base);

(3) A modular open-source software tool for exposure assessment calculations.

Technically, these components have been implemented in two modular software tools, PMM-Lab and FoodProcess-Lab (FPL). Both can be downloaded freely, installed locally, and used offline. This enables users to keep unpublished or confidential data on their desktop. The software also incorporates knowledge on food production processes and predictive models as well as the creation of scenarios as illustrated in Section 3.

PMM-Lab and FPL are both extensions to the scientific workflow management system KNIME (http://www.knime.org/) and inherit its modularity. The KNIME framework allows users to execute any data processing task by combination of small executable software modules, called nodes, into executable workflows. Each node's calculation result can be inspected visually at the node's outport. Plenty of nodes are available in KNIME and they can also be used from within PMM-Lab and FPL. In this way, it becomes possible to import data from all sources virtually and even to create reports automatically from workflows. In relation to food safety modelling, this modular workflow-based approach is therefore highly beneficial as the generation of prediction results becomes reproducible and transparently documented.

2.3. Software for Predictive Modelling (PMM-Lab). PMM-Lab (http://sourceforge.net/projects/pmmlab) is a community resource for generation and application of predictive models, integrating more than 20 domain specific nodes as a new node library into KNIME. One of the advantages of this tool is that now raw data used to generate predictive models and the model generation workflow can be physically connected to the final model. This allows the data used for model generation to be viewed at any time. PMM-Lab additionally contains a database that stores all information (experimental data, models, metadata, and workflows) in relational database tables [20].

Additional information on how to use PMM-Lab can be found in the PMM-Lab Wiki (http://sourceforge.net/p/pmmlab/wiki/Home).

2.4. Software for Predicting the Tenacity of Pathogens along Food Processing Chains (FoodProcess-Lab). FPL (http://sourceforge.net/projects/foodprocesslab) is like PMM-Lab, an extension to the KNIME framework providing six domain specific nodes structured inside the FPL node library. The "Ingredients" and "FoodProcess" nodes are the graphical representation of food processing chains and contain information on food processing parameters. All this information can be saved in the integrated database via the "Writer" node. Additionally, FPL can be used to perform mathematical calculations on agents spreading within food processing chains by the application of the "Agents" node. Via the "Filter Models" Tab of the "FoodProcess" node, the software can also make use of models on agent tenacity saved in the PMM-Lab section of the database. Information on food production process chains and parameters can be retrieved from the FPL database itself.

Finally, the "View" node can be used to graphically represent the change of food process conditions and agent

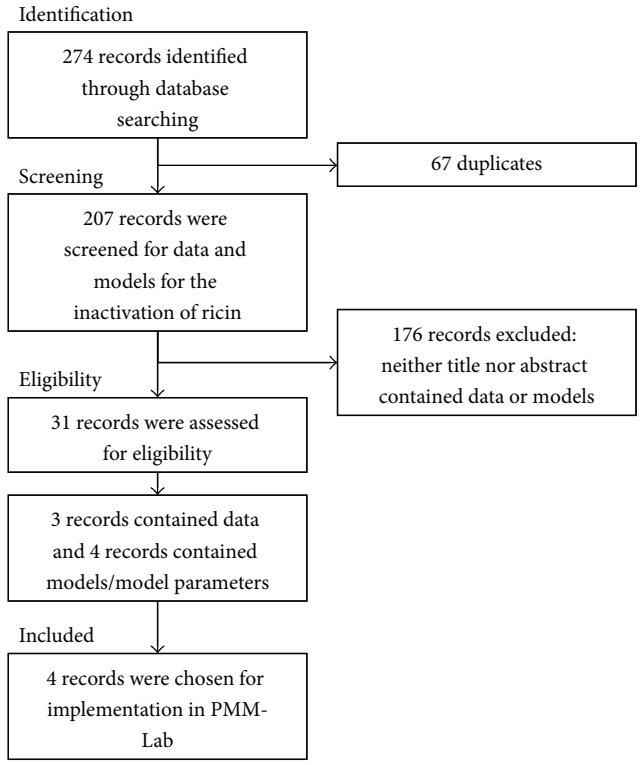

Figure 1: Flow diagram on the literature review performed precluding the implementation of models for the inactivation of ricin in foods with PMM-Lab.

concentration for the whole food process chain. Information about installation and sample workflows can be found in the FoodProcess-Lab Wiki (http://sourceforge.net/p/foodprocesslab/wiki/Home).

3. Results

Predictive models are important components of quantitative risk assessments. Several software tools exist which are designed to create predictive models based on pathogen specific experimental data (e.g., GinaFit [26], DMfit [27]). Additionally, there are tools allowing the application of models for predicting the tenacity of agents in different food matrices (e.g., ComBase Predictor [28], PMP [29], and SSSP [30]). However, in case of bio- and agroterrorist agents, authorities have to develop their own knowledge bases covering agent tenacity, considering typical food production processes including processing parameters. First efforts for a systematical collection of information concerning the latter aspect have been made in projects like FRISBEE (http://frisbee-wp2.chemeng.ntua.gr/coldchaindb) [31]. Unfortunately, the available solutions are currently only directed towards time-temperature profiles of postproduction processing steps. Additionally, models and software developed and used within the FRISBEE system are not freely available. In order to empower authorities to establish their own knowledge base in preparation for bio- or agroterrorist events free software access is highly beneficial. This requirement also takes into account the fact that in case of a real intentional food contamination situation the information exchange between authorities would be much easier if open-source software solutions already commonly used were applied.

3.1. Knowledge Base Generation

3.1.1. Current Knowledge on the Inactivation of Ricin. In the literature research, a total of 274 entries dealing with the inactivation of ricin were retrieved from PubMed and Web of Science (see Figure 1). Of these, 31 publications were considered as relevant for in-depth analysis. Seven articles contained models, model parameters, or experimental data on the inactivation of ricin in food (see Table 1).

These papers describe the influence of temperature [14, 21–23], pH [13, 25], and chemicals [24] on ricin activity. Different food matrices as well as buffers were used in these reports: beef, milk, egg [22], infant formula [14, 24], orange juice, apple juice [21], pancake mix, peanut butter [24], phosphate buffered saline (PBS) [22, 24], sodium phosphate/sodium acetate buffer [13, 25], and KCl buffer [23]. The applied detection methods included fluorescence measurement, ELISA and cytotoxicity assays (see Table 1).

3.2. Ricin Model Repository

3.2.1. Option 1 (Reimplementation of Models from Literature References). Model equations, model parameters, and model metadata from the studies summarized in Table 1 were used

Table 1: Studies on inactivation of ricin in food matrices.

Matrix	Environmental conditions	Detection method(s)	Rate constants[a]	Reference
Apple juice	25°C; 60–90°C ($n = 6$)	ELISA, cytotoxicity assay	√	[21]
Beef	63°C; 72°C	Fluorescence		[22]
Buffers (HCl, KCl, glycine, acetic acid, KOH, KH_2PH_4, K_2HPO_4, boric acid, $KHCO_3$, K_2CO_3)	43.9, 52.9, 65.3, 71.5, 78.2, 86.5°C pH 1–12	Visible light (colour change)	√	[23]
Egg	63°C; 72°C	Fluorescence		[22]
Infant formula	60–90°C ($n = 6$)	ELISA, cytotoxicity assay	√	[14]
Infant formula[c]	NaClO (1.3, 6.7, 13 mM) at RT	ELISA, cytotoxicity assay	√	[24]
Infant formula[c]	PAA (6.6, 13, 26 mM) at RT	ELISA, cytotoxicity assay	√	[24]
Milk	63°C; 72°C	Fluorescence		[22]
Na-phosphate/Na-acetate buffer	pH 3–10 ($n = 16$) at 20°C	Fluorescence		[13]
Na-phosphate/Na-acetate buffer	pH 2–7 at 25°C ($n = 15$) and 60°C ($n = 6$); 5–70°C at pH 7.3 ($n = 16$), 4.7 ($n = 15$), 4.0 ($n = 10$) and 3.0 ($n = 8$)	Fluorescence[b]		[25]
Orange juice	25°C; 60–90°C ($n = 6$)	ELISA, cytotoxicity assay	√	[21]
Pancake mix[c]	NaClO (6.7, 13, 27 mM) at RT	ELISA, cytotoxicity assay	√	[24]
Pancake mix[c]	PAA (6.6, 13 mM) at RT	ELISA, cytotoxicity assay	√	[24]
Pancake mix[c]	PAA-based disinfectant (1.0, 3.0, 5.0% with pH 5.0, 4.4, 3.9, resp.) at RT	ELISA	√	[24]
Pancake mix[c]	CAD (3.0, 5.0, 7.0% with pH 10.2, 11.0, 12.1, resp.) at RT	ELISA	√	[24]
PBS	63°C; 72°C	Fluorescence		[22]
PBS[c]	NaClO (67, 130, 270 μM) at RT	ELISA, cytotoxicity assay	√	[24]
PBS[c]	PAA (6.6, 13, 26 mM) at RT	ELISA, cytotoxicity assay	√	[24]
PBS[c]	PAA-based disinfectant (0.1, 0.5, 1.0% with pH 6.2, 5.7, 5.0, resp.) at RT	ELISA	√	[24]
PBS[c]	CAD (0.5, 2.0, 5.0% with pH 8.8, 9.7, 11.0, resp.) at RT	ELISA	√	[24]
Peanut butter[c]	NaClO (13, 27, 40 mM) at RT	ELISA, cytotoxicity assay	√	[24]
Peanut butter[c]	PAA (39, 66, 130 mM) at RT	ELISA, cytotoxicity assay	√	[24]
Peanut butter[c]	PAA-based disinfectant (1.0, 3.0, 5.0% with pH 5.0, 4.4, 3.9, resp.) at RT	ELISA	√	[24]
Peanut butter[c]	CAD (3.0, 5.0, 7.0% with pH 10.2, 11.0, 12.1, resp.) at RT	ELISA	√	[24]

[a]√: published rate constants useful for modelling the inactivation of ricin in foods.
[b]Fluorescence of ricin B-chain.
[c]In solution and dried on stainless steel coupons.
NaClO: sodium hypochlorite, CAD: chlorinated alkaline detergent, PAA: peracetic acid, and RT: room temperature.

to reimplement models using PMM-Lab. Model equations were entered as the so-called primary model formulas into the PMM-Lab Formula Creator node. Then, metadata and model parameters from the publications were copied to an MS Excel table and imported into PMM-Lab via the XLS Model Reader node. The generated primary models were saved to the local PMM-Lab model database.

3.2.2. Option 2 (Model Estimation). If not all model parameters necessary for reimplementation were given in a publication, proprietary models were created based on experimental data or parameter estimates in the publication. This approach was also applied, where parameter estimates were missing in published models. In case of the publication by Jackson et al. [21], the estimates on parameter "A" were not given

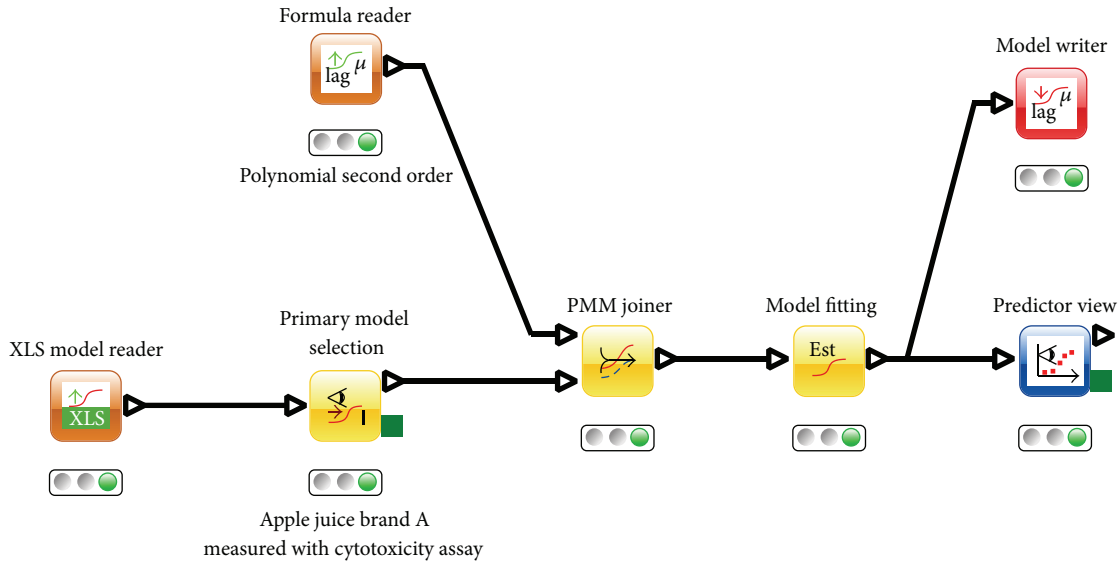

FIGURE 2: Estimation of proprietary secondary models and its application for prediction of ricin inactivation in apple juice.

(see (1)). In this case, the available primary models could be used to create proprietary secondary models allowing the inactivation of ricin to be predicted over the whole temperature range covered by the performed laboratory experiments. The so-called secondary models describe the relationship of primary model parameters to varying experimental conditions, like, for example, temperature. In this way, combined primary and secondary models can be used to interpolate ricin inactivation in the range of measured experimental conditions.

Jackson et al. [21] published a primary model formula which was fitted to measurements of residual ricin (1) after inactivation in different foods

$$\%\text{ricin} = Ae^{-kt}, \tag{1}$$

where A is an empirically determined constant, k is the first-order rate constant, and t is the thermal treatment duration. As suggested in the publication, the Arrhenius equation (2) was then used as secondary model formula to create a model for the change of the first-order rate constant k with temperature

$$k = Be^{-E_a/(RT)}, \tag{2}$$

where B is an empirically determined constant, E_a is the activation energy, R is the gas constant, and T is the temperature in Kelvin.

To simplify the parameter estimation process, the first-order rate constant was transformed by application of the natural logarithm transformation. Equations (1) and (2) were adjusted accordingly (see the following equation):

$$\begin{aligned} \%\text{ricin} &= Ae^{(-\exp(\ln(k))t)}, \\ \ln(k) &= \ln(B) - \frac{E_a}{(RT)}. \end{aligned} \tag{3}$$

Other equations were also tested for secondary model estimation, of which the second-order polynomial performed best as in the following equation:

$$\ln(k) = a_0 + a_1 * T + a_2 * T^2, \tag{4}$$

where a_0, a_1, and a_2 are empirically determined constants and T is the temperature in degrees Celsius.

The model generation workflow applied is depicted in Figure 2. As users can use the Formula Reader node to select equations from a wide formula collection implemented in the software, this very same workflow also allows alternative (better fitting) secondary models to be searched for. The results of the model fitting step performed with PMM-Lab are shown in Tables 2 and 3.

Overall, most of the fitted models had an R^2 greater than 0.94 with a few exceptions (minimum was 0.915). According to R^2, the polynomial models performed better than the Arrhenius-based models. In contrast, the AIC values from the Arrhenius models are lower than those from the polynomial models, indicating that the Arrhenius models should be preferred. This can be explained by the fact that Arrhenius models contain only two free model parameters instead of three in the polynomial models. As a consequence, the estimated Arrhenius-type secondary models were used to create a combined primary/secondary model which was saved into the PMM-Lab model database.

In comparison with the values for the inactivation energies published by Jackson et al. [21], half of those estimated with PMM-Lab match the published values (Table 2). However, four E_a values differ. In order to find higher agreement of published and estimated data, the original Arrhenius equation (non-ln-transformed) was used and one out of six outlying inactivation rates were omitted, resulting in a very high agreement with the published data (Table 2, last column; for full data, see Supplementary Table 3 in Supplementary Material available online at http://dx.doi.org/10.1155/2015/830809).

Table 2: Secondary model estimation and quality criteria: Arrhenius equation, ln transformed; $\ln(k) = \ln(B) - E_a/(8.314*T)$.

Matrix	Ricin inactivation measured with	E_a [kJ/mol] Jackson et al.	E_a [kJ/mol] This paper	$\ln(B)$	RMSE	R^2	AIC	E_a [kJ/mol] This paper[a]
Apple juice clear	ELISA	120 ± 10	188 ± 20	62.32	0.4891	0.9551	6.9853	118
Apple juice clear	Cytotoxicity assay	110 ± 20	185 ± 14	61.23	0.3448	0.9765	2.7898	119
Apple juice cloudy	ELISA	200 ± 11	187 ± 18	61.82	0.4298	0.9646	5.4350	204[b]
Apple juice cloudy	Cytotoxicity assay	240 ± 30	169 ± 18	55.95	0.4230	0.9582	5.2437	262[b]
Orange juice A	ELISA	170 ± 30	203 ± 31	67.47	0.7403	0.9154	11.9581	165
Orange juice A	Cytotoxicity assay	140 ± 30	177 ± 19	58.8	0.4579	0.9558	6.1937	139
Orange juice B	ELISA	170 ± 20	216 ± 28	72.1	0.6722	0.9370	10.8003	174[c]
Orange juice B	Cytotoxicity assay	161 ± 09	228 ± 26	76.23	0.6206	0.9511	9.8419	158

Values are estimated parameter values ± standard errors; [a]Activation energies calculated using the original Arrhenius equation $k = B* \exp(-E_a/(8.314*T))$; for a better fitting, some of the inactivation rates Jackson et al. [21] published were not used in this calculation (see [b] and [c]); of the published inactivation rates at 60, 70, 75, 80, 85 and 90°C, the rate at 90°C was omitted in [b] and the rate at 85°C was omitted in [c]. Standard errors could not be calculated. T: Temperature [K].

Table 3: Secondary model estimation and quality criteria: Polynomial of second order; $\ln(k) = a_0 + a_1*T + a_2*(T^2)$.

Matrix	Ricin inactivation measured with	a_0	a_1	a_2	RMSE	R^2	AIC
Apple juice clear	ELISA	−37.5238	0.7551	−0.0038	0.3643	0.9813	31.7249
Apple juice clear	Cytotoxicity assay	−31.8713	0.5990	−0.0028	0.2646	0.9896	27.8857
Apple juice cloudy	ELISA	−23.2621	0.3635	−0.0012	0.4874	0.9659	35.2165
Apple juice cloudy	Cytotoxicity assay	−22.9993	0.3852	−0.0015	0.4703	0.9613	34.7882
Orange juice A	ELISA	3.0323	−0.3642	0.0038	0.6293	0.9541	38.2830
Orange juice A	Cytotoxicity assay	−6.3983	−0.0783	0.0017	0.4394	0.9695	33.9735
Orange juice B	ELISA	−10.0907	−0.0180	0.0016	0.7194	0.9459	39.8892
Orange juice B	Cytotoxicity assay	−25.3006	0.3829	−0.0010	0.7134	0.9515	39.7884

T: temperature [°C].

3.3. Food Process Model Repository. FPL can use knowledge on food processing chains stored in the integrated database. Furthermore, users can collect new information on processing parameters, for example, the processing steps for salami production. FPL also allows the user to describe processing chains with commodity flows that split up and join back again as in the case of the production of a meat product from carcasses (carcass → [processing to different pieces] → further processing, e.g., cutting or mincing → [addition of different parts of processed meat and fat] → meat product with standardized amount of fat). Values on temperature or other environmental conditions can either be entered as a single value, as a time-temperature profile, or as a function. The software also enables users to import knowledge on food production processes directly from other tools like CARVER [32].

As the basic design principle FPL represents each processing step as a food processing node (see Figure 3) which can be configured according to real world conditions. It is saved in the knowledge base or simply as a KNIME workflow. A similar modular concept was already introduced by Nauta [33, 34]. His Modular Process Risk Model (MPRM) is widely used in the domain of quantitative microbial risk assessments. In FPL, every FoodProcess node can both model microbial tenacity and calculate the effect of product handling changes. Its modularity refers to the reusability of single FoodProcess nodes as well as of full food processing chains (workflows). Together with the predictive models stored in the PMM-Lab database, the collected process information is then used as input for the predictions which are performed in each FPL process node [16].

3.4. Application of the Knowledge Base in Scenario Simulation

3.4.1. Use Case 1 (Scenario Simulation). In the following hypothetical contamination scenario, minisalamis (small salami sticks, weight: 10 g) are contaminated with ricin during their production. The food processing chain in brief is as follows [35]: Large parts of beef, pork, and lard are cut into pieces and are frozen before the mincing step (Table 4). The frozen meat is minced and pickling salt with nitrate, spices, sodium ascorbate, and lactic acid bacteria are added. The prepared meat is filled into casings and the raw sausages are warmed to room temperature. A short bath in potassium ascorbate prevents growth of bacteria on the surface of the casing. The minisalamis mature for 72 hours at 20–24°C and are smoked for 124 hours at 18–20°C. The hypothetical contamination of a production batch of the size of 100 kg with 3000 g pure ricin is set to take place during the process step "packaging," meaning that the sausages would be contaminated on the outside. Finally, the minisalamis are stored and sold. The

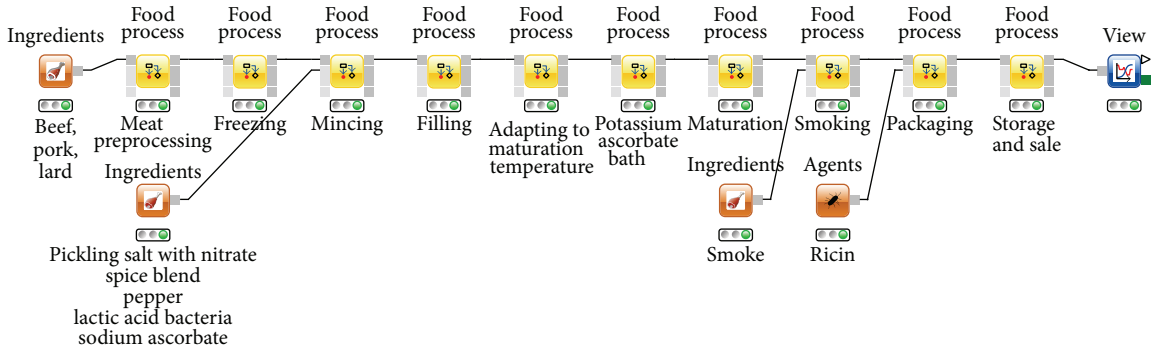

Figure 3: Process steps in the production of minisalamis as represented in FPL. Every yellow symbol (node) represents one processing step in the production of beef salami, configured in accordance with the data in Table 4.

Table 4: Process steps in the production of beef salami.

Process step	Duration[a]	Temperature [°C]	Introduced ingredient	Ingredient mass [kg]	Product
Meat preprocessing	3 min	2	Raw beef Raw pork Lard	35 35 30	Pieces of raw beef, pork, lard
Freezing	24 h	−20			
Mincing	10 min	−20 → 0	Pickling salt with nitrate Spice blend Pepper Lactic acid bacteria Sodium ascorbate	2.8 1.3 0.3 0.08 0.05	Seasoned minced meat
Filling	3 min	0			Raw sausages
Adapting to maturation	4 h	22			
Potassium ascorbate bath	5 s	22			
Maturation	72 h	24 → 22 → 20			
Smoking	124 h	20 → 18	Smoke		Smoked minisalami
Packaging	4 h	17			
Storage and sale	7/15/34 d	17			

[a]Duration, d: day, h: hour, min: minute, and s: second.

representation of the food processing chain in FPL and the introduction of ricin are both shown in Figure 3.

Ricin is a protein which degrades in the course of time, depending on temperature and pH. In the described scenario, the amount of active ricin was calculated with an inactivation rate published by Jackson et al. [21]. In the software, distinct predictive models can be assigned to each node/processing step. The amount and concentration of ricin left at the end of one node are "handed over" to the following node where it serves as the initial concentration.

For the given example, the time period for storage and disposal (until the customer is able to consume the product) was set to 15 days at 17°C. Figure 4 shows the simulation results with respect to inactivation of ricin along the depicted processing chain. 12% of the introduced amount of ricin remains active until the day of consumption, resulting in a concentration of 4.3 mg ricin/g sausage. According to [12], the lethal oral dose for humans may be as low as 1 mg/kg of body weight. Thus, a person weighing 80 kg would already consume a deadly dose of ricin when eating only two minisalamis.

3.4.2. Use Case 2 (Exploring Alternative Scenarios). Contamination of a food processing chain can occur accidentally or intentionally and in various ways. In this example, ricin might not only be introduced at the packaging step, but also be mixed into the sausage meat during the mincing step or the toxin might be attached to the sausages during the maturation. In each of the three cases, the time until consumption is also an important factor concerning the amount of active ricin left. Therefore, the consequences of consuming minisalamis 7, 15, and 30 days after their production were calculated (Table 5). In most of the scenarios, the amount of active ricin left is below the lethal dose of 1 mg/kg of body weight. According to the model, this is the case when the salamis are contaminated during the mincing and maturation steps and if a minisalami contaminated during the packaging

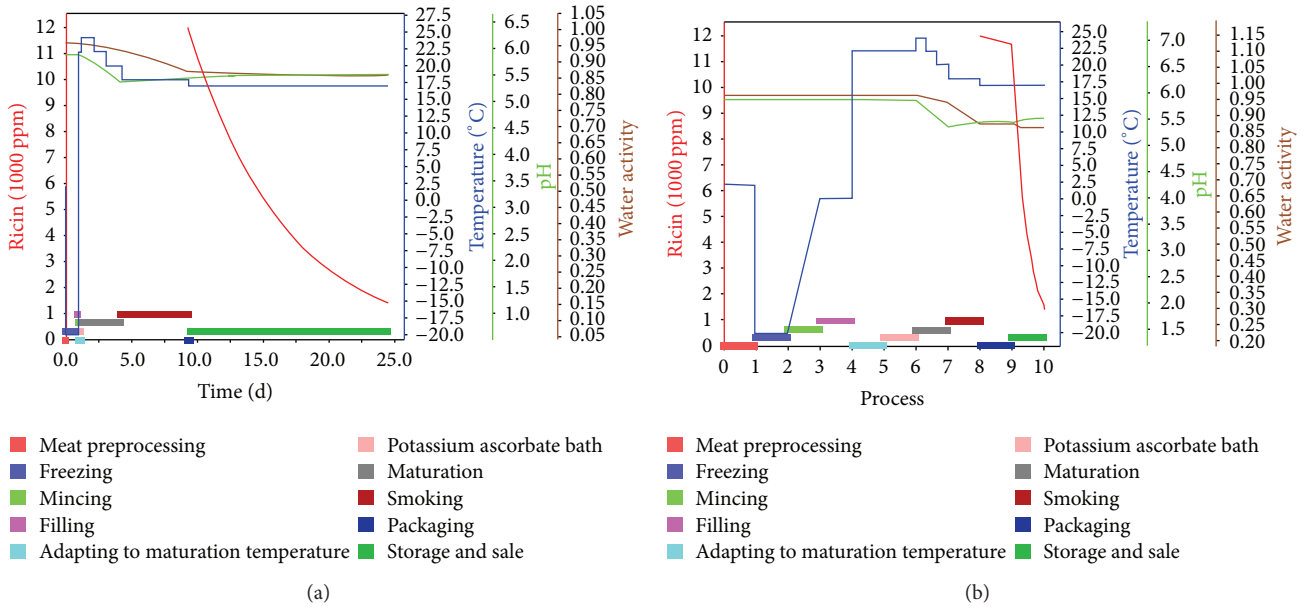

Figure 4: Visualisation of the change in processing parameters during the production of the minisalami. The coloured bars at the bottom of the graph show the different processing steps. The changes in temperature (blue), pH (green), and water activity (brown), as well as the inactivation curve of ricin (red), are shown as lines. The food processing chain is depicted as actual time series (a), for a clearer view on process steps, showing all process steps with equally wide bars (b).

Table 5: Contamination scenarios, calculated amount of active ricin left [mg] in minisalamis.

Process step	Day of consumption		
	7	15	30
Mincing	32.7	10.7	0.7
Maturation	33.5	10.9	0.8
Packaging	131.5	42.9	3.0

process was eaten a month later. In these cases, symptoms like nausea, vomiting, diarrhoea, and abdominal pain might occur [12]. On the other hand, if consumed only one week after production, each minisalami might still contain 131.5 mg active ricin which can lead to liver and renal dysfunction and death [12]. If salamis and packages were contaminated with ricin powder intoxication via inhalation is also possible. Depending on the particle size the lethal dose for inhalation ricin may be 50 times lower as was shown for monkeys [36].

4. Discussion

Models for the inactivation of ricin in foods were reviewed. Available models were implemented in PMM-Lab and used in a representation of a minisalami food process chain in FPL to predict the remaining amount of active ricin in the sausage.

4.1. Knowledge Base Generation

4.1.1. Inactivation of Ricin. Only a minority of the publications contained information about the inactivation of ricin in foods. Mainly, the word "inactivation" led to abstracts about ribosomes inactivated by toxins. As ricin is a model toxin and representative for a whole group of ribosome inactivating toxins, many articles published findings about other toxins like shiga toxin or saporin, in which only the ricin toxin group was referenced. Finally, a considerable number of texts dealt with the molecular structure of ricin and other toxins. Publications were excluded if they did not contain information about ricin in foods in title or abstract. As a consequence, the uncertainty associated with the models applied in this research is quite high as the amount of independent experimental data that can be used for model generation is low. This underlines that in case of real bioterroristic crisis situations there will be a need for information exchange between governmental authorities which have more in-depth in-house data. Here, the open-source software framework can be supportive as well.

In case of new research areas about which no data are available it might be of help to use data and models about similar toxins as "proxy models." This would not lead to exact predictions but might show into which direction research needs to go in order to find more quickly a solution.

4.1.2. Ricin Model Repository. The works of William Tolleson and colleagues are truly a treasure for modellers when trying to calculate the inactivation of ricin in different foods. The published inactivation rates could be used as parameters in model formulas during the implementation of models in PMM-Lab. Unfortunately, not all parameters were noted, perhaps for safety reasons. For example, parameter B in (2) has not been published. This made the estimation of two unknowns (B and E_a) necessary, leading to a greater variability. Of course, there was the possibility to use the published E_a values and simply recalculate all B values. But

in this case the estimation of both parameters was chosen in order to estimate a secondary inactivation model with PMM-Lab. The activation energies (E_a) shown above can only partly be called "in line" with those published by Jackson et al. [21].

Differences between E_a values might be a result of a different data basis: Jackson et al. [21] calculated the E_a using the original laboratory measurements and were able to derive the constant B empirically. In our case, both parameters were estimated applying the damped least square algorithm (also known as Levenberg-Marquardt algorithm) which is implemented in the PMM-Lab Model Fitting node. Due to these different parameter estimation approaches, the activation energies should not be used independent of the other parameter estimates.

Higher accordance with the published results could be obtained using the original Arrhenius equation. However, because of numerical reasons, a calculation of the covariance matrix was not possible with PMM-Lab.

4.1.3. Food Process Model Repository. One of the advantages for the user working with the FPL plug-in is that no programming is necessary. Nodes can be dragged and dropped in order to create a new processing step. It is also a modular system, allowing the user to reuse workflows with new data or to copy parts of workflows as a basis for a new processing chain. In this way, different contamination scenarios can be easily visualized and worst case scenarios can be identified. Having information on whole food processing chains saved in the food safety knowledge base becomes most advantageous when an estimate on the fate of an agent has to be given quickly, as, for example, in crisis situations.

4.1.4. Application of the Knowledge Base in Scenario Simulations. Above, several scenarios for the contamination of the minisalami food chain with ricin are described. Many more could easily be set up, for example, in order to consider food distribution in a more detailed way. However, data suitable for predictive modelling is frequently hard to find. In this case, a well-documented food processing chain containing slopes for temperature, pH value, and water activity was available. It could be directly implemented into FPL.

However, published inactivation rates for ricin in foods are scarce and mainly describe the thermal inactivation between 60 and 90°C [14, 21, 23, 24]. In the minisalami production chain, temperatures range from −20°C to 24°C, of which the most important process steps (maturation, smoking, storage, and sale) have temperatures between 17 and 24°C. Due to the lack of data, a rate for the inactivation of ricin in PBS at 25°C and pH 3.8 was used [21]. It was used in a primary model, meaning that changes in process temperature, pH, and water activity were not considered. For a suitable prediction of ricin inactivation, a secondary model for every interim product in the food chain would be necessary. As the model temperature is higher (25°C) than the food process temperatures (−20–24°C), this is not a fail-safe prediction and a higher proportion of ricin might remain active in the minisalami compared to the amounts calculated here.

However, the objective for generating scenarios in this paper was to show what is possible with publicly available data and published scientific literature. Risk assessors in the crisis and defence sector perhaps have access to unpublished data. The combination of PMM-Lab and FoodProcess-Lab is a powerful tool for which an easy-to-explain proof-of-principle example was provided.

The contamination of a food chain with a toxin is just one example. The growth of *Salmonella* during the production of accidentally contaminated minced chicken meat and the growth of *Listeria monocytogenes* in raw milk cheese are examples of bacterial contamination which can also be modelled with FPL and PMM-Lab, provided that necessary data and models are available.

4.1.5. Knowledge Base Consolidation. The creation of food safety knowledge bases is not only a technical or scientific challenge. Successful building-up and consolidation require acceptance and support by experimental researchers, modelling experts, and end users. This implies that several related issues have to be addressed in parallel with the technical implementation of knowledge bases. First, an internationally harmonized data exchange format for information related to food safety modelling would be of enormous value. Such a data exchange format would allow scientists to report their experimental data or models in a standardized way independent from the software used. This would improve transparency and quality control significantly, as it then becomes possible to provide unambiguous information on the data sets used for model generation, for example. It would also support existing food safety data collections like ComBase (http://www.combase.cc/) as software tools could be developed (or extended) that support information exchange. A first proposal for such a food safety information exchange format has recently been published at the OpenML for Predictive Modelling in Food community portal: http://sourceforge.net/projects/microbialmodelingexchange/. Second, the idea of sharing data and models within the scientific community needs to be promoted. In this sense, it would be beneficial if the opportunity to provide experimental data and models as supplementary materials to scientific publications would be widely advocated. This would also support the establishment of supervised community knowledge bases. These resources could in turn assign persistent URIs to data sets or models which would allow them to be referenced directly. The third relevant issue for knowledge base consolidation is related to the presentation and visualization of modelling results to the end users. The challenge here is that the latter demand easy-to-interpret answers to questions that usually require complex modelling efforts. Additionally, model based predictions might differ depending on the model used. Currently available solutions for illustration of model related uncertainties still impair end users' understanding. Also, the heterogeneity of user interfaces in existing and emerging software tools is challenging for end users. Here, open-source software projects could help to disseminate solutions with high usability and functionality as these components could then be reused by other software developers in their tools.

5. Conclusions

With this work, a proof-of-principle for a food safety knowledgebase applicable in bioterroristic crisis scenarios is delivered. FPL as a free-community resource can be used to represent, save, and exchange food processing chains. In combination with PMM-Lab, the inactivation of toxins as well as the tenacity of bacteria can be modelled along these food chains, providing means for exposure assessment. Once a knowledge base is built up, this will be of great help in crisis situations and beyond.

Conflict of Interests

The authors declare that there is no conflict of interests regarding the publication of this paper.

Acknowledgments

The authors would like to thank William Tolleson for an explanation of model generation in the cited paper and helpful comments on related publications. This work is part of the German national research project SiLeBAT and is funded by the Federal Ministry of Education and Research, Research Grant 13N11202.

References

[1] "Regulation (EC) No 178/2002 of the European Parliament and the Council of 28 January 2002 laying down the general principles and requirements of food law, establishing the European Food Safety Authority and laying down procedures in matters of food safety," 2002.

[2] A. A. Weiser, S. Gross, A. Schielke et al., "Trace-back and trace-forward tools developed Ad Hoc and used during the STEC O104:H4 outbreak 2011 in Germany and generic concepts for future outbreak situations," *Foodborne Pathogens and Disease*, vol. 10, no. 3, pp. 263–269, 2013.

[3] H. Mutlu and M. A. R. Meier, "Castor oil as a renewable resource for the chemical industry," *European Journal of Lipid Science and Technology*, vol. 112, no. 1, pp. 10–30, 2010.

[4] G. A. Balint, "Ricin: the toxic protein of castor oil seeds," *Toxicology*, vol. 2, no. 1, pp. 77–102, 1974.

[5] S. M. Bradberry, K. J. Dickers, P. Rice, G. D. Griffiths, and J. A. Vale, "Ricin poisoning," *Toxicological Reviews*, vol. 22, no. 1, pp. 65–70, 2003.

[6] V. R. Ambekar and K. K. Dole, "Detoxification of castor cake," *The Indian Journal of Dairy Science*, vol. 10, article 16, 1957.

[7] "Weapons of mass destruction (WMD)—Ricin," 2013, http://www.globalsecurity.org/wmd/intro/bio_ricin.htm.

[8] R. A. Zilinskas, "Iraq's biological weapons: the past as future?" *Journal of the American Medical Association*, vol. 278, no. 5, pp. 418–424, 1997.

[9] R. Crompton and D. Gall, "Georgi Markov—death in a pellet," *Medico-Legal Journal*, vol. 48, no. 2, pp. 51–62, 1980.

[10] Centers for Disease Control and Prevention, "Investigation of a ricin-containing envelope at a postal facility—South Carolina," *The Morbidity and Mortality Weekly Report*, vol. 52, no. 46, pp. 1129–1131, 2003.

[11] Centers for Disease Control and Prevention, "Recommendations of the CDC strategic planning workgroup biological and chemical terrorism: strategic plan for preparedness and response," *Morbidity and Mortality Weekly Report*, vol. 49, no. RR-4, pp. 1–14, 2000.

[12] J. Audi, M. Belson, M. Patel, J. Schier, and J. Osterloh, "Ricin poisoning a comprehensive review," *Journal of the American Medical Association*, vol. 294, no. 18, pp. 2342–2351, 2005.

[13] T. L. Bushueva and A. G. Tonevitsky, "The effect of pH on the conformation and stability of the structure of plant toxin-ricin," *FEBS Letters*, vol. 215, no. 1, pp. 155–159, 1987.

[14] L. S. Jackson, W. H. Tolleson, and S. J. Chirtel, "Thermal inactivation of ricin using infant formula as a food matrix," *Journal of Agricultural and Food Chemistry*, vol. 54, no. 19, pp. 7300–7304, 2006.

[15] A. U. Okorie and F. O. I. Anugwa, "The feeding value of roasted castor oil bean (*Ricinus communis*) to growing chicks," *Plant Foods for Human Nutrition*, vol. 37, no. 2, pp. 97–102, 1987.

[16] A. Falenski, A. Weiser, C. Thoens, B. Appel, A. Kaesbohrer, and M. Filter, "Food crisis scenario simulations improving food safety and security," in *Proceedings of the 9th Future Security, Security Research Conference*, K. Thoma, I. Häring, and T. Leismann, Eds., Fraunhofer, Stuttgart, Germany, 2014.

[17] A. Liberati, D. G. Altman, J. Tetzlaff et al., "The PRISMA statement for reporting systematic reviews and meta-analyses of studies that evaluate healthcare interventions: explanation and elaboration," *British Medical Journal*, vol. 339, Article ID b2700, 2009.

[18] P. Kästli and R. Hausch, "The viability of *Brucella abortus* Bang in different cheese varieties," *Schweizer Archiv für Tierheilkunde*, vol. 99, no. 11, pp. 638–644, 1957.

[19] M. Plommet, R. Fensterbank, L. Vassal et al., "Survival of *Brucella abortus* in ripened soft cheese made from naturally infected cows milk," *Le Lait*, vol. 68, no. 2, pp. 115–120, 1988.

[20] M. Filter, C. Thöns, J. Brandt et al., "A community resource for integrated predictive microbial modelling (PMM-Lab)," in *Proceedings of the 5th International Workshop Cold Chain Management*, 2013.

[21] L. S. Jackson, Z. Zhang, and W. H. Tolleson, "Thermal stability of ricin in orange and apple juices," *Journal of Food Science*, vol. 75, no. 4, pp. T65–T71, 2010.

[22] X. He, S. Lu, L. W. Cheng, R. Rasooly, and J. M. Carter, "Effect of food matrices on the biological activity of ricin," *Journal of Food Protection*, vol. 71, no. 10, pp. 2053–2058, 2008.

[23] M. Levy and A. E. Benaglia, "The influence of temperature and pH upon the rate of denaturation of ricin," *The Journal of Biological Chemistry*, vol. 186, no. 2, pp. 829–847, 1950.

[24] W. H. Tolleson, L. S. Jackson, O. A. Triplett et al., "Chemical inactivation of protein toxins on food contact surfaces," *Journal of Agricultural and Food Chemistry*, vol. 60, no. 26, pp. 6627–6640, 2012.

[25] T. L. Bushueva and A. G. Tonevitsky, "Similarity of protein conformation at low pH and high temperature observed for B-chains of two plant toxins: ricin and mistletoe lectin 1," *FEBS Letters*, vol. 229, no. 1, pp. 119–122, 1988.

[26] A. H. Geeraerd, V. P. Valdramidis, and J. F. van Impe, "GInaFiT, a freeware tool to assess non-log-linear microbial survivor curves," *International Journal of Food Microbiology*, vol. 102, no. 1, pp. 95–105, 2005.

[27] ComBase, DMFit Web Edition, Norwich, UK, Institute of Food Research, 2013, http://www.combase.cc/index.php/en/component/content/article/2-uncategorised/136-dmfit-web-edition.

[28] ComBase, *ComBase Predictor*, Institute of Food Research, Norwich, UK, 2013, http://modelling.combase.cc/ComBase_Predictor.aspx.

[29] USDA, *Pathogen Modeling Program (PMP) Online*, USDA, Wyndmoor, Pa, USA, 2003, http://pmp.errc.ars.usda.gov/PMPOnline.aspx.

[30] DTU Aqua, *Seafood Spoilage and Safety Predictor (SSSP)*, 3rd edition, 2009.

[31] FRISBEE, *The Food Refrigeration Innovations for Safety, Consumers' Benefit, Environmental Impact and Energy Optimisation along the Cold Chain in Europe Project*, 2013, http://www.frisbee-project.eu.

[32] FDA, *CARVER + Shock Manufacturing*, 2nd edition, 2007.

[33] M. J. Nauta, "A modular process risk model structure for quantitative microbiological risk assessment and its application in an exposure assessment of *Bacillus cereus* in a REPFED: RIVM," Tech. Rep. 149106007, 2001.

[34] M. J. Nauta, "Modelling bacterial growth in quantitative microbiological risk assessment: is it possible?" *International Journal of Food Microbiology*, vol. 73, no. 2-3, pp. 297–304, 2002.

[35] J. Kabisch, R. Pichner, and M. Gareis, "Tenazitätsstudie im Hinblick auf pathogene Mikroorganismen; Mykotoxinbelastung schimmelpilzgereifter Produkte (Minisalamis)," Abschlussbericht, Max Rubner-Institut, 2009.

[36] C. L. Wilhelmsen and M. L. M. Pitt, "Lesions of acute inhaled lethal ricin intoxication in rhesus monkeys," *Veterinary Pathology*, vol. 33, no. 3, pp. 296–302, 1996.

Hindawi Publishing Corporation
BioMed Research International
Volume 2015, Article ID 918631, 12 pages
http://dx.doi.org/10.1155/2015/918631

Research Article

Biometrics Analysis and Evaluation on Korean *Makgeolli* Using Brainwaves and Taste Biological Sensor System

Yong-Sung Kim[1] and Yong-Suk Kim[2]

[1] *Division of Computer Science & Engineering, Chonbuk National University, Jeonju 561-756, Republic of Korea*
[2] *Department of Food Science and Technology, Chonbuk National University, Jeonju 561-756, Republic of Korea*

Correspondence should be addressed to Yong-Suk Kim; kimys08@jbnu.ac.kr

Received 9 September 2014; Accepted 31 October 2014

Academic Editor: Tai hoon Kim

There are several methods available in measuring food taste. The sensory evaluation, for instance, is a typical method for panels to test of taste and recognize smell with their nose by measuring the degree of taste characteristic, intensity, and pleasure. There are many issues entailed in the traditional sensory evaluation method such as forming a panel and evaluation cost; moreover, it is only localized in particular areas. Accordingly, this paper aimed to select food in one particular area, and compare and review the content between sensory evaluations using a taste biological sensor, as well as presenting an analysis of brainwaves using EEG and finally a proposal of a new method for sensory evaluation. In this paper, the researchers have conducted a sensory evaluation whereas a maximum of nine points were accumulated by purchasing eight types of rice wine. These eight types of *Makgeolli* were generalized by generating multidimensional data with the use of TS-5000z, thus learning mapping points and scaling them. The contribution of this paper, therefore, is to overcome the disadvantages of the sensory evaluation with the usage of the suggested taste biological sensor system.

1. Introduction

Recently, many strategic plans have been proposed to globalize Korean food. Yet, there were various issues to take Korean food globally in accordance with such proposals. Not only has the degree of taste, characteristic, intensity, and pleasure formed the backbone of taste for the actual food, but also taste differs depending on the country and regional environment. Because a lot of time and cost are involved in researching and analyzing such conditions, new alternative plan is required to globalize Korean food [1].

In this paper, in order to overcome human limit and economic feasibility with regard to sensory evaluation, comparing and analyzing evaluation results between the taste biological sensor system (*TS-5000z)* and sensory evaluation of panels with physicochemical analysis have been conducted.

Subsequently, it continued to analyze the results of brainwaves of panels to resulting materials of *TS-5000z* to draw out standardized results of characteristics and intensity to a certain degree that forms the backbone of taste.

Standardization and taste measurement are needed in order to globalize alcoholic beverages making it commercially available everywhere. In relation to the case of European wines, enhancing the product's value and improved productivity is regarded through its taste specialization by its brand. *Makgeolli*, for thousands of years, is one of the most marketable traditional alcoholic beverages in Korea.

There were especially made adjective-expressions for sensory evaluation that are well developed in the Korean language, hence, the existence of numerous adjective terms to express the taste of *Makgeolli*. According to the previous pilot research, with regard to the mutual similarities of the pairs of terms, we can reach the realization of the hardship of formulating complete sets with small number of adjectives that can generally be used to express all kinds of Korean *Makgeolli*.

Makgeolli is an alcoholic drink made with rice, wheat flour, barley, corn, and sweet potato as major fermenting materials and thereafter fermented with *Koji* or *Nuruk* [1, 2]. The physicochemical and taste qualities of this drink depend

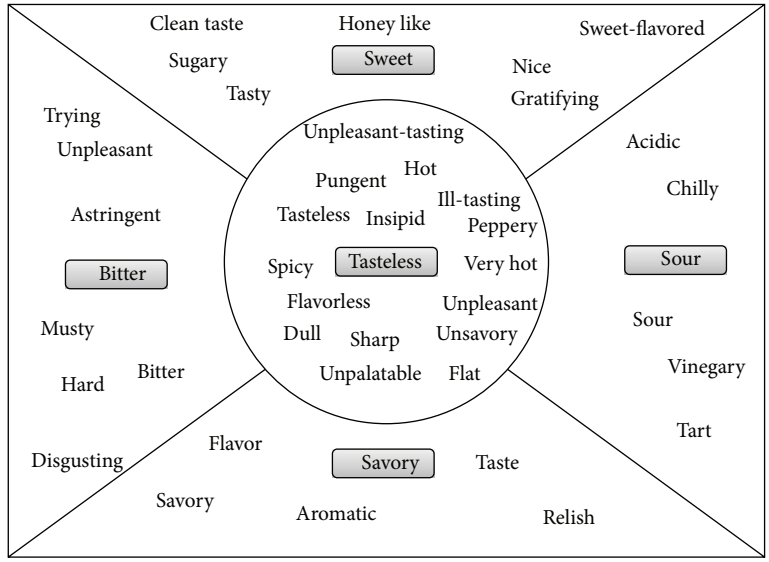

Figure 1: Type of taste information.

on the making materials, heating methods, and *Nuruk,* as well as the produced area [3]. In order for this drink to maintain its quality characteristics, *Makgeolli* has to be heated at 62–65°C for 30 minutes, preventing the drink from being altered for a long period of time to be able to keep its flavor and balanced taste. Sterilized *Makgeolli*, however, has weaknesses such as death of useful microbes, heated flavor, and a feeling of refreshment [3, 4].

This paper, therefore, concentrates on the elicitation of regional properties found in *Makgeolli* through the taste correlation between the electroencephalographic data of sensual test and taste biological sensor data.

Accordingly, by analyzing correlation of physicochemical analysis and sensory evaluation of *Makgeolli* with *TS-5000z* analysis results and by comparing analyzed results of brainwaves of panels based on such findings, it showed that it has the capability to replace the sensory evaluation as a scale if complementary scale is proposed for the analyzed results of *TS-5000z*.

2. Related Works

2.1. Taste-Adjectives. The taste is often described as a sensory reaction that is caused by the chemical stimulus. In order to recognize the taste, materials are firstly dissolved in the saliva that stimulates gustatory cells, hence signaling the cerebrum. Hereafter, the activity takes about a minute to taste. After eating the food, the taste lingers for 30 seconds.

Scale describing and introducing a particular product in qualitative and quantitative measures is called a scale method. Four basic tastes in Figure 1 are the baseline for dimensions in accordance with "imputed characteristic to a certain taste [5, 6]."

Here, the closer the concept of a particular adjective is to a traditional taste, the closer that concept gets to the baseline. However, it is difficult to argue this type of ordering as it is affiliated with dimensions in accordance with imputed characteristic to a certain taste.

Since quantitative description is defined with characteristics and intensity of appearance, smell, taste, and physical properties of a particular product, it is typical to understand taste in terms of physiological base and taste-adjectives formed in its semantics.

There is a point to consider when classifying the properties of *Makgeolli*: although a certain taste of its property is generally classified as good, it can still be recognized as unpleasant if it shows more than the required specific concentration.

2.2. Clustering Algorithm. Taste evaluation scale development using adjective pairs is extremely small and although there have been cases of using food taste as evaluation scale, it proved to be unsuccessful. In order to develop adjective scale that is to be used in qualitative sensory evaluation of actual taste, it is necessary to use correlation of adjectives to analyze factor analysis and congregation analysis and congregate adjectives expressing positive taste, negative taste, food texture, and heat level. In general, congregation is defined as follows.

Let us say that the sample $S = \{x_1, x_2, \ldots, x_n\}$ is given, which satisfies the below conditional equation, a subset of $C = \{S_1, S_2, \ldots, S_c\}$:

$$S_i \neq \varnothing, \quad (i = 1, \ldots, c)$$

$$S_i \cap S_j = \varnothing, \quad (i, j = 1, \ldots, c,\ i \neq j)$$

$$\bigcup_{i=1}^{c} = S. \tag{1}$$

Affiliated variables are defined in expression (2) and congregationl number in expression (3). Each congregation uses variables that show the degree of affiliation. Affiliated variable m_{ij} shows the degree of affiliation of x_i toward x_j.

Affiliated variables should satisfy the following conditional equation:

$$0 \le m_{ij} \le 1,$$
$$\sum_{j=1}^{k} m_{ij} = 1, \quad (2)$$
$$\sum_{i=1}^{N} m_{ij} < N.$$

Stirling number may be utilized to count different types of congregations. Stirling number is a conditional number from dividing objects of N onto K group. Therefore, Stirling number can be defined cyclic expression as follows:

$$S(N, N) = 1, \quad k = 1 \text{ or } N$$
$$\text{otherwise,} \quad (3)$$
$$S(N, k) = S(N-1, k-1) + kS(N-1, k).$$

In this paper, termite colony algorithm is used to congregate adjectives used to describe *Makgeolli*. Termite colony algorithm is based on the probability value of termite behavior. The aim is to find a suitable initial congregation required for k-means congregation using termite colony algorithm. Through termite search, estimating sample density within congregation is possible, and this estimated initial set suitable for density influences congregational functions (Algorithm 1).

2.3. Samples and Analysis Biometrics. With the purpose of experimenting, 12 commercialized *Makgeolli* samples (unsterilized = 5, sterilized = 7) produced in South Korea were purchased and maintained at 4°C refrigerator. The five unsterilized commercial *Makgeolli* samples were categorized as US1, US2, US3, US4, and US5. On the other hand, seven sterilized samples were categorized as S1, S2, S3, S4, S5, S6, and S7 [7].

The physicochemical qualities of *Makgeolli* samples such as pH, aminotype nitrogen, titratable acidity, and soluble solid contents were tested [8, 9]. In the case of sensory testing, graduate and undergraduate students (n = 25) from the Department of Food Science and Technology in Chonbuk National University were introduced with the objective and methodology prior to the test. The samples were tested using a 9-point hedonic scale ranging from "really like" (scale 9) to "really dislike" (scale 1). Properties like turbidity, color, flavor, sweetness, sourness, bitterness, thickness, cooling sensation, and balance were evaluated for the sensory test [9].

The data was treated using the statistical analysis system (SAS, 1998) package software for the analysis of variance and Duncan's test. All analyses were conducted in triplicate except for the sensory test that was measured by 25 students. The statistical significance was established at $P < 0.05$.

2.4. Brainwaves. Brainwave research with regard to human emotional change has been relatively developed. This research used a dimensional approach, derived from the cognitive theories, which determines a person's state of mind in terms of dimension. The common dimensions are determined through two types: the valence of emotion, reflecting either positive or negative emotions, and the arousal level of emotion, reflecting either active or passive emotion [6, 8]. Figure 2 is a 2D valence-arousal emotional model. The model shows more diversified and generalized expressions compared to discrete emotion approaches.

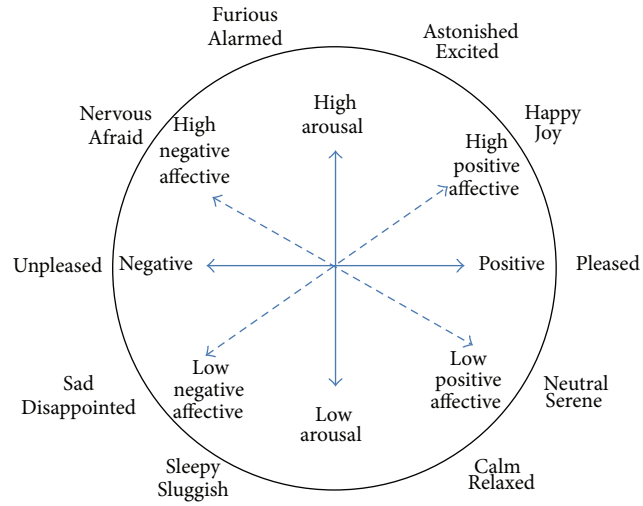

Figure 2: Valence-arousal emotional model.

EEG (electroencephalogram) is a brain activity classified with brainwaves that emit electric flow which is generated when signals are sent out into the cerebral nerves through the nervous system. When measuring brainwaves, it is possible to obtain an exceptionally complicated type of analogue waveform as seen in the valence-arousal emotional model. It is considered as the raw data of EEG. The raw data, afterwards, were transformed into digital data [10]. The digital data, subsequently, were transformed into a power spectrum, whereas it was also utilized for data analysis.

Power spectral analysis is a mathematical approach employed in order to quantify EEG. It does not, however, provide a biophysical model of the EEG generation. The purpose of the analysis is for the decomposition of signals into its constituting frequency components (e.g., EEG). FFT (fast Fourier transform), on the other hand, is known as a widely used method in acquiring data such as the EEG spectrum [11–13].

FFT algorithm describes signals as linear superposition of Sines and Cosines characterized by their frequency in the equation as seen below expression (4). Consider

$$x(t) = \int_{-\infty}^{+\infty} X(f)\, e^{i2\pi ft} df. \quad (4)$$

The power spectrum, also known as power density spectrum, demonstrates the distribution of power or variance over the frequency components of a signal. It is also known as a Fourier transform of the autocorrelation function.

Input: setting of termite cluster value
Output: The initial cluster $Z = \{z_1, z_2, \ldots, z_6\}$ // initial value termite cluster
Begin:
$x_{\text{mean}} = \left[\max(x_i) - \min(x_i)\right]/2$ // center point of the entire sample
$y_{\text{mean}} = \left[\max(y_i) - \min(y_i)\right]/2$
while (TRUE) {
Termite_Search_Path() // / probability path search
if $(t_i = |(x_n/6)/2|)$ break; // t_i: termite colony $|(x_n/6)/2|$: sample space density
}
for (j = 1 to 7) {
Swap (z_i, t_i) // swap z_i to t_i.
}
$z_7 = x_{\text{mean}}, y_{\text{mean}}$ // assign center point of entire sample space to z_7.
Initial_Z() // initialize the colony of number of k
$Z = \{z_1, z_2, \ldots, z_7\}$
while (TRUE) {
for (i = 1 to n) //x_i// position at the nearest cluster center
if (old_Z = new_Z) break; // compare with the previous cluster center
for (j = 1 to k) z_i replace z_j // setting cluster center
}
End:

Algorithm 1: TCA K-mean's algorithm.

Table 1: Type and feature of brainwaves.

Type	Frequency	Normality
δ (delta)	0.5~4 Hz	Hypnoidal
θ (theta)	4~7 Hz	Slow wave sleep
α (alpha)	8~12 Hz	Stable wave
Mid-β (midbeta)	16~20 Hz	Concentrate stable wave
β (beta)	21~30 Hz	Action stress wave
γ (gamma)	30~50 Hz	Arousal and excitement

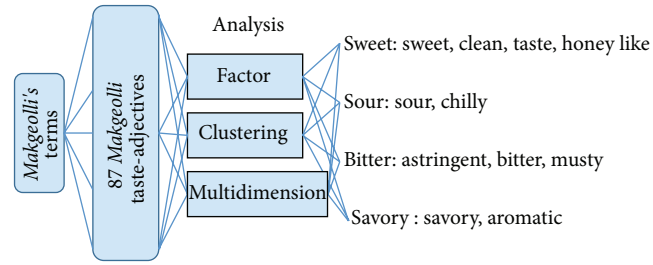

Figure 3: Four catalog of *Makgeolli* taste-adjectives.

The degree of the brain activity causes the shape of brainwaves to react differently. If the brain works more actively, it produces a wider frequency bandwidth of brainwaves as seen in Table 1.

One of the most used methods in the analysis of brainwaves is the power spectrum analysis [12, 13]. This study, hence, mainly utilized the power spectrum analysis since it is a remarkably adequate method in terms of the time series frequency analysis of the raw data.

3. Experimental Results and Discussion

3.1. Representative Taste-Adjective. Before evaluating eight different types of *Makgeolli* purchased locally through sensory evaluation and *TS-5000z* taste sensor, there was little preliminary work that needs to be done. First was the selection of *Makgeolli* that sells the most locally. Secondly, get 20 students to sort out 87 taste-adjectives that were used on Internet and in Korean dictionary. Thirdly, out of the 87 selected taste-adjectives, 45 of them were sorted out and were placed into final four categories. Lastly, through factor analysis and congregation algorithm as well as multidimensional analysis, we extracted 12 taste-adjectives for *Makgeolli*. The processed result is shown in Figure 3.

The outcome of the experiment leads into four representative *Makgeolli*-adjectives describing taste: sweet, sour, bitter, and savory.

As shown above, among various *Makgeolli* types in adjective dimension, finding the *Makgeolli* that is preferred by foreigners should help narrowing down the taste dimension of *Makgeolli* from adjective dimension for exporting the product globally.

3.2. Physicochemical Characteristics of Makgeolli. The pH level of *Makgeolli*, as an alcoholic drink, is a significant factor for its preservation and fermentation process. The pH of S1 *Makgeolli* sample, as seen in Figure 4, had the lowest level with 3.88 while that of S4 sample had the highest pH with 4.49.

Titratable acidity, on the other hand, serves as a vital indicator influencing the taste and flavor of a drink. The lactic acid bacteria and yeast found in *Makgeolli* produce

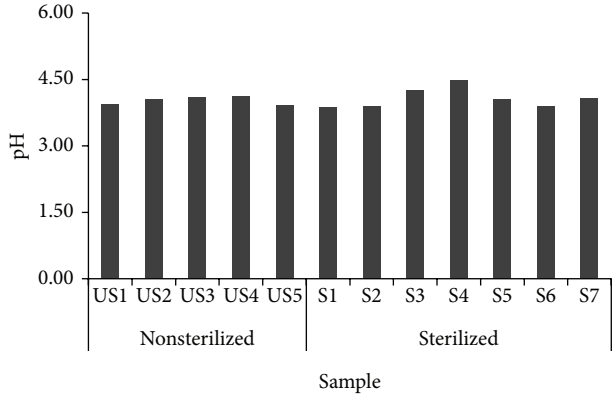

Figure 4: pH of 12 *Makgeolli* samples produced in South Korea.

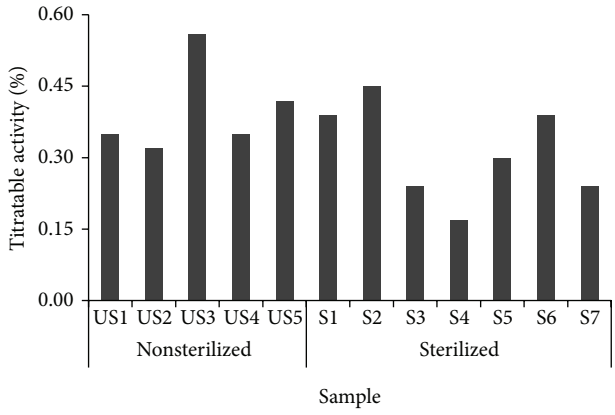

Figure 5: Titratable acidity of 12 *Makgeolli* samples produced in South Korea.

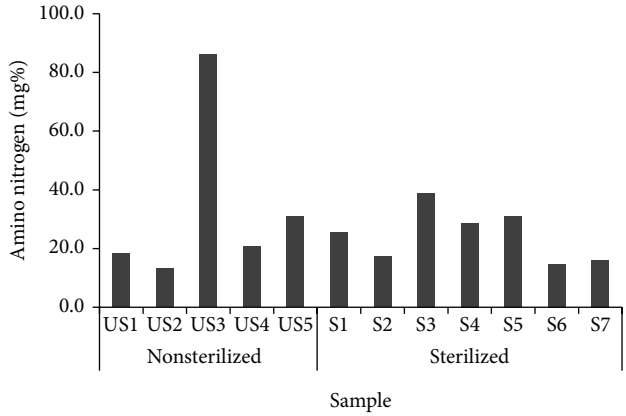

Figure 6: Aminotype nitrogen contents of 12 *Makgeolli* samples produced in South Korea.

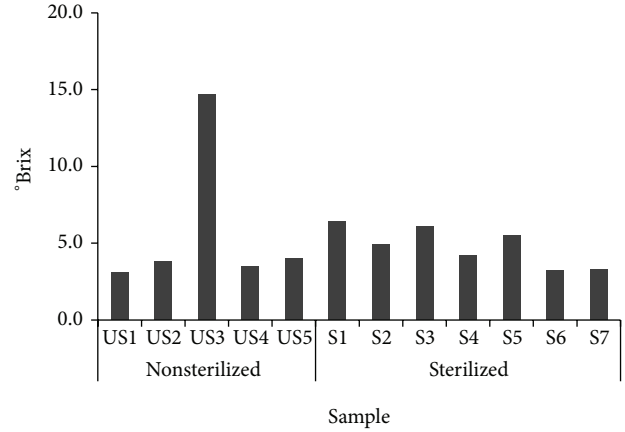

Figure 7: Soluble solid contents of 12 *Makgeolli* samples produced in South Korea.

organic acid that can be increased within the process of fermentation [14]. The result in Figure 5 shows that the titratable acid content of the S4 sample (sterilized) had the lowest percentage with 0.17%. Meanwhile, the US3 which got 0.56 percent had the highest percentage within the samples.

The aminotype nitrogen contents were illustrated in Figure 6 resulting with US3 (sterilized) with 86.19 mg% being the highest among the samples while the other samples ranged from 13.08 to 31.06 mg%.

In Figure 7, the soluble solid contents of US3 (unsterilized), S1, and S3 (sterilized) obtained 14.7, 6.4, and 6.1°Brix.

3.3. Sensory Test on Domestic Makgeolli Samples Using Taste Biological Sensor. Taste biological sensor, an electronic equipment, has a similar structure as the taste bud of a human tongue and detects taste ingredient, which is sent to a computer in corresponding electrical signal which compiles data.

The taste was analyzed using *TS-5000z*, a taste biological sensor from Japan. An available taste biological sensor system found in Daesang Research Center from Incheon, Korea, was used for equipment testing as seen in Figure 8. The system consists of five taste biological sensors, namely, sourness, umami, bitterness, saltiness, and astringency. There were also three aftertaste sensors classified as bitterness, astringency, and umami [15].

The method for converting multidimensional data measured by *TS-5000z* to a taste form recognized by human is important. In other words, the required implementation of mapping function of four (4) adjective scales of *Makgeolli* abstracted and measured from *TS-5000z*, and in order to verify these brainwaves of panels are used as in Figure 9.

In this paper, eight different types of *Makgeolli* have been purchased that are currently sold locally to analyze physicochemical and microbiological properties. Afterwards, a 9-point scale sensory evaluation is conducted, and using eight types of *Makgeolli* evaluated by these panels, multidimensional data has been created from *TS-5000z* and studied through mapping function.

Using the statistical analysis system (SAS, 1998) package software, the data was analyzed for the analysis of variance and Duncan's test. All analyses were carried out in triplicate

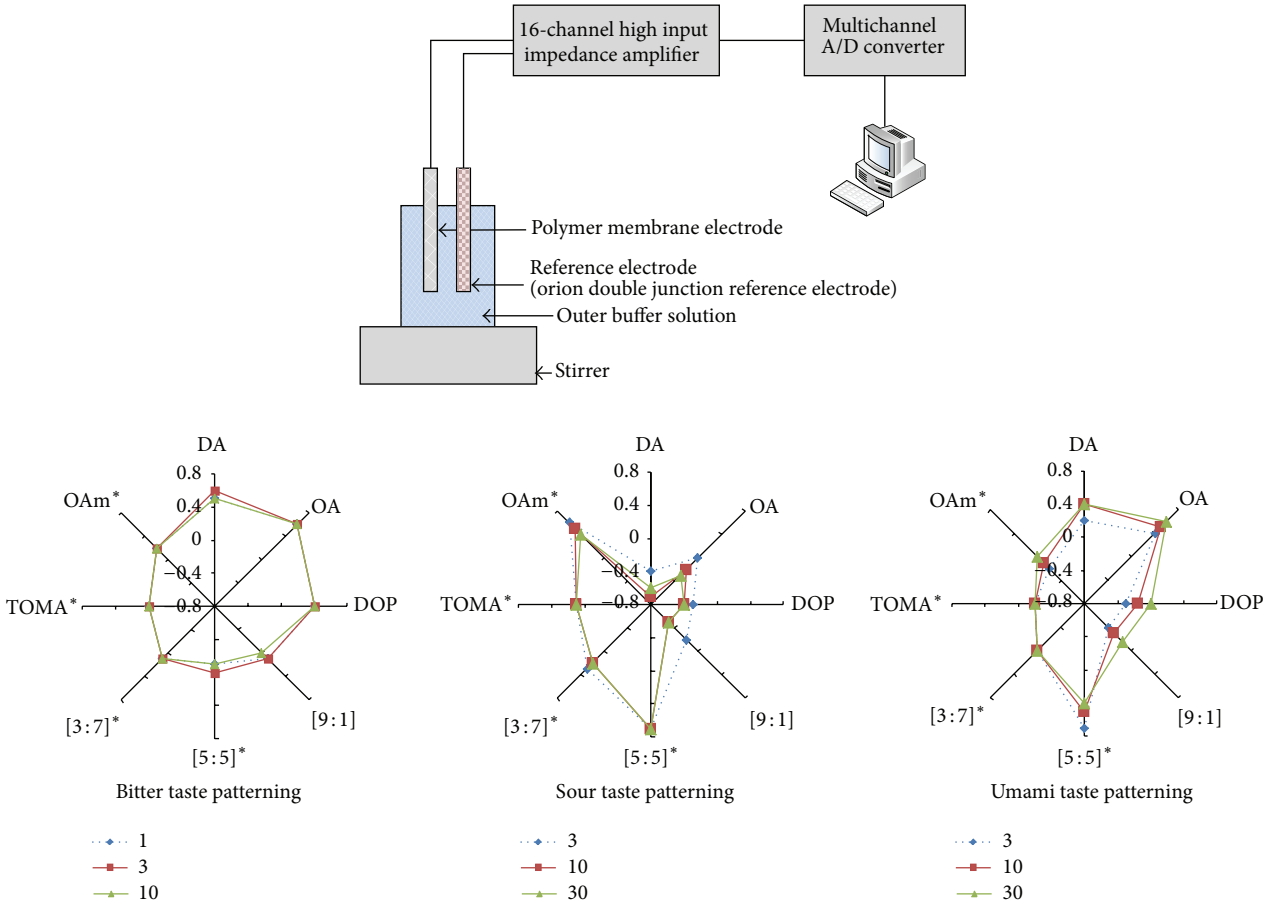

Figure 8: Taste biological sensor (*TS-5000z*) and multidimensional data.

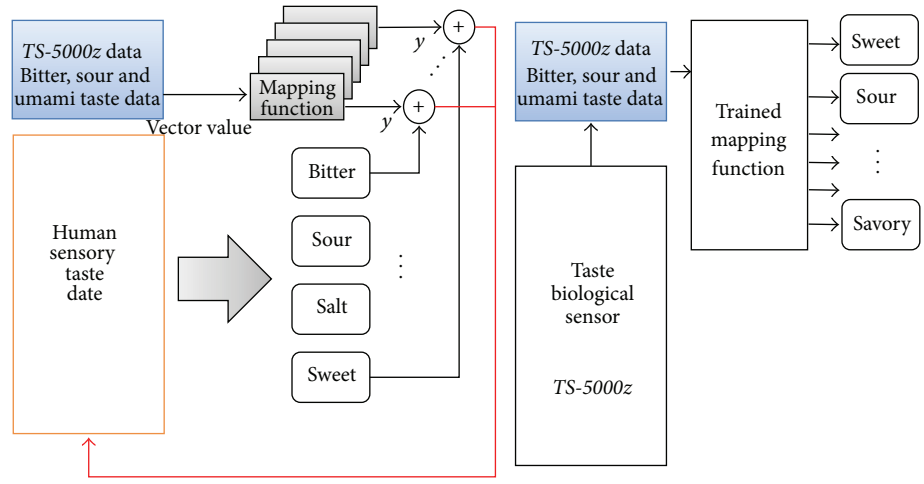

Figure 9: Structure of learning process.

with the exception of the sensory evaluation that was measured by 12 determinations. The significance was established at $P < 0.05$.

The results on the 12 domestic *Makgeolli* samples using the taste biological sensor system were shown in Table 2. The samples US2 (6.00 ± 2.11), US4 (5.80 ± 1.99), S1 (5.50 ± 1.43), and S2 (5.50 ± 1.27) were significantly high in balance. Moreover, the samples S6, S2, and S1 (sterilized) scored higher with 6.40, 6.00, and 5.70 compared to other samples. The significant differences were not observed between sterilized and unsterilized samples in balance scores of sensory test within the use of this system.

Table 2: Sensory test of 12 *Makgeolli* samples produced in South Korea using taste biological sensor.

Samples	Turbidity	Color	Flavor	Sweetness	Sourness	Bitterness	Thickness	Cooling sensation	Balance
US1	5.90 ± 1.10^{abc}	6.00 ± 0.82^{bcd}	5.50 ± 1.08^{b}	4.70 ± 1.25^{abc}	5.20 ± 1.69^{ab}	5.60 ± 1.51^{a}	5.10 ± 0.74^{a}	6.10 ± 1.10^{ab}	5.10 ± 1.10^{abc}
US2	6.50 ± 1.96^{a}	7.60 ± 1.43^{a}	7.10 ± 1.20^{a}	5.80 ± 1.93^{ab}	5.80 ± 1.69^{a}	5.70 ± 1.77^{a}	5.00 ± 2.31^{ab}	5.40 ± 1.71^{abcd}	6.00 ± 2.11^{a}
US3	4.30 ± 1.49^{d}	3.70 ± 1.83^{f}	4.90 ± 1.79^{b}	3.40 ± 1.58^{c}	3.00 ± 1.56^{c}	3.10 ± 1.29^{c}	4.50 ± 2.46^{ab}	3.20 ± 2.10^{ef}	3.70 ± 1.34^{cde}
US4	6.60 ± 2.32^{a}	7.50 ± 1.08^{a}	7.10 ± 0.88^{a}	6.10 ± 2.02^{a}	5.60 ± 2.50^{a}	5.40 ± 2.37^{a}	4.50 ± 2.01^{ab}	5.20 ± 2.25^{abcd}	5.80 ± 1.99^{ab}
US5	6.10 ± 1.37^{ab}	7.00 ± 1.41^{ab}	2.80 ± 1.87^{c}	3.10 ± 1.66^{c}	3.20 ± 2.15^{bc}	3.20 ± 2.10^{bc}	3.20 ± 2.10^{b}	4.10 ± 2.60^{cdef}	3.10 ± 1.97^{e}
S1	5.20 ± 0.92^{abcd}	5.20 ± 1.14^{cde}	5.90 ± 1.10^{ab}	5.80 ± 1.23^{ab}	5.10 ± 2.13^{abc}	5.00 ± 1.49^{ab}	5.10 ± 1.60^{a}	5.70 ± 1.64^{abc}	5.50 ± 1.43^{ab}
S2	4.50 ± 0.85^{cd}	5.10 ± 0.99^{de}	5.90 ± 1.52^{ab}	5.90 ± 0.88^{ab}	5.40 ± 1.84^{a}	5.60 ± 1.65^{a}	5.10 ± 1.45^{a}	6.00 ± 1.76^{ab}	5.50 ± 1.27^{ab}
S3	6.20 ± 1.55^{ab}	6.50 ± 1.43^{abc}	5.70 ± 1.64^{ab}	5.50 ± 1.84^{ab}	4.40 ± 1.84^{abc}	4.70 ± 2.16^{abc}	4.00 ± 1.76^{ab}	4.30 ± 1.89^{bcdef}	4.90 ± 1.45^{abcd}
S4	5.10 ± 2.38^{abcd}	4.20 ± 2.10^{ef}	6.00 ± 1.76^{ab}	4.50 ± 2.07^{abc}	4.10 ± 3.00^{abc}	4.10 ± 2.28^{abc}	3.90 ± 1.97^{ab}	2.90 ± 1.73^{f}	3.50 ± 1.43^{de}
S5	5.90 ± 1.52^{abc}	5.30 ± 1.57^{cde}	4.80 ± 1.87^{b}	4.30 ± 2.41^{bc}	4.20 ± 3.16^{abc}	4.20 ± 2.30^{abc}	3.60 ± 1.78^{ab}	3.70 ± 2.16^{def}	4.20 ± 1.69^{bcde}
S6	4.80 ± 1.14^{bcd}	4.90 ± 1.37^{def}	5.50 ± 1.08^{b}	5.20 ± 0.79^{ab}	4.60 ± 1.26^{abc}	5.00 ± 0.94^{ab}	5.40 ± 1.07^{a}	6.40 ± 1.17^{a}	5.30 ± 0.95^{ab}
S7	5.40 ± 0.97^{abcd}	5.50 ± 0.97^{cde}	6.00 ± 1.56^{ab}	5.70 ± 1.34^{ab}	5.20 ± 1.40^{ab}	5.10 ± 1.45^{a}	5.20 ± 1.23^{a}	5.00 ± 1.33^{abcde}	5.10 ± 1.66^{abc}

[a–f]Mean values with different superscripts in the same column are significantly different ($P < 0.05$).

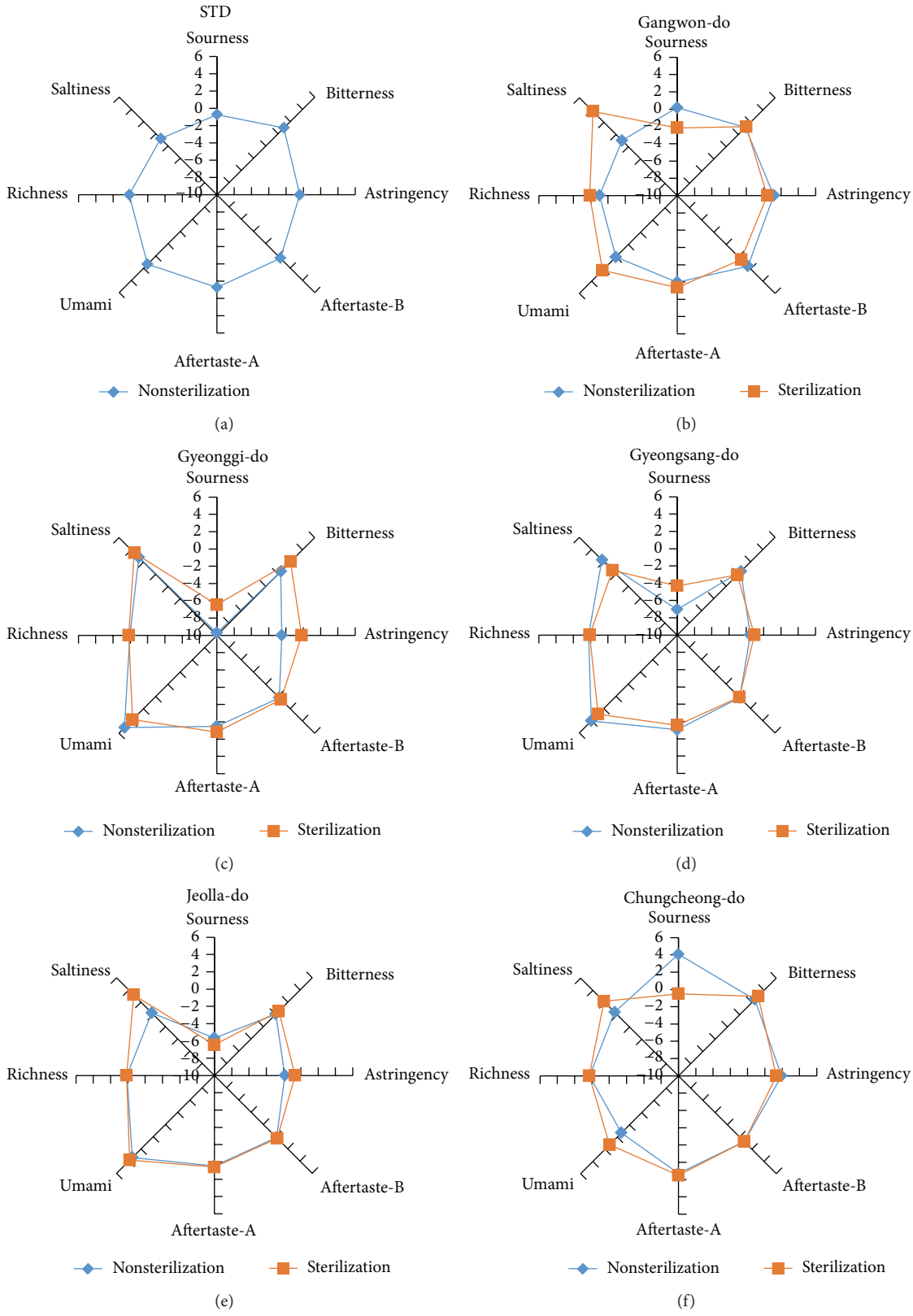

Figure 10: Taste results by taste biological sensor on 12 *Makgeolli* samples produced in South Korea.

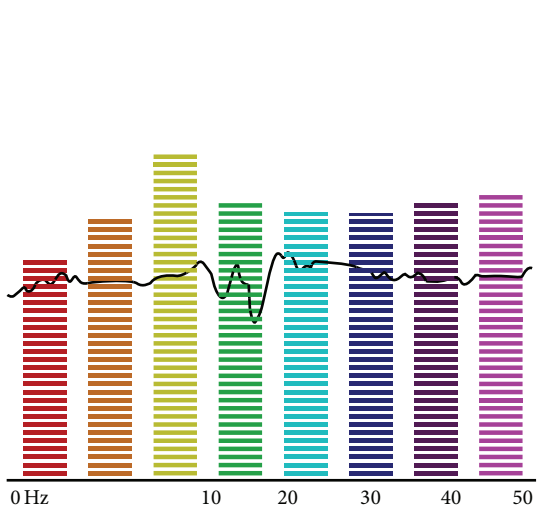

(a) Raw data

(b) Power spectrum

Attention	Meditation
60	64
60	64
43	48
43	56
47	56
44	57
54	61
...	...

(c) Excel data

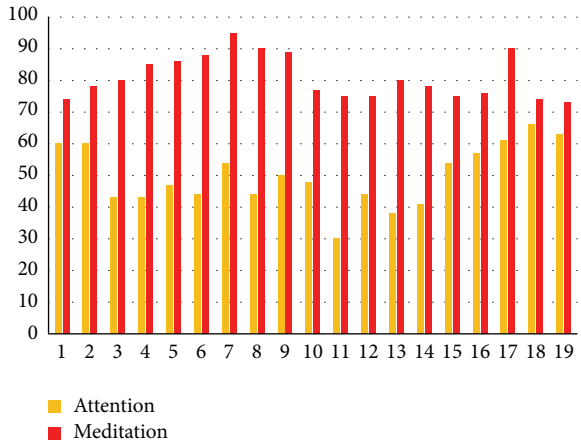

(d) Digital data

Figure 11: Digital transformation process.

3.4. Taste Biological Sensor Analyses on Makgeolli. The taste biological sensor was compared to a standard one. The standard sample which showed middle score in the sensory test was the standard sample CD1 (unsterilized). According to taste biological sensor test results, as shown in Figure 10, the sourness level showed significant distinction between WM1 (7.69) and BS1 (−23.84). Meanwhile, the sourness found in an unsterilized *Makgeolli* sample was generally higher than that in sterilized ones.

The bitterness found in the samples CJ1 (5.59), SJ1 (5.56), WR2 (5.47), WR1 (5.20), CW1 (5.13), and SD1 (5.03) was high. Umami and richness, on the other hand, found in the samples GS5, WR1, PG1, GS1, and SJ1 were higher than the other samples. The SD1 sample showed the highest score in umami with 6.65 and 0.83 in richness according to the taste biological sensor.

3.5. Correlation. The correlation analysis between the analytical value of physicochemical characteristics and sensory testing of Korean *Makgeolli* samplesusing the taste biological sensor was conducted.

The pH and titratable acidity (physicochemical characteristics), as shown in Table 3, showed high reverse correlation. The correlation analysis between physicochemical characteristics and sensory testing of Korean *Makgeolli* using the taste biological sensor showed that "titratable acidity" and "sourness, cooling sensation, and balance" have high correlation.

In addition, the criteria "sweetness-bitterness," "sourness-bitterness, thickness, cooling sensation, and balance," "bitterness-thickness, cooling sensation, and balance," "thickness- cooling sensation and balance," and "cooling sensation-balance" showed a strong correlation as shown in Table 3. Lastly, items between physicochemical characteristic

Table 3: Correlation analysis between physicochemical characteristic values and sensory test on Korean *Makgeolli*.

	pH	Titratable acidity	Aminotype nitrogen	Soluble solid	Lightness	Redness	Yellowness	Turbidity	Color	Flavor	Sweetness	Sourness	Bitterness	Thickness	Cooling sensation	Balance
pH	NA	**−0.910****	0.578	−0.038	0.033	0.498	0.141	0.35	−0.041	0.67	−0.353	**−0.828***	−0.738	−0.703	**−0.878****	**−0.815***
Titratable acidity		NA	−0.509	0.134	−0.136	−0.476	−0.466	−0.559	−0.132	−0.622	0.368	**0.913****	0.709	0.649	**0.801***	0.716
Aminotype nitrogen			NA	0.716	0.351	**0.933****	0.035	0.747	0.596	0.31	−0.101	−0.541	−0.477	**−0.835***	−0.676	−0.463
Soluble solid				NA	0.344	0.63	−0.146	0.387	0.617	0.073	0.266	0.109	0.122	−0.359	−0.162	0.073
Lightness					NA	−0.186	−0.072	0.463	0.362	0.291	−0.068	−0.049	−0.078	−0.14	−0.039	−0.084
Redness						NA	0.092	**0.879***	0.549	0.024	−0.099	−0.618	−0.491	**−0.877***	−0.669	−0.405
Yellowness							NA	0.48	0.539	0.291	0.306	−0.302	0.13	0.064	0.011	0.219
Turbidity								NA	**0.780***	0.105	−0.134	−0.603	−0.408	−0.649	−0.424	−0.242
Color									NA	0.11	0.481	−0.052	0.219	−0.201	0.057	0.337
Flavor										NA	0.252	−0.281	−0.075	−0.099	−0.368	−0.269
Sweetness											NA	0.648	**0.861***	0.595	0.626	0.807*
Sourness												NA	**0.898****	**0.829***	**0.891****	**0.841***
Bitterness													NA	**0.860***	**0.887****	**0.954****
Thickness														NA	**0.904****	**0.809***
Cooling sensation															NA	**0.932****

$^{*}P < 0.05$; $^{**}P < 0.01$. NA: not analysed.

Figure 12: Analysis results of brainwaves.

analysis and taste biological sensor showed a strong correlation score.

3.6. Brainwaves Detection. The EEG used in this research was produced by the American Neuroscience. The mindset of the said EEG has a series of advantages. Firstly, EEG can distinguish the state of brain; in other words, it can differentiate good state from bad state. Secondly, because EEG can analyze brainwaves in real-time, this paper analyzed brainwaves in a five-minute lapse after tasting *Makgeolli* of the panels. Lastly, because EEG outputs brainwaves in power spectrum form this has been digitized for utilization [16].

Analog data obtained from raw data of the panels' brainwaves have been converted from power spectrum form to digital data through FFT, which is then visualized through excel data as seen in Figure 11 [16, 17].

Power spectrum analysis shows change in the process from good state to bad state using raw data that is generated from time series, which is evaluated by the tasting of panels of the eight *Makgeolli* samples. Since numerical analysis of brainwaves with regard to selecting the *Makgeolli* changes over time, after a five-minute lapse from tasting *Makgeolli*, the intensity of taste is measured 10 times in one minute. In other words, within just two minutes, measuring was done. Figure 12 shows the tasting results of four panels who have consumed eight *Makgeolli* samples in two minutes.

As shown in Figure 12, *Makgeolli* samples 1, 2, 3, and 4 show good state whereas samples 7 and 8 show bad state, and 5 and 6 show the in-between state. This experiment result was almost in match with experiment result of *TS-5000z*.

4. Conclusion

It may be said that, strategically, coming up with a scale that can evaluate food's taste characteristic, intensity, and pleasure is one way to globalize Korean food. In general, representative method that evaluates taste is called sensory evaluation, where human recognizes food taste using the actual tongue. This however, in realistic sense, is used in only limited cases due to issues with forming panels and cost incurred in order to conduct sensory evaluation.

Accordingly, in this paper, artificial tongue from electronic equipment, in other words, suggests the method of utilizing taste biological sensor system in place of sensory evaluation. Firstly, it had chosen *Makgeolli* samples that are sold locally and congregated taste-adjectives used to describe chosen *Makgeolli* by applying it through termite colony theory.

Afterwards, the results of physics and chemical characteristic and sensory evaluation of *Makgeolli* have been compared with the measured result from the taste biological sensor and scaled abstract function in order to suggest a generalized scale.

Therefore, the degree of contribution this paper made was from suggesting a new paradigm that may replace sensory evaluation with taste biological sensor and a method that overcomes various shortcomings of sensory evaluation. Moreover, in order to obtain precise and exact result, it had provided a standardized scale of taste biological sensor by comparing tasting results of *Makgeolli*.

This study is a pioneer in contributing through the investigation between the correlation analysis of brainwaves in accordance with taste biological sensor evaluation and electroencephalographic data. For future researches, there would be an expansion and comparison in a selection of liquors, especially beer and wine, including the smell and color to statistically improve the taste biological sensor system. A foundation is established for the application of the taste biological sensor system in a specific area as an alternative to sensory evaluation.

Conflict of Interests

The authors declare that there is no conflict of interests regarding the publication of this paper.

Acknowledgments

This research was supported by research funds of Chonbuk National University in 2009 and Basic Science Research Program through the National Research Foundation of Korea (NRF) funded by the Ministry of Education, Science and Technology (no. 1201000870).

References

[1] D. H. Jung, *Historical Development of Korean Liquor*, Shinkwang Publishing, Seoul, Korea, 2004.

[2] I. S. Ryu, *We Enjoy the Taste of 101 Kinds of Makgeolli*, Notebooks, The Treetop (Woodemji), Seoul, Republic of Korea, 2010.

[3] Ministry of Agriculture, *Food and Rural Affairs, Introduction of Takju and Yakju*, Suhwasa, Seoul, Republic of Korea, 2012.

[4] C.-H. Baek, J.-H. Choi, H. S. Choi et al., "Quality characteristics of brown rice Makgeolli produced under differing conditions," *Korean Journal of Microbiology and Biotechnology*, vol. 41, no. 2, pp. 168–175, 2013.

[5] R. J. Larsen and D. M. Buss, *Personality Psychology*, McGraw-Hill, New York, NY, USA, 2002.

[6] H. M. Kim, "Comparative analysis of multi-cultural situations between Korea and Germany," in *Proceedings of the International Workshops on FRS*, Jeju, Republic of Korea, December 2013.

[7] S.-H. Kim, Y.-S. Kim, and Y.-S. Kim, "Correlational analysis of brain waves according to sensual evaluation on commercial Makgeolli," *International Journal of Bio-Science & Bio-Technology*, vol. 6, no. 1, pp. 95–100, 2014.

[8] H. J. Kim, K. H. Lee, H. I. Yong, and C. U. Jo, "Effect of UV-C and electron beam irradiation of on the quality of rice wine (Makgeolli)," *Korean Journal of Food Preservation*, vol. 20, no. 1, pp. 45–51, 2013.

[9] H.-E. Kim and Y.-S. Kim, "Comparison of quality characteristics and instrumental analysis on Korean Makgeolli," *International Journal of Bio-Science and Bio-Technology*, vol. 6, no. 1, pp. 123–128, 2014.

[10] J. S. Ahn, *Using Pattern Analysis of EEG Signals for Implementation of Game Interface*, Graduate School of Chung-Ang University, Seoul, South Korea, 2010.

[11] P. Ekman and M. J. Power, *Handbook of Cognition and Emotion*, John Wiley & Sons, Sussex, UK, 1999.

[12] A. C. Guyton and J. E. Hall, *Textbook of Medical Physiology*, Elsevier, Philadelphia, Pa, USA, 2005.

[13] C. W. James and J. W. Tukey, "An algorithm for the machine calculation of complex Fourier series," *Mathematics of Computation*, vol. 19, no. 90, pp. 297–301, 1965.

[14] C. W. Park, S. Y. Jang, E. J. Park, S. H. Yeo, O. M. Kim, and Y. J. Jeong, "Comparison of the quality characteristics of commercial Makgeolli type in South Korea," *Korean Journal of Food Preservation*, vol. 18, no. 6, pp. 884–890, 2011.

[15] K. Toko, "Taste sensor," *Sensors and Actuators, B: Chemical*, vol. 64, no. 1–3, pp. 205–215, 2000.

[16] J. Y. Kim, "EEG signal feature analysis of smart phone game user," in *Proceedings of the International Workshops on FRS*, 2013.

[17] K. S. Jung and Y. S. Choi, "Brain wave and user profile based learning content type recom-mendation in interactive e-learning environment," *International Journal of Smart Home*, vol. 6, no. 3, pp. 33–40, 2012.

Hindawi Publishing Corporation
BioMed Research International
Volume 2015, Article ID 535894, 9 pages
http://dx.doi.org/10.1155/2015/535894

Research Article

Quantification of Hepatorenal Index for Computer-Aided Fatty Liver Classification with Self-Organizing Map and Fuzzy Stretching from Ultrasonography

Kwang Baek Kim[1] and Chang Won Kim[2]

[1]*Department of Computer Engineering, Silla University, Busan 617-736, Republic of Korea*
[2]*Department of Radiology, School of Medicine, Pusan National University, Pusan National University Hospital, Busan 602-739, Republic of Korea*

Correspondence should be addressed to Kwang Baek Kim; gbkim@silla.ac.kr and Chang Won Kim; radkim@nate.com

Received 29 August 2014; Accepted 17 November 2014

Academic Editor: Tai-hoon Kim

Accurate measures of liver fat content are essential for investigating hepatic steatosis. For a noninvasive inexpensive ultrasonographic analysis, it is necessary to validate the quantitative assessment of liver fat content so that fully automated reliable computer-aided software can assist medical practitioners without any operator subjectivity. In this study, we attempt to quantify the hepatorenal index difference between the liver and the kidney with respect to the multiple severity status of hepatic steatosis. In order to do this, a series of carefully designed image processing techniques, including fuzzy stretching and edge tracking, are applied to extract regions of interest. Then, an unsupervised neural learning algorithm, the self-organizing map, is designed to establish characteristic clusters from the image, and the distribution of the hepatorenal index values with respect to the different levels of the fatty liver status is experimentally verified to estimate the differences in the distribution of the hepatorenal index. Such findings will be useful in building reliable computer-aided diagnostic software if combined with a good set of other characteristic feature sets and powerful machine learning classifiers in the future.

1. Introduction

Fatty liver or hepatic steatosis is a common histologic finding in human liver biopsy specimens, and nonalcoholic fatty liver disease (NAFLD) is the most common cause of fatty liver [1]. The prevalence of NAFLD in the general population is estimated to be 20–30% in Western countries [2], but this number is considerably higher in people with type 2 diabetes or obesity [3] and recent report found a similar tendency in Asian countries as well [4]. In a majority of patients, NAFLD is associated with metabolic risk factors such as obesity, diabetes mellitus, and dyslipidemia [5]. NAFLD is not only a liver disease but also an early mediator that reflects a metabolic disorder [6].

Liver biopsy is the gold standard for the quantification of hepatic steatosis. However, it is difficult for most patients to accept it due to its invasiveness and a significant degree of sampling error [7].

Ultrasonography (US) is an appealing technique compared with computed tomography (CT) and magnetic resonance imaging (MRI) in detecting the fatty infiltration of the liver because of its simplicity, low cost, noninvasive nature, and widespread availability.

However, almost always, the use of US methodologies in diagnosis suffers from several limitations including operator dependency, subjective evaluation, and limited ability to quantify the amount of fatty infiltration, and, ultimately, it is frequently regarded as being unable to provide an accurate measurement of the liver fat content [8].

Recently, there has been notable progress in US methodologies. The overall sensitivity, specificity, positive likelihood ratio, and negative likelihood ratio of the ultrasound for the detection of a moderate-severe fatty liver, as compared to histology, were sufficiently high compared with those of other imaging techniques (i.e., CT or MRI) [1]. Thus, there has been a growing need to have a computer-aided tool to quantify

liver steatosis by using the liver echogenicity or the increased US attenuation in fatty liver tissue.

The automated fatty liver diagnosis system typically consists of the detection of the fatty liver area, feature extraction, and classification. The performance of the classifier is highly dependent on the feature set for the classifier algorithms used for the diagnosis. Some of the recent efforts in this line of research are the support vector machine (SVM) with wavelet packet transform (WPT) [9] or gray-level run length matrix (GLRLM) [10], simple neural network, and self-organizing map (SOM) with a textual feature set [11]. Other research efforts in this field include extracting the salient features with the data mining technique [12] or texture analysis [13] or finding an appropriate quantification index to decide a fatty liver class such as the fatty liver index (FLI) [14] and hepatorenal index (HRI) [15].

Further, in practice, several studies report that the ultrasonographic findings of the fatty liver are based on the brightness level of the liver in comparison to the renal parenchyma [16–18]. Since Joseph et al. [19] reported a "bright liver pattern" indicating that a closely packed high amplitude echoes throughout the liver, this pattern has been recognized as a diagnostic hallmark of the fatty liver. Normally, liver and renal cortexes are of a similar echogenicity; however, the renal cortex appears relatively hypoechoic as compared to the liver parenchyma in fatty liver patients on US. The liver-to-kidney contrast has been used as a diagnostic parameter for the fatty liver in many articles [1].

In this study, we also note the importance of the quantification of HRI as a predictor of the fatty liver level and its utility in classification. While many previous studies have viewed the fatty liver classification as a two-class problem (normal versus abnormal), our approach considers it a multiclass problem (normal, mild, moderate, and severe) on the basis of [20].

We also apply a self-organizing map (SOM) and the corresponding cluster analysis in the quantification process of the contrast of HRI with respect to the steatosis level of the liver. SOM has been effectively used in many engineering applications such as computer vision and texture analysis [21] and many areas of medical image analysis [22, 23]. The proposed method does not take into account the quality of the textual feature set that is used in the final fatty liver classification and diagnosis at this point of time. Rather, we focus on the usefulness of SOM and the other corresponding intelligent image processing methods in quantifying HRI with respect to the fatty level of a liver US image.

2. Fatty Liver Area Extraction with Image Processing Algorithms

A typical US image that contains the liver and the right kidney areas and has a relatively low intensity is shown in Figure 1.

There exists a limiting membrane with a high intensity as the border of our two regions of interest (ROI)—the liver and the right kidney. Such ROI are extracted with respect to the location of musculi abdominis and fascia found in the upper area of the liver and the fatty areas of the liver and the kidney.

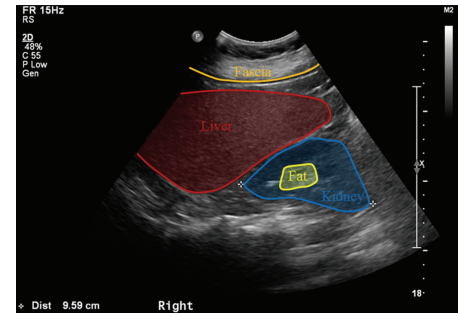

Figure 1: Ultrasonography image and regions of interest.

Figure 2 summarizes the overall procedures performed in this study. Our software consists of two major activities—ROI extraction with image processing and cluster analysis with an artificial intelligence technique. The latter will be explained in Section 3 in detail.

The first major step of image preprocessing for the US analysis is to enhance the brightness contrast. The US image contains a relatively bright area such as abdomen muscles, fascia, fat area in the kidney, and the border lines between the liver and the kidney. We apply the fuzzy stretching technique [24] for this purpose. The fuzzy stretching technique enhances the contrast by dynamically controlling the maximum and the minimum range of the stretching with a triangle-type fuzzy membership function.

Let x_i be the brightness value of the input US image where i is in the range of $[0, 255]$. Then, the average brightness value of the image x_m can be computed by using the following formula:

$$x_m = \sum_{i=0}^{255} x_i \frac{1}{MN}, \tag{1}$$

where M and N denote the width and the length of the image.

Then, the distance between the brighter area and the average $d_{\max}$, and the darker area and the average $d_{\min}$ is defined as follows:

$$\begin{aligned} d_{\max} &= \left| x_h - x_m \right|, \\ d_{\min} &= \left| x_m - x_l \right|, \end{aligned} \tag{2}$$

where x_h and x_l denote the highest and the lowest brightness pixel value, respectively. Then, the brightness values are adjusted according to the following rule and the maximum and minimum intensity values $I_{\max}$ and $I_{\min}$ are computed by the following formula:

$$\begin{aligned} &\text{if } (x_m > 128) \quad \text{ad} = 255 - x_m \\ &\text{else if } (x_m \le d_{\min}) \quad \text{ad} = d_{\min} \\ &\text{else if } (x_m \le d_{\max}) \quad \text{ad} = d_{\max} \\ &\text{else ad} = x_m, \\ &I_{\max} = x_m + \text{ad}, \quad I_{\min} = x_m - \text{ad}. \end{aligned} \tag{3}$$

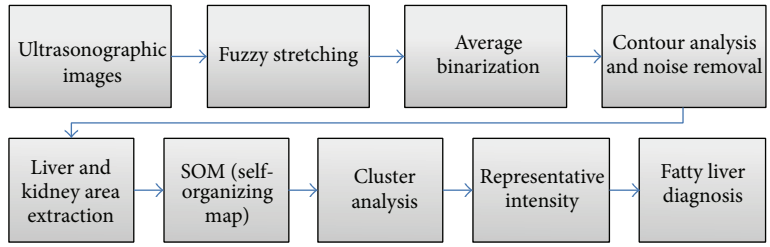

Figure 2: Overall procedure of the proposed method.

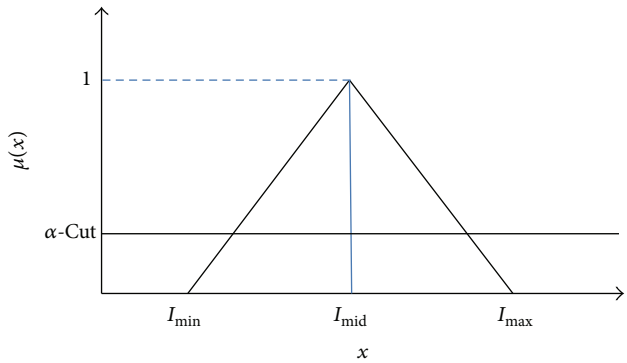

Figure 3: Fuzzy membership function for brightness enhancement.

The fuzzy membership function for intensity stretching is then defined as shown in Figure 3 in the interval $[I_{min}, I_{max}]$, where the maximum membership degree I_{mid} is defined as follows:

$$I_{mid} = \frac{I_{max} + I_{min}}{2}. \tag{4}$$

Thus, the membership degree is defined according to the following rules in the interval $[I_{min}, I_{max}]$:

$$\begin{aligned}
&\text{if } (x \le I_{min}) \quad \text{or} \quad (x \ge I_{max}) \text{ then } \mu(x) = 0,\\
&\text{if } (x > I_{mid}) \text{ then } \mu(x) = \frac{I_{max} - x}{I_{max} - I_{mid}},\\
&\text{if } (x < I_{mid}) \text{ then } \mu(x) = \frac{x - I_{min}}{I_{mid} - I_{min}},\\
&\text{if } (x = I_{mid}) \text{ then } \mu(x) = 1.
\end{aligned} \tag{5}$$

The membership degree $\mu(x)$ obtained from the above rules is then applied to the following formula to compute the lower (γ) and the higher (β) boundaries of the intensity that are defined as the minimum and maximum values among x whose $\mu(x)$ is no less than α-cut:

$$\begin{aligned}
&\text{if } (I_{min} \ne 0) \quad \alpha\text{-cut} = \frac{I_{min}}{I_{max}}\\
&\text{else } \alpha\text{-cut} = 0.5.
\end{aligned} \tag{6}$$

Finally, the following formula finishes the stretching to enhance the brightness contrast:

$$x^G = 255\frac{x - \gamma}{\beta - \gamma}, \tag{7}$$

where x^G denotes the stretched brightness value of the pixel from the original value x. Figure 4 demonstrates the effect of fuzzy stretching.

To the image obtained in Figure 4, we also apply average binarization only for pixels with positive intensity.

After binarization, we apply the edge tracking algorithm [25] for fast object labeling. The edge tracking algorithm tracks pixels having the same object label. The search for the same label is 5-directional, starting with the top left spot orthogonal to the current search direction by 45° each until the search point returns to the starting point. If the search diverges or the area obtained by this edge tracking is too small (<200) or too large (>20000), we remove those objects as noise since such a set of objects has no chance to form any fascia, fat in the kidney, or limiting membrane with a high intensity as the border of the liver and the kidney. Figure 5 demonstrates the effect of binarization (Figure 5(b)) and noise removal by object labeling (Figure 5(c)).

However, the limiting membrane, the border between the liver and the kidney, tends to have no clear form with a relatively low intensity; thus, it is easy to lose such information in the brightness-enhancing process. In order to restore such lost boundary lines, we apply the average binarization and labeling procedure again after connecting relatively bright fascia and kidney fat area. This refocusing contour analysis can successfully restore the boundary lines, and the effect can be shown as in Figure 6.

The final treatment of this ROI extraction procedure is to discriminate the liver and kidney area with reverse-binarization and AND operations. Knowing that the liver area is located in between the fascia and the limiting membrane boundary lines and the kidney area is located in between the limiting membrane boundary lines and the kidney fat area, we extracted the ROIs as shown in Figure 7 for a further analysis of hepatic steatosis.

3. Quantification of Hepatorenal Index by Self-Organizing Map

In this paper, we adopt the traditional fatty liver classification based on [20] in which abnormal fatty livers are classified

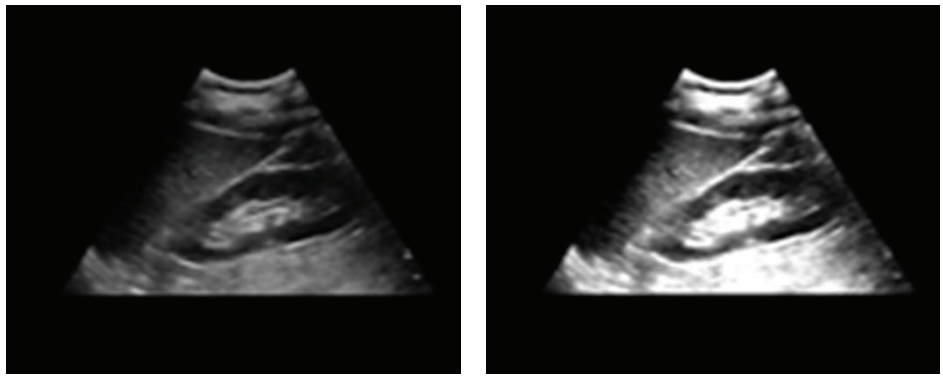

(a) Input image (b) Fuzzy stretched image

Figure 4: Fuzzy stretching effect.

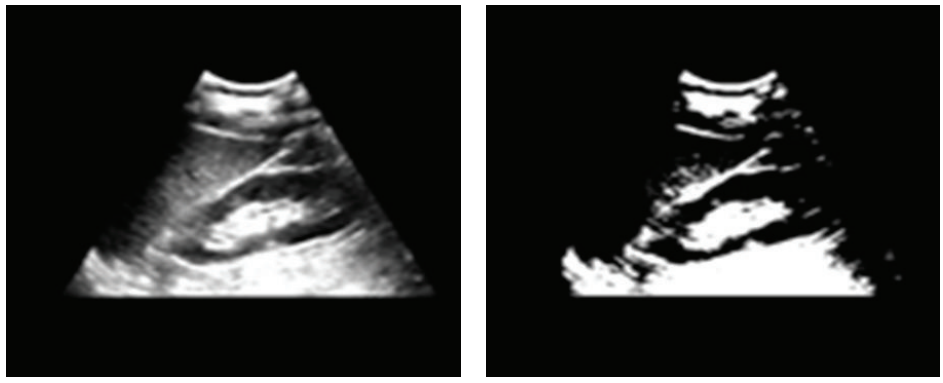

(a) Fuzzy stretched image (b) After binarization

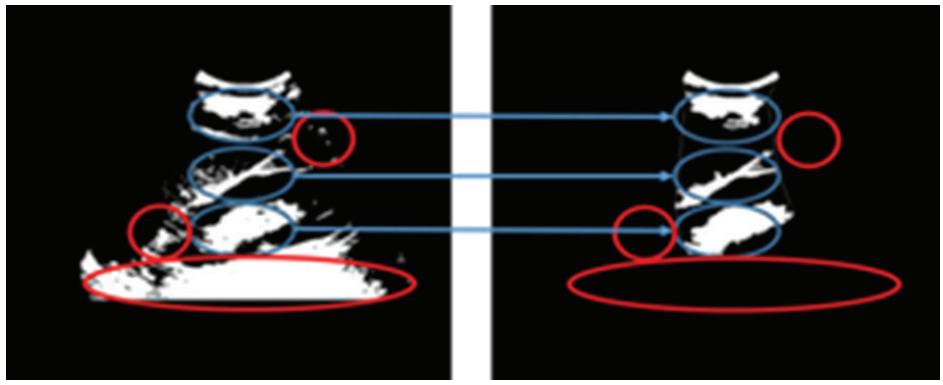

(c) After object labeling and noise removal

Figure 5: Object extraction by contour analysis.

into three levels—mild, moderate, and severe—with respect to the evidence of diffuse hyperechogenicity of the liver relative to the kidneys, ultrasound beam attenuation, and poor visualization of the intrahepatic structures. Figure 8 shows the typical mild and moderate levels of the fatty liver where the mild level (Figure 8(a)) has a slightly increasing echogenicity level of liver parenchyma with clear boundaries of the diaphragm and the intrahepatic blood vessel, whereas the moderate level (Figure 8(b)) has a relatively high increase in the echogenicity and the boundaries become vague. Such a tendency becomes stronger when the fatty liver status is "severe."

In the US analysis, the brightness level of the liver area with the presence of the right kidney, the hepatorenal index difference (HRI-diff), or hepatorenal index ratio (HRI-ratio) is often used as an index of the abnormal fatty liver classification [15–17]. However, while strongly correlated to other useful classification indexes [18], the quantification of

(a) Boundary lost (b) Boundary restored

Figure 6: Redoing binarization for boundary line restoration.

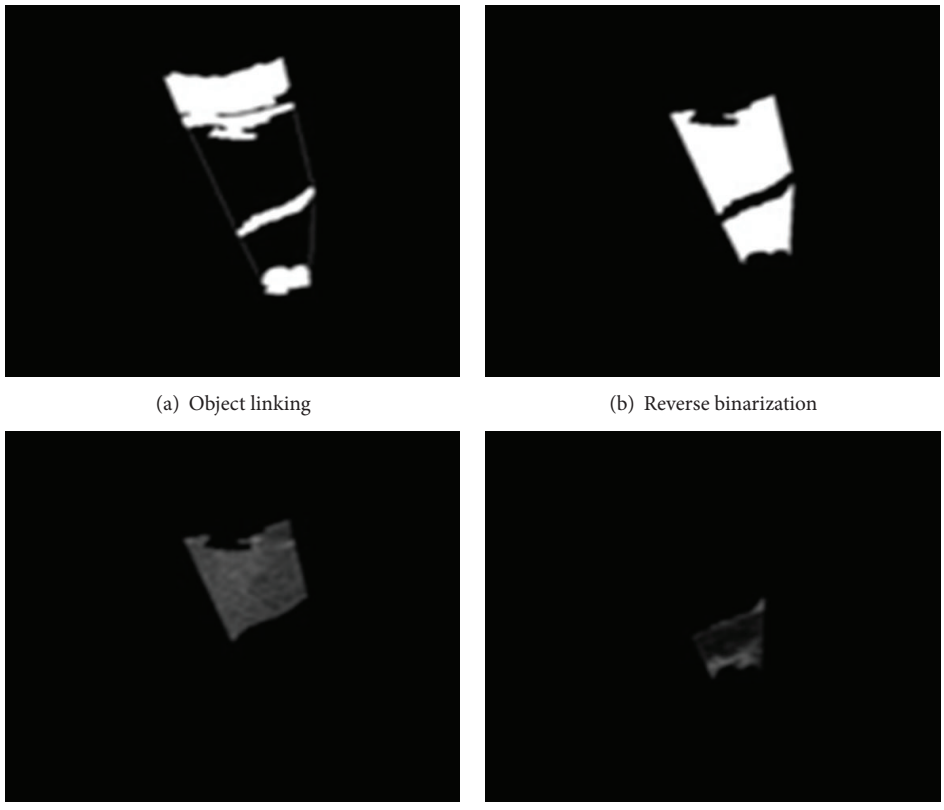

(a) Object linking (b) Reverse binarization

(c) Liver area (d) Kidney area

Figure 7: Extracting regions of interest.

HRI with respect to hepatic steatosis is not a simple problem due to the sensitivity of the probing position and the operator subjectivity.

In this paper, we propose a method based on a self-organizing map (SOM) [21] to quantify HRI-diff automatically. Our goal is to compute the representative brightness value by the cluster analysis obtained by SOM and show that such representative HRI values have a strong statistical tendency with the severity of the fatty liver level.

SOM, a nonlinear, ordered, smooth mapping of high-dimensional data onto the regular, low-dimensional array [21], is an unsupervised learning neural network tool used in many medical image analysis applications [22, 23]. Some studies have used SOM as a diagnostic classifier over a set

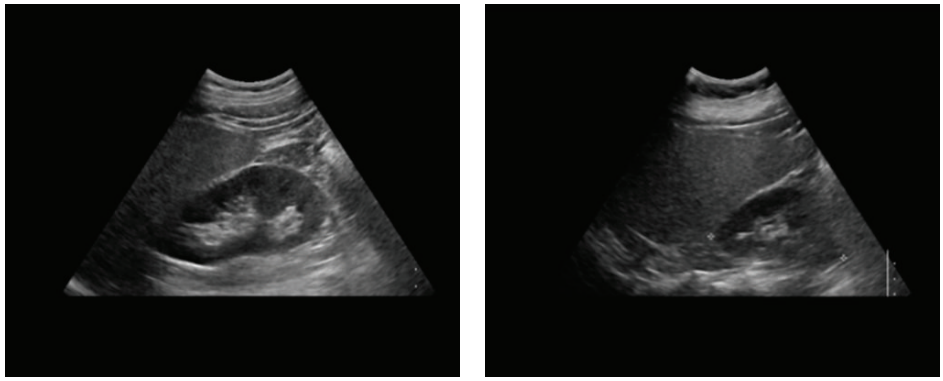

(a) Mild level (b) Moderate level

Figure 8: Fatty liver with respect to severity.

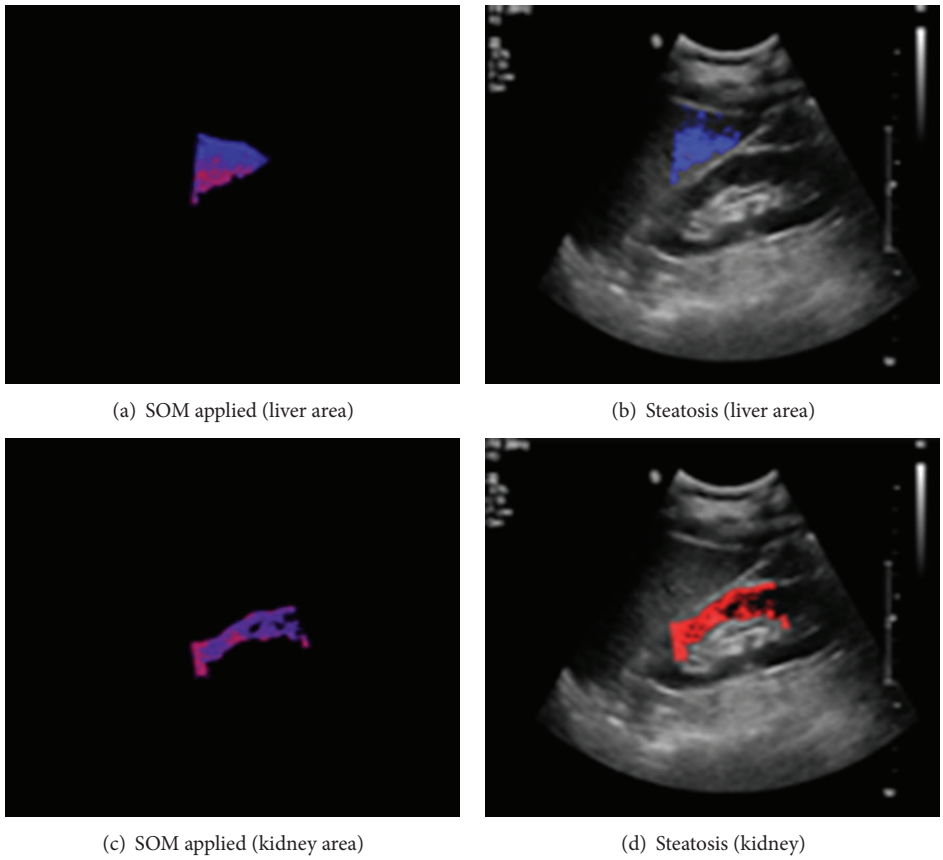

(a) SOM applied (liver area) (b) Steatosis (liver area)

(c) SOM applied (kidney area) (d) Steatosis (kidney)

Figure 9: Typical normal liver.

of textual/statistical features in this fatty liver classification problem [11], but in our work, SOM is used to form a set of stable clusters with respect to the HRI values. Then, the distinction of such clusters with respect to HRI-diff from that of renal parenchyma shows the quantified characteristic of HRI.

We use a two-dimensional output layer in this application, and the SOM algorithm used in this study is as shown in Algorithm 1.

The connection weight (w) has the role of sample input patterns and the most similar output neuron j becomes the winner during the learning process. Then, all connected weights within the radius r from the winner node j will be updated. The similarity is computed by the following:

$$D(j) = \sum_{i} \left(w_{ji} - x_i\right)^2. \tag{8}$$

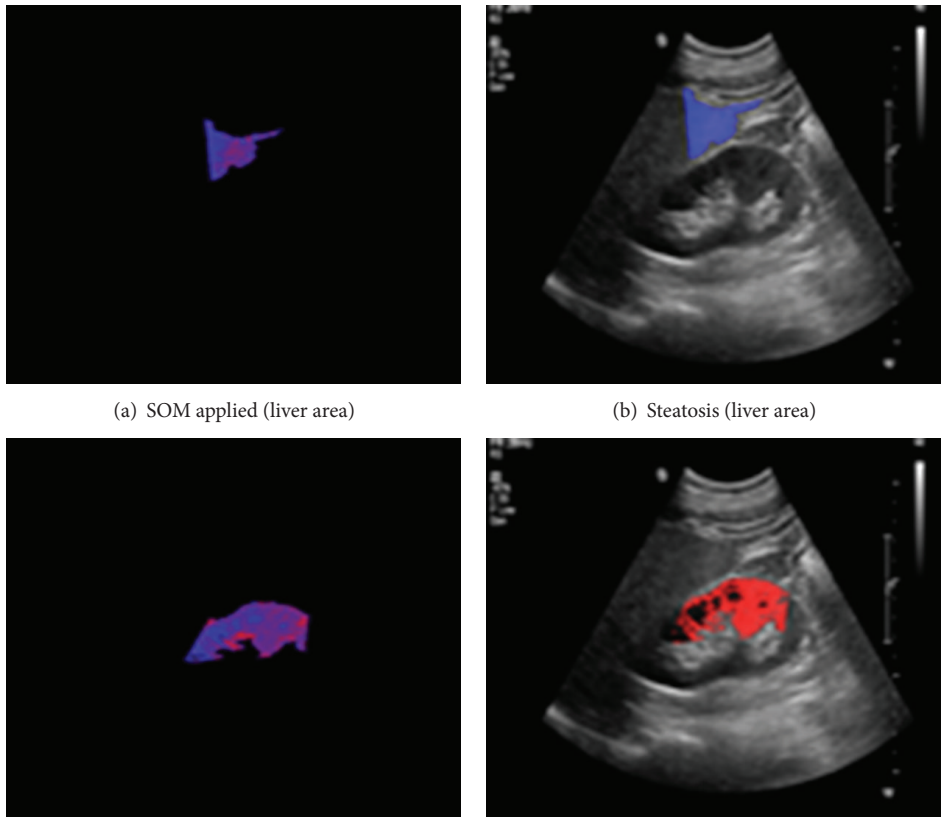

(a) SOM applied (liver area) (b) Steatosis (liver area)

(c) SOM applied (kidney area) (d) Steatosis (kidney)

Figure 10: Typical mild fatty liver.

Weight (w^{k+1}) of the learning step $k + 1$ is then defined as follows:

$$\Delta w_{ji}^{k} = \alpha \left[x_i - w_{ji}^{k} \right], \quad w_{ji}^{k+1} = w_{ji}^{k} + \alpha \left[x_i - w_{ji}^{k} \right]. \quad (9)$$

After the predefined number of repetitions, the radius r and the learning rate α are reduced and the learning step continues. The stopping condition in our experiment was $\alpha < 0.2$ or radius r becomes a nonpositive value.

The clusters from SOM learning are then analyzed after quantization. The quantization process is necessary because of the possible US distractions. Thus, the representative intensity value is defined as the average over pixels in the largest cluster after quantization.

Then, the hepatorenal index difference (HRI-diff) is computed to view if there is a statistically significant tendency with respect to the severity of hepatic steatosis.

Since it is expected that the representative intensity of the kidney area is relatively stable and that of the liver area is positively proportional to the severity of steatosis, HRI-diff will play the role of the predictor of the fatty liver severity classification.

4. Experiment and Analysis

The proposed method is implemented in Visual Studio 2010 C# with Intel Core @ 3.40 GHz and 4 GB RAM PC. 25 images from 10 normal, 7 mild, and 8 moderate fatty liver patients were obtained from the Pusan National University Hospital, Korea, in the 1024 × 768 bitmap format. Images were obtained by the right subcostal scan including the lower pole of the liver and the right kidney. Table 1 summarizes the major findings of this experiment.

Table 1: HRI quantification with respect to severity level of fatty liver.

	LP	RP	Number of CL
Normal			
Range	23–53	21–51	
SD	3.027	3.671	8–10
Mean	43.500	41.709	
Mild			
Range	38–74	28–53	
SD	2.546	3.157	9–11
Mean	52.159	43.724	
Moderate			
Range	38–91	28–68	
SD	2.321	4.023	9-10
Mean	68.729	46.704	

LP: liver parenchyma; RP: renal parenchyma; number of CL: number of clusters.

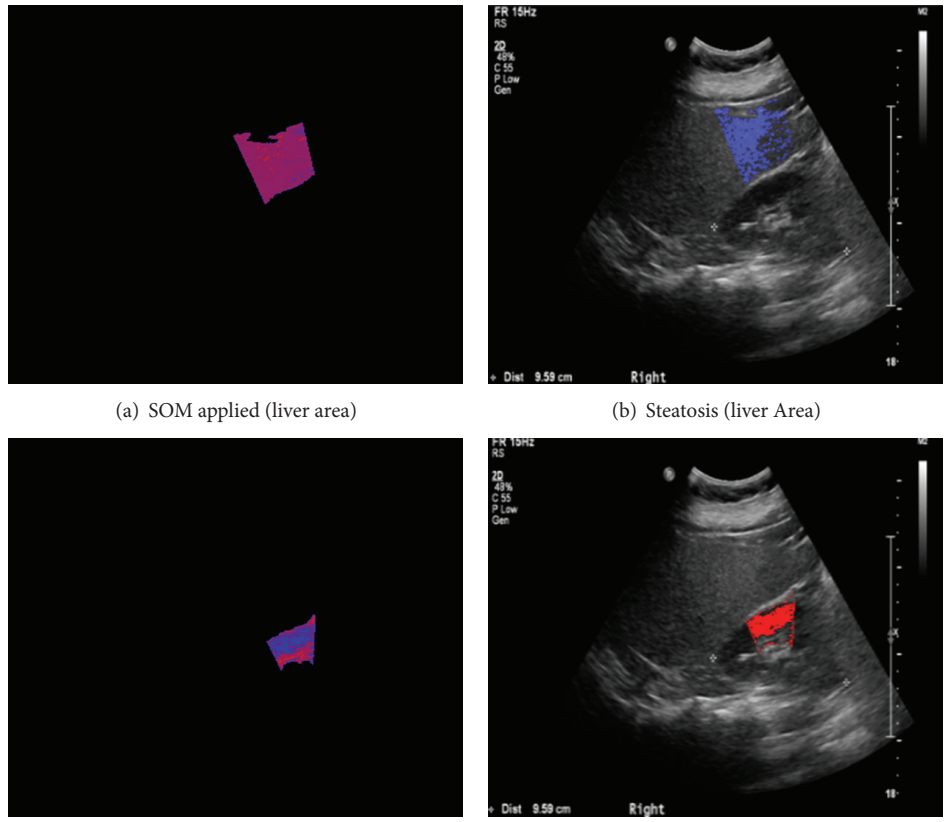

(a) SOM applied (liver area)

(b) Steatosis (liver Area)

(c) SOM applied (kidney area)

(d) Steatosis (kidney)

Figure 11: Typical moderate fatty liver.

Step 1. Initialize weights
$w \leftarrow$ random value
Step 2. Set topological neighborhood and learning rate
Radius $r \leftarrow$ integer
Learning rate $\alpha \leftarrow$ small number $(0 < \alpha < 1)$
Step 3. While the stop condition is not satisfied,
Do Steps 4–8
Step 4. For each input x
Do Steps 5–8
Step 5. Compute distance
$$D(j) = \sum_i (w_{ji} - x_i)^2$$
Step 6. Find winner neuron y_j^*
Step 7. Update weights within radius
$$w_{ji}^{k+1} = w_{ji}^k + \alpha[x_i - w_{ji}^k]$$
Step 8. Reduce the learning rate and radius
Step 9. Test the stop condition

Algorithm 1: Self-organizing map (SOM) learning algorithm.

As represented in Table 1, HRI values in the liver area are positively proportional to the severity of the hepatic steatosis and even the dispersion of the distribution is clearly discriminative considering low standard deviation within the class level.

Figures 9, 10, and 11 show the typical ROI extractions and fatty level visualizations with respect to the severity level—normal, mild, and moderate. At this point of time, we did not have "severe" fatty liver images in this experiment.

5. Conclusion

In this study, we aim to quantify the HRI difference between the liver and the kidney by using US images as a useful predictor attribute of the multilevel (multiclass) hepatic steatosis classification. The proposed fully automated computer-aided diagnostic system typically consists of three parts—ROI extraction with image processing, feature set extraction, and applying classifier algorithms. In the ROI extraction procedure, we use a fuzzy stretching algorithm to enhance the brightness contrast. The carefully designed fuzzy membership function and the corresponding auxiliary image processing techniques such as labeling, binarization, and contour analysis enable us to extract the appropriate and distinguishable liver and kidney areas from the image.

Then, the self-organizing map (SOM), an unsupervised neural network learning algorithm, is designed to form representative clusters of the liver image from the ROI US images. The characterization of the cluster analysis gives us a clear statistical delineation of the intensity distribution in terms of HRI-diff among different levels of hepatic steatosis.

The purpose of this study is to show that HRI is an important and informative diagnostic attribute in multiclass fatty liver classification because of such quantification. This encourages us to develop reliable automatic diagnostic software if it is combined with other sets of useful textual or statistical features and other powerful machine learning algorithms in the future.

Conflict of Interests

The authors declare that there is no conflict of interests regarding the publication of this paper.

Acknowledgment

This study was supported by a grant from the National R&D Program for Cancer Control, Ministry for Health and Welfare, Republic of Korea (0920050).

References

[1] R. Hernaez, M. Lazo, S. Bonekamp et al., "Diagnostic accuracy and reliability of ultrasonography for the detection of fatty liver: a meta-analysis," *Hepatology*, vol. 54, no. 3, pp. 1082–1090, 2011.

[2] R. Williams, "Global challenges in liver disease," *Hepatology*, vol. 44, no. 3, pp. 521–526, 2006.

[3] G. Targher, L. Bertolini, R. Padovani et al., "Prevalence of nonalcoholic fatty liver disease and its association with cardiovascular disease among type 2 diabetic patients," *Diabetes Care*, vol. 30, no. 5, pp. 1212–1218, 2007.

[4] D. N. Amarapurkar, E. Hashimoto, L. A. Lesmana et al., "How common is non-alcoholic fatty liver disease in the Asia–Pacific region and are there local differences?" *Journal of Gastroenterology and Hepatology*, vol. 22, no. 6, pp. 788–793, 2007.

[5] N. Chalasani, Z. Younossi, J. E. Lavine et al., "The diagnosis and management of non-alcoholic fatty liver disease: practice guideline by the American Association for the Study of Liver Diseases, American College of Gastroenterology, and the American Gastroenterological Association," *Hepatology*, vol. 55, no. 6, pp. 2005–2023, 2012.

[6] J.-F. Fu, H.-B. Shi, L.-R. Liu et al., "Non-alcoholic fatty liver disease: an early mediator predicting metabolic syndrome in obese children?" *World Journal of Gastroenterology*, vol. 17, no. 6, pp. 735–742, 2011.

[7] V. Ratziu, F. Charlotte, A. Heurtier et al., "Sampling variability of liver biopsy in nonalcoholic fatty liver disease," *Gastroenterology*, vol. 128, no. 7, pp. 1898–1906, 2005.

[8] M.-F. Xia, H.-M. Yan, W.-Y. He et al., "Standardized ultrasound hepatic/renal ratio and hepatic attenuation rate to quantify liver fat content: an improvement method," *Obesity*, vol. 20, no. 2, pp. 444–452, 2012.

[9] F. U. A. A. Minhas, D. Sabih, and M. Hussain, "Automated classification of liver disorders using ultrasound images," *Journal of Medical Systems*, vol. 36, no. 5, pp. 3163–3172, 2012.

[10] K. Raghesh Krishnan and R. Sudhakar, "Automatic classification of liver diseases from ultrasound images using GLRLM texture features," *Advances in Intelligent Systems and Computing*, vol. 195, pp. 611–624, 2013.

[11] N. Neogi, A. Adhikari, and M. Roy, "Classification of ultrasonography images of human fatty and normal livers using GLCM textural features," *Current Trends in Technology and Science*, vol. 3, no. 4, pp. 252–259, 2014.

[12] U. R. Acharya, S. V. Sree, R. Ribeiro et al., "Data mining framework for fatty liver disease classification in ultrasound: a hybrid feature extraction paradigm," *Medical Physics*, vol. 39, no. 7, pp. 4255–4264, 2012.

[13] M. Singh, S. Singh, and S. Gupta, "An information fusion based method for liver classification using texture analysis of ultrasound images," *Information Fusion*, vol. 19, no. 1, pp. 91–96, 2014.

[14] G. Bedogni, S. Bellentani, L. Miglioli et al., "The fatty liver index: a simple and accurate predictor of hepatic steatosis in the general population," *BMC Gastroenterology*, vol. 6, article 33, 2006.

[15] M. Webb, H. Yeshua, S. Zelber-Sagi et al., "Diagnostic value of a computerized hepatorenal index for sonographic quantification of liver steatosis," *American Journal of Roentgenology*, vol. 192, no. 4, pp. 909–914, 2009.

[16] G. Targher, L. Bertolini, S. Rodella, G. Lippi, G. Zoppini, and M. Chonchol, "Relationship between kidney function and liver histology in subjects with nonalcoholic steatohepatitis," *Clinical Journal of the American Society of Nephrology*, vol. 5, no. 12, pp. 2166–2171, 2010.

[17] Y. S. Park, C. H. Lee, K. M. Choi et al., "Correlation between abdominal fat amount and fatty liver using liver to kidney echo ratio on ultrasound," *Journal of Korean Society of Ultrasound in Medicine*, vol. 31, no. 4, pp. 219–224, 2012.

[18] S. İçer, A. Coşkun, and T. İkizceli, "Quantitative grading using grey relational analysis on ultrasonographic images of a fatty liver," *Journal of Medical Systems*, vol. 36, no. 4, pp. 2521–2528, 2012.

[19] A. E. A. Joseph, K. C. Dewbury, and P. G. McGuire, "Ultrasound in the detection of chronic liver disease (the "bright liver")," *British Journal of Radiology*, vol. 52, no. 615, pp. 184–188, 1979.

[20] C. A. Mittelstaedt and L. M. Vincent, *Abdominal Ultrasound*, Churchill Livingston, New York, NY, USA, 1987.

[21] J. Vesanto and E. Alhoniemi, "Clustering of the self-organizing map," *IEEE Transactions on Neural Networks*, vol. 11, no. 3, pp. 586–600, 2000.

[22] K.-B. Kim, S. Kim, and G.-H. Kim, "Vector quantizer of medical image using wavelet transform and enhanced SOM algorithm," *Neural Computing and Applications*, vol. 15, no. 3-4, pp. 245–251, 2006.

[23] P. L. Chang and W. G. Teng, "Exploiting the self-organizing map for medical image segmentation," in *Proceedings of IEEE International Symposium on Computer-Based Medical Systems*, pp. 281–288, 2007.

[24] K. B. Kim, S. W. Jang, and C. K. Kim, "Recognition of car license plate by using dynamical thresholding method and enhanced neural networks," in *Computer Analysis of Images and Patterns*, vol. 2756 of *Lecture Notes in Computer Science*, pp. 309–319, Springer, Berlin, Germany, 2003.

[25] D. B. Jess, M. Mathioudakis, R. Erdélyi, G. Verth, R. T. J. Mcateer, and F. P. Keenan, "Discovery of spatial periodicities in a coronal loop using automated edge-tracking algorithms," *The Astrophysical Journal*, vol. 680, no. 2, pp. 1523–1531, 2008.

Hindawi Publishing Corporation
BioMed Research International
Volume 2015, Article ID 343475, 8 pages
http://dx.doi.org/10.1155/2015/343475

Research Article

A Multimodal User Authentication System Using Faces and Gestures

Hyunsoek Choi[1] and Hyeyoung Park[2]

[1]*School of Electrical Engineering and Computer Science, Kyungpook National University, Deagu 702-701, Republic of Korea*
[2]*School of Computer Science and Engineering, Kyungpook National University, Deagu 702-701, Republic of Korea*

Correspondence should be addressed to Hyeyoung Park; hypark@knu.ac.kr

Received 26 September 2014; Accepted 19 November 2014

Academic Editor: Sabah Mohammed

As a novel approach to perform user authentication, we propose a multimodal biometric system that uses faces and gestures obtained from a single vision sensor. Unlike typical multimodal biometric systems using physical information, the proposed system utilizes gesture video signals combined with facial images. Whereas physical information such as face, fingerprints, and iris is fixed and not changeable, behavioral information such as gestures and signatures can be freely changed by the user, similar to a password. Therefore, it can be a countermeasure when the physical information is exposed. We aim to investigate the potential possibility of using gestures as a signal for biometric system and the robustness of the proposed multimodal user authentication system. Through computational experiments on a public database, we confirm that gesture information can help to improve the authentication performance.

1. Introduction

With the growing need for secure authentication methods, various biometric signals are being actively studied. One recent trend is the use of multimodal data for achieving high reliability [1–3]. However, in general, multimodal biometric systems require multiple sensors, which result in high developmental costs. As a new attempt for achieving high reliability and low cost, this paper proposes a novel multimodal biometric system that uses two heterogeneous biometric signals obtained from a single vision sensor: facial image and gesture video.

Face is a representative of physical biometric signals, and many studies have been carried out on developing reliable face recognition systems [4, 5]. However, the performance of face recognition systems is easily influenced by various environmental factors such as illumination, expression, pose, and occlusion. Despite a significant number of studies conducted to overcome these limitations, face recognition systems are still vulnerable and need improvement. Multimodal fusion can be a good solution to overcome this vulnerability [6–8]; however, it incurs a high cost and causes inconvenience. The proposed method is a novel approach to resolve this problem.

Gestures can also be used for user authentication. Gestures are a type of behavioral biometric signals that have recently been considered as good alternatives to physical biometric signals such as faces [9]. The biggest advantage of gestures is changeability by users. Even if physical biometric signals are stolen, users can not change their own physical signal. However, users can change the gesture signals easily like password. Along with the popularization of various IT devices such as smart phones, Kinect, and stereo cameras, a number of studies have been conducted to show that gestures can be used as a good behavioral biometric signal for user authentication. In earlier studies [10–12], it was shown that accelerometer-based gesture recognition is feasible for user authentication in mobile devices. Also, in [13] the accelerometer and the gyroscope on mobile devices were combined for gesture-based user authentication. A novel multitouch gesture-based authentication technique was also proposed [14]. The gesture signal captured by Kinect was also used for user authentication [15, 16]. However, these conventional works require specific sensors such as accelerometer, gyroscope, and depth camera.

Inspired by these previous studies, we propose to use gestures combined with face which can be obtained from

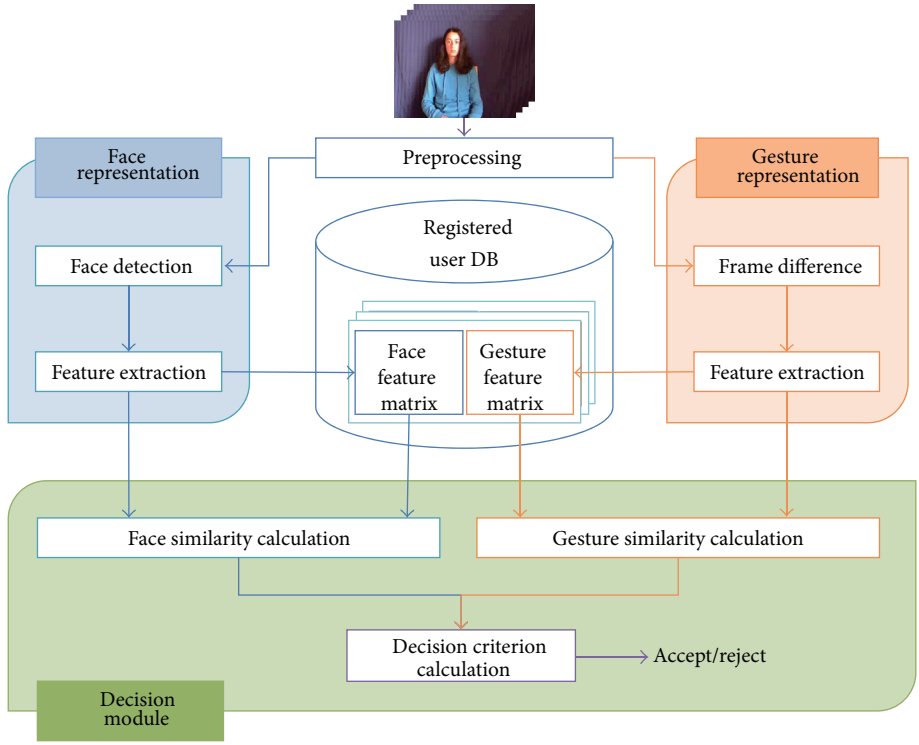

Figure 1: Overall process of the proposed multimodal biometric system, which combines face-based biometrics and gesture-based biometrics.

mboxa single vision sensor for user authentication. The proposed method can be easily implemented to many types of IT equipment including smart TVs and game devices because it uses only a general vision sensor.

One objective of the proposed method is to show the possibility of gesture video as a biometric signal for user authentication system. Another one is to show the possibility of combining two different biometric signals obtained by a single vision sensor. Although the signals are captured by the same sensor in a single action, they have virtually independent distributional properties, which is desirable for multimodal combination. Therefore, we expect to improve the performance of authentication systems using the proposed combination plan with an insignificant increase in hardware cost. In addition to the benefit of low implementation cost, we take advantage of the common properties of the two different signals. Noting that both face and gesture signals are given as RGB images, we can use common image processing techniques to extract efficient feature matrices from the two signals. Furthermore, we apply an appropriate distance measure to the feature matrices instead of typical distance measures. A comprehensive description of the proposed system and its properties are addressed in the subsequent sections.

2. Proposed Multimodal Biometric System

Figure 1 shows the overall structure of the proposed user authentication system, which is composed of three parts: face representation module, gesture representation module, and decision module. When a video stream that includes face and hand gestures is provided, simple preprocessing such as image resizing and RGB-to-gray transformation is performed. Then, the face and gesture representation modules extract facial and gesture information from the single video and represent each of them using feature matrix, respectively. The decision module uses the two feature matrices to determine whether the given input is authentic or not.

The proposed system operates in two different phases: data registration phase and authentication phase. In the data registration phase, each gallery video is represented by two feature matrices through the face and gesture representation modules, and it is added to user database in the form of two feature matrices. In the authentication phase, a given probe video initially goes through the representation modules to be represented by two feature matrices. Then, the decision module compares the probe feature matrices with the registered gallery feature matrices to determine if the given probe data is authentic or not.

Although detailed description of the representation modules and decision module is given in Sections 3 and 4, respectively, we would like to note a main characteristic of the proposed system. That is, we obtain two biometric signals from a single video stream and use a common feature extraction method for obtaining low-dimensional features from the two signals. This not only reduces the implementation cost but also makes the succeeding process simple. Because the two signals are represented by the same feature descriptor, they can be subjected to the same decision making algorithms.

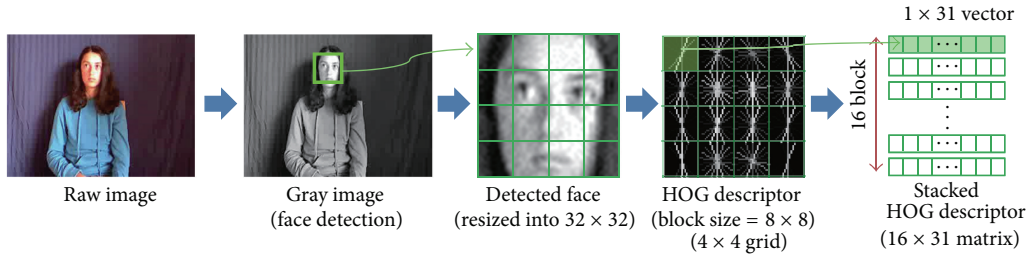

Figure 2: Process of the face representation module.

3. Data Representation Modules

3.1. Face Representation Module. The face representation module detects a face in a given input video and represents it using a feature matrix. We apply the Viola-Jones face detector [17] to locate the region of the face within an image. It searches for a face in each frame starting with the first frame of the given input video until getting detection results from the face detector.

Once a face is detected, the face area is resized to a 32×32 pixel image and we divided face image into a 4×4 grid with an 8×8 block size for local feature extraction. As a local feature descriptor, we applied a histogram of oriented gradients (HOG) descriptor [18]. We employ the VLFeat library [19] for obtaining a HOG descriptor in implementation. In the VLFeat library, each local grid is represented by 31 dimensional feature vectors so that 16×31 feature matrix $\mathbf{F}$ represents a face. Figure 2 shows the process of the face representation module.

3.2. Gesture Representation Module. In the gesture representation module, frame differencing is initially conducted between two consecutive image frames to capture the area where a gesture movement occurs. It is also possible to eliminate the undesirable effect of the illumination changes and background using frame differencing. Then, we extract the HOG descriptor from each image frame using the same algorithm used in the face representation module. Unlike the face representation module, the difference image is divided into a 6×8 grid with a 40×40 block size.

By stacking each HOG feature vector obtained from each difference image row by row, we obtain a $T \times D$ feature matrix $\mathbf{G}$ for gesture data, where T denotes the number of difference images given by a gesture sequence and D denotes the dimensionality of the feature vector obtained using the HOG descriptor. Note that T varies depending on the length of the input video whereas D is fixed (1,488 (= $6 \times 8 \times 31$) in our actual implementation). Figure 3 shows the process of the gesture representation module.

4. Decision Module and Proposed Similarity Measure

Once a video signal (probe data) is represented by a pair of two feature matrices $(\mathbf{F}_{\text{prb}}, \mathbf{G}_{\text{prb}})$, they are used as inputs with user ID and a threshold θ for the decision module. At first, the decision module finds a previously registered gallery data $(\mathbf{F}_{\text{gal}}, \mathbf{G}_{\text{gal}})$ with given user ID. Then, it calculates distance of faces and gestures, $d(\mathbf{F}_{\text{prb}}, \mathbf{F}_{\text{gal}})$ and $d(\mathbf{G}_{\text{prb}}, \mathbf{G}_{\text{gal}})$, respectively. After calculating, the decision module calculates likelihood ratio to determine whether to accept or reject by decision criterion with a threshold θ. To achieve a good authentication performance, we focus on two core factors of the decision module: the distance measure and decision criterion.

Note that columns and rows in the face feature matrix $\mathbf{F}$ and gesture feature matrix $\mathbf{G}$ have special characteristics. For face feature matrix $\mathbf{F}$, each row vector corresponds to local grid in facial image and each column corresponds to a histogram quantity of HOG feature descriptor (see Figure 2). For gesture feature matrix $\mathbf{G}$, each row vector corresponds to a frame in gesture video and each column corresponds to a histogram quantity of HOG feature descriptor (see Figure 3). Therefore, typical distance measures for vector data may cause some loss in the relation of time and spatial locality information. We try to maintain the spatial locality of facial image and the sequential relationship between the image frames of the gesture video by using the matrix features directly without vectorization. For this purpose, we employ the matrix correlation distance proposed in our previous works [20] which is a distance measure for matrix data. When two $l_1 \times l_2$ feature matrices $\mathbf{X}$ and $\mathbf{Y}$ are given, the matrix correlation distance is defined as

$$d(\mathbf{X}, \mathbf{Y}) = 1 - \left(\frac{\rho_{\text{row}}(\mathbf{X}, \mathbf{Y}) + \rho_{\text{col}}(\mathbf{X}, \mathbf{Y})}{2} \right),$$

$$\rho_{\text{row}}(\mathbf{X}, \mathbf{Y}) = \frac{1}{l_1} \sum_{i=1}^{l_1} \frac{\sum_{j=1}^{l_2} (x_{ij} - m_x)(y_{ij} - m_y)}{\sqrt{\sum_{j=1}^{l_2} (x_{ij} - m_x)^2 \sum_{j=1}^{l_2} (y_{ij} - m_y)^2}}, \quad (1)$$

$$\rho_{\text{col}}(\mathbf{X}, \mathbf{Y}) = \frac{1}{l_2} \sum_{j=1}^{l_2} \frac{\sum_{i=1}^{l_1} (x_{ij} - m_x)(y_{ij} - m_y)}{\sqrt{\sum_{i=1}^{l_1} (x_{ij} - m_x)^2 \sum_{i=1}^{l_1} (y_{ij} - m_y)^2}},$$

where m_x and m_y are the average of all the elements in $\mathbf{X}$ and $\mathbf{Y}$, respectively. The distance value $d(\mathbf{X}, \mathbf{Y})$ is in $[0, 2]$, which is similar to the conventional correlation distance. We should note that the distance measure assumes that two matrices $\mathbf{X}$ and $\mathbf{Y}$ have the same size. Therefore, in the case of gesture data with various row sizes depending on the length of the video, an additional process is required to perform size alignment

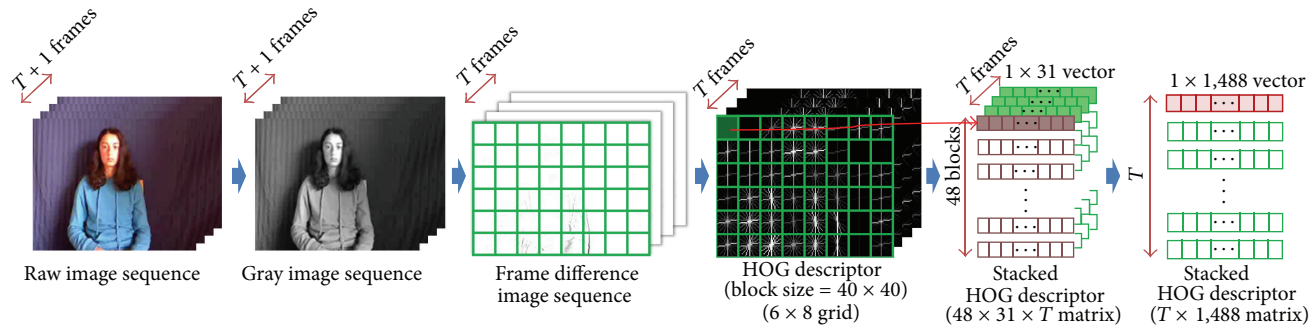

FIGURE 3: Process of the gesture representation module.

of two gesture feature matrices. In this paper, we apply a dynamic time warping (DTW) algorithm [21] to align the rows of matrices, which is a technique to find an optimal alignment between two given sequences.

After computing the distance values $d_F = d(\mathbf{F}_{\text{prb}}, \mathbf{F}_{\text{gal}})$ and $d_G = d(\mathbf{G}_{\text{prb}}, \mathbf{G}_{\text{gal}})$, we need to make a decision of acceptance using these values. To do this, we propose a decision criterion based on the likelihood ratio of the distance values, which is defined by

$$r_{FG}(d_F, d_G) = \frac{p(\Omega_A \mid d_F, d_G)}{p(\Omega_I \mid d_F, d_G)} = \frac{p(d_F, d_G \mid \Omega_A)\, p(\Omega_A)}{p(d_F, d_G \mid \Omega_I)\, p(\Omega_I)}, \tag{2}$$

where Ω_A denotes the class of distance values from authentic data pairs and Ω_I denotes the class of distance values from impostor data pairs. Therefore, r_{FG} indicates the ratio of likelihood of whether the distance values (d_F, d_G) originate from an authentic data pair or an impostor data pair. In other words, a large value of r_{FG} implies that the observed distance (d_F, d_G) has a higher possibility of originating from the population of authentic data pairs.

In order to obtain an explicit function for calculating r_{FG}, we need to estimate the probability densities $p(\Omega_A \mid d_F, d_G)$ and $p(\Omega_I \mid d_F, d_G)$. For real world implementation, we assume the Gaussian model for $p(d_F, d_G \mid \Omega_A)$ and $p(d_F, d_G \mid \Omega_I)$ and estimate the parameters using gallery data. Similarly the prior probabilities $p(\Omega_A)$ and $p(\Omega_I)$ are estimated, too. Though the threshold θ is set for 1 typically, it is changeable. If θ is high, the number of false acceptances is decreased and the number of false rejections is increased. If θ is low, the reverse phenomenon occurs. In the experiments, we measure the performance of proposed authentication system with variable θ. A summarized description of decision module is presented in Algorithm 1.

5. Experimental Results

In order to confirm the performance of proposed system, we conducted experiments on the ChaLearn database [22], which was built for a gesture recognition competition. Although the data includes depth signals obtained from Kinect, we use only RGB signals because the proposed method is developed for a general vision sensor. Figure 4 shows some examples of the data. From the whole data set, we prepared three sets—A, B, and C—for experiments. Each set is composed of 80 video samples from 20 subjects; each subject makes his/her own unique gesture four times. Experiments are carried out for each set separately using 4-fold cross-validation. Three samples from each subject are used for gallery data and one sample is used for probe data. Therefore, total 12 experiments were carried out.

Before starting authentication, we first need to estimate two conditional distributions, $p(d_F, d_G \mid \Omega_A)$ and $p(d_F, d_G \mid \Omega_I)$, which are used in decision criterion $r_{FG}(d_F, d_G)$. For each experiment, we first make all possible data pairs from gallery data and in order to obtain 1,770 distance values, among which 60 values are from authentic pairs and 1,710 from impostor pairs. The estimated pdf $p(d_F, d_G \mid \Omega_A)$ and $p(d_F, d_G \mid \Omega_I)$ using these values are then applied to calculate $r_{FG}(d_F, d_G)$ in the authentication phase. For evaluating authentication performance, we compute distances between gallery and probe data. Since we have 20 probe samples and 60 gallery samples, there are 1,200 distance values: 60 authentic values and 1,140 impostor values. The performance is evaluated by the error rates (false acceptance and false rejection) of decision module for the 1,200 values.

We compared the performance of the decision module by changing modality and other conventional distance measures. In the unimodal case, we use marginal distribution such as $p(d_F \mid \Omega_A)$ and $p(d_G \mid \Omega_A)$ for obtaining the decision criterion. We first compared the value of equal error rate (EER), which is a typical measure for evaluating authentication systems. EER is the value of error rate when the false acceptance rate (FAR) is equal to the false rejection rate (FRR). Figure 5 shows the average EER over 4-fold cross-validation for each set A, B, and C. As can be seen from Figure 5, gesture-based unimodal system shows slightly better performance than face-based unimodal system. Also, the proposed multimodal biometric system shows the best result.

In Figure 6, we present the detection error tradeoff (DET) curves [23] for visualized comparison among different modalities with various distance measures. The DET curve is a plot of error rates for binary classification systems, in which the lower left curve implies the better performance.

Input: Feature matrices of face $\mathbf{F}_{prb}$ and gesture $\mathbf{G}_{prb}$ for a probe video with user ID and a threshold θ
Output: Authentication Result (Accept/Reject)
(1) Find a gallery data $(\mathbf{F}_{gal}, \mathbf{G}_{gal})$ with user ID
(2) Calculate the distance $d_F = d(\mathbf{F}_{prb}, \mathbf{F}_{gal})$ using (1)
(3) Align the gesture feature matrix $\mathbf{G}_{prb}$ and $\mathbf{G}_{gal}$ using DTW algorithm
$(\mathbf{G}_{prb}, \mathbf{G}_{gal}) \xrightarrow{\text{DTW}} (\widetilde{\mathbf{G}}_{prb}, \widetilde{\mathbf{G}}_{gal})$
$\widetilde{\mathbf{G}}_{prb}$ and $\widetilde{\mathbf{G}}_{gal}$ have same size.
(4) Calculate the distance $d_G = d(\widetilde{\mathbf{G}}_{prb}, \widetilde{\mathbf{G}}_{gal})$ using (1)
(5) Calculate the likelihood ratio, $r_{FG}(d_F, d_G)$ using (2)
(6) **if** $r_{FG}(d_F, d_G) > \theta$ **then**
(7) Probe video is accepted
(8) **else**
(9) Probe video is rejected
(10) **end if**

Algorithm 1: Pseudocode for the decision module.

(a) (b)

Figure 4: Sample images from ChaLearn database: (a) first frames of 20 selected users, (b) image frames in a gesture video.

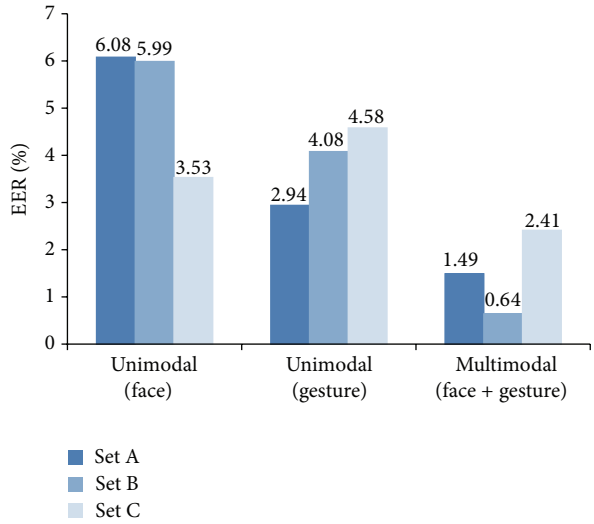

Figure 5: Average EER (%) depending on biosignals using matrix correlation distance.

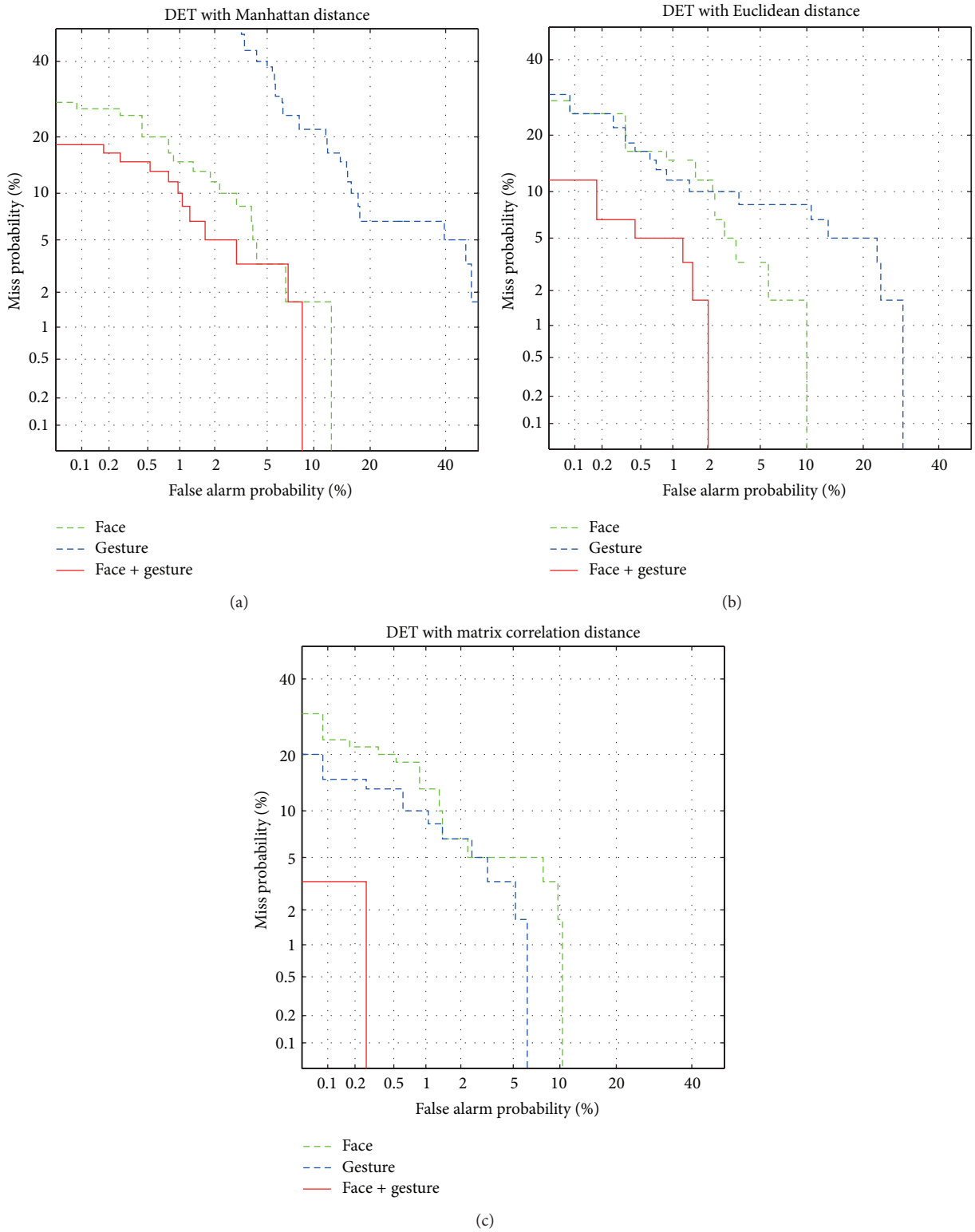

Figure 6: DET curves of authentication system with different modalities: (a) Manhattan distance, (b) Euclidean distance, and (c) matrix correlation distance.

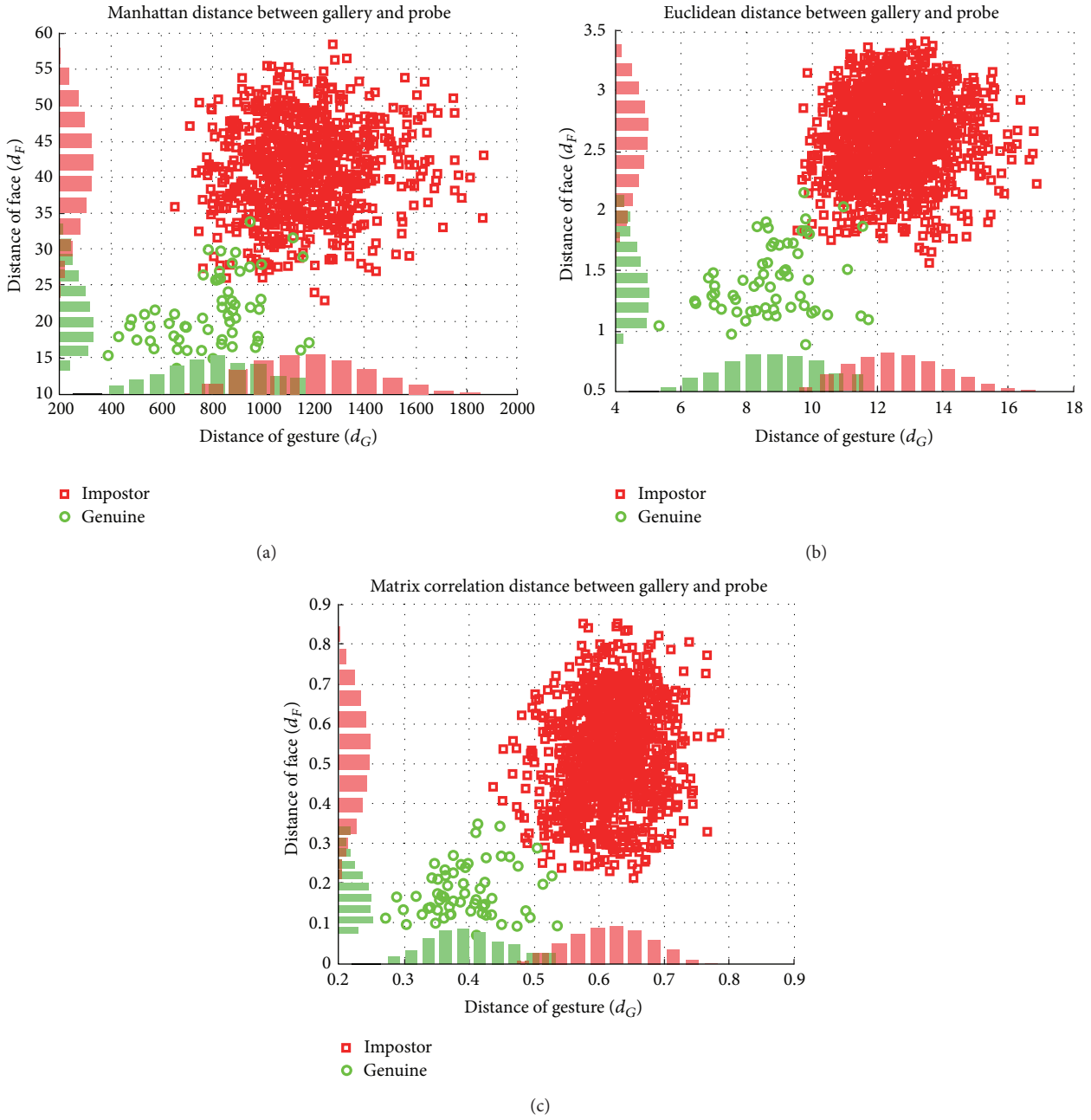

FIGURE 7: Scatter plots of distance values between authentic pairs (○) as well as impostor pairs (□): (a) Manhattan distance, (b) Euclidean distance, and (c) matrix correlation distance.

As can be seen from Figure 6, the proposed multimodal biometric system is superior to unimodal systems regardless of the distance measures. We can also observe that the performance is dependent on the distance measures. For gesture, conventional Manhattan distance and Euclidean distance give poor performance but the matrix correlation distance shows improvement, which is even better than face. This effect is emphasized by the combination of face and gesture, resulting in the remarkable improvement of DET curves as shown in the solid curve of Figure 6(c).

Figure 7 shows the scatter plots of the distance values (d_F, d_G) in Ω_A (○) as well as those in Ω_I (□). In this figure, we can observe that the discriminability is increased by using multimodality. We also plot the marginal histogram of d_F and d_G on the corresponding axes. The overlapped region of histogram implies the region where decision error occurs. In the case of a gesture, we can see that the matrix correlation distance can significantly decrease overlapped region. This means that matrix correlation distance is more appropriate to gesture data with our proposed feature representation. Additionally, we can observe that the bivariate distributions of (d_F, d_G) have the shape of ellipse, which can justify our Gaussian assumption for estimating the conditional distributions $p(d_F, d_G \mid \Omega_I)$ and $p(d_F, d_G \mid \Omega_A)$. Moreover, from

the shape of ellipse, we can guess that the two modalities are almost independent, and this is supported by the fact that the average value of correlation coefficient is 0.19. This property is desirable for combining two biometric signals to construct multimodal biometric system.

6. Conclusion

In this paper, we present a look into simple and efficient vision-based multimodal biometric system using heterogeneous biometric signals. By combining physical and behavioral biometric signals, we can achieve a high degree of reliability. Because the proposed system uses a single vision sensor, it can be easily implemented on commonly used smart devices such as smart TVs. More comprehensive study on developing efficient feature extraction and classification will be done for real world application of the proposal system.

Conflict of Interests

The authors declare that there is no conflict of interests regarding the publication of this paper.

Acknowledgments

This research was partially supported by the DGIST R&D Program of the Ministry of Education, Science and Technology of Korea (13-IT-03) and Basic Science Research Program through the National Research Foundation of Korea (NRF) funded by the Ministry of Education, Science and Technology (NRF-2013R1A1A2061831).

References

[1] A. Ross and A. K. Jain, "Multimodal biometrics: an overview," in *Proceedings of the 12th European Signal Processing Conference*, pp. 1221–1224, Vienna, Austria, September 2004.

[2] K. Bowyer, K. Chang, and P. Yan, "Multi-modal biometrics: an overview," in *Proceedings of the 2nd Workshop on Multi-Modal User Authentication*, Toulouse, France, May 2006.

[3] A. K. Jain and A. Kumar, "Biometric recognition: an overview," in *Second Generation Biometrics: The Ethical, Legal and Social Context*, E. Mordini and D. Tzovaras, Eds., pp. 49–79, Springer, Amsterdam, The Netherlands, 2012.

[4] W. Zhao, R. Chellappa, P. J. Phillips, and A. Rosenfeld, "Face recognition: a literature survey," *ACM Computing Surveys*, vol. 35, no. 4, pp. 399–458, 2003.

[5] R. Jafri and H. R. Arabnia, "A survey of face recognition techniques," *Journal of Information Processing Systems*, vol. 5, no. 2, pp. 41–68, 2009.

[6] I. A. Kakadiaris, G. Passalis, T. Theoharis, G. Toderici, I. Konstantinidis, and N. Murtuza, "Multimodal face recognition: combination of geometry with physiological information," in *Proceedings of the IEEE Computer Society Conference on Computer Vision and Pattern Recognition (CVPR '05)*, vol. 2, pp. 1022–1029, San Diego, Calif, USA, June 2005.

[7] K. W. Bowyer, K. Chang, and P. Flynn, "A survey of approaches and challenges in 3D and multi-modal 3D + 2D face recognition," *Computer Vision and Image Understanding*, vol. 101, no. 1, pp. 1–15, 2006.

[8] K. I. Chang, K. W. Bowyer, and P. J. Flynn, "An evaluation of multimodal 2D+3D face biometrics," *IEEE Transactions on Pattern Analysis and Machine Intelligence*, vol. 27, no. 4, pp. 619–624, 2005.

[9] R. V. Yampolskiy and V. Govindaraju, "Behavioural biometrics: a survey and classification," *International Journal of Biometrics*, vol. 1, no. 1, pp. 81–113, 2008.

[10] J. Liu, Z. Wang, L. Zhong, J. Wickramasuriya, and V. Vasudevan, "uWave: accelerometer-based personalized gesture recognition and its applications," in *Proceedings of the 7th Annual IEEE International Conference on Pervasive Computing and Communications (PerCom '09)*, pp. 1–9, Galveston, Tex, USA, March 2009.

[11] G. Bailador, C. Sanchez-Avila, J. Guerra-Casanova, and A. de Santos Sierra, "Analysis of pattern recognition techniques for in-air signature biometrics," *Pattern Recognition*, vol. 44, no. 10-11, pp. 2468–2478, 2011.

[12] J. Guerra-Casanova, C. Sánchez-Ávila, G. Bailador, and A. de Santos Sierra, "Authentication in mobile devices through hand gesture recognition," *International Journal of Information Security*, vol. 11, no. 2, pp. 65–83, 2012.

[13] D. Guse, *Gesture-based user authentication on mobile devices using accelerometer and gyroscope [Master thesis]*, Berlin Institue of Technology, 2011.

[14] N. Sae-Bae, K. Ahmed, K. Isbister, and N. Memon, "Biometric-rich gestures: a novel approach to authentication on multi-touch devices," in *Proceedings of the 30th ACM Conference on Human Factors in Computing Systems (CHI '12)*, pp. 977–986, Austin, Tex, USA, May 2012.

[15] K. Lai, J. Konrad, and P. Ishwar, "Towards gesture-based user authentication," in *Proceedings of the IEEE 9th International Conference on Advanced Video and Signal-Based Surveillance (AVSS '12)*, pp. 282–287, Beijing, China, September 2012.

[16] J. Wu, J. Konrad, and P. Ishwar, "The value of multiple viewpoints in gesture-based user authentication," in *Proceedings of the IEEE Computer Society Conference on Computer Vision and Pattern Recognition Workshop*, pp. 90–97, Columbus, Ohio, USA, June 2014.

[17] P. Viola and M. J. Jones, "Robust real-time face detection," *International Journal of Computer Vision*, vol. 57, no. 2, pp. 137–154, 2004.

[18] N. Dalal and B. Triggs, "Histograms of oriented gradients for human detection," in *Proceedings of the IEEE Computer Society Conference on Computer Vision and Pattern Recognition (CVPR '05)*, pp. 886–893, San Diego, Calif, USA, June 2005.

[19] A. Vedaldi and B. Fulkerson, "VLFeat: An Open and Portable Library of Computer Vision Algorithms," http://www.vlfeat.org.

[20] H. Choi, J. Seo, and H. Park, "Matrix correlation distance for 2D image classification," in *Proceedings of the of ACM Symposium on Applied Computing*, pp. 1741–1742, Gyeongju, Republic of Korea, March 2014.

[21] M. Müller, "Dynamic time warping," in *Information Retrieval for Music and Motion*, M. Müller, Ed., pp. 69–84, Springer, New York, NY, USA, 2007.

[22] ChaLearn, *ChaLearn Gesture Dataset (CGD 2011)*, 2012, http://gesture.chalearn.org/data.

[23] A. Martin, G. Doddington, and T. Kamm, "The DET curve in assessment of detection task performance," in *Proceedings of the European Conference on Speech Communication and Technology*, pp. 1895–1898, Rhodes, Greece, September 1997.

Hindawi Publishing Corporation
BioMed Research International
Volume 2014, Article ID 872827, 8 pages
http://dx.doi.org/10.1155/2014/872827

Research Article

Establishing Standards for Studying Renal Function in Mice through Measurements of Body Size-Adjusted Creatinine and Urea Levels

Wellington Francisco Rodrigues,[1,2] Camila Botelho Miguel,[1] Marcelo Henrique Napimoga,[3] Carlo Jose Freire Oliveira,[4] and Javier Emilio Lazo-Chica[1,4]

[1] *Postgraduate Course in Health Sciences, Federal University of Triângulo Mineiro, 38061-500 Uberaba, MG, Brazil*
[2] *Cefores, Federal University of Triangulo Mineiro, 38015-050 Uberaba, MG, Brazil*
[3] *Laboratory of Immunology and Molecular Biology, São Leopoldo Mandic Institute and Research Center, 13045-755 Campinas, SP, Brazil*
[4] *Institute of Biological and Natural Sciences, Federal University of Triângulo Mineiro, 38015-050 Uberaba, MG, Brazil*

Correspondence should be addressed to Carlo Jose Freire Oliveira; carlo@icbn.uftm.edu.br

Received 3 June 2014; Accepted 23 July 2014; Published 27 August 2014

Academic Editor: Tai hoon Kim

Strategies for obtaining reliable results are increasingly implemented in order to reduce errors in the analysis of human and veterinary samples; however, further data are required for murine samples. Here, we determined an average factor from the murine body surface area for the calculation of biochemical renal parameters, assessed the effects of storage and freeze-thawing of C57BL/6 mouse samples on plasmatic and urinary urea, and evaluated the effects of using two different urea-measurement techniques. After obtaining 24 h urine samples, blood was collected, and body weight and length were established. The samples were evaluated after collection or stored at −20°C and −70°C. At different time points (0, 4, and 90 days), these samples were thawed, the creatinine and/or urea concentrations were analyzed, and samples were restored at these temperatures for further measurements. We show that creatinine clearance measurements should be adjusted according to the body surface area, which was calculated based on the weight and length of the animal. Repeated freeze-thawing cycles negatively affected the urea concentration; the urea concentration was more reproducible when using the modified Berthelot reaction rather than the ultraviolet method. Our findings will facilitate standardization and optimization of methodology as well as understanding of renal and other biochemical data obtained from mice.

1. Introduction

The kidneys have homeostatic, regulatory, and excretory roles and, depending on their ability to function, they can exhibit a variety of pathological conditions. However, more than a century after the first development of an assay for evaluating kidney function [1], some doubts persist about the correct method for evaluation of the function of this organ.

Among the current tools used to evaluate renal function, biochemical measurements are the most commonly used and include evaluation of creatinine clearance, by analyzing the serum, plasma, and urine creatinine levels and of urea concentration, by assessing the plasma concentration and excretion of urea [2]. The main techniques used to evaluate serum, plasma, and urine creatinine levels are the colorimetric assay, employing alkaline picrate [1], and enzymatic assays [3], while high-performance liquid chromatography (HPLC) is also used to a lesser extent [4, 5]. To assess urea concentration, colorimetric and enzymatic assays are also used; the vast majority of these employ an enzyme that breaks down urea (urease) as well as a coupled enzyme that uses ammonia as substrate.

The methods currently used for evaluating creatinine clearance have been compared in a study investigating the sera of different animal species; these methods vary significantly in their measurement of creatinine clearance in serum

and overestimate or underestimate the actual glomerular filtration rate, which is represented by the clearance [6]. Besides these analytical variations, another important factor influencing measurement of creatinine clearance is the ratio of weight to height, which determines body surface area (BSA); creatinine clearance is typically corrected for the latter. Although the methodological parameters of height and weight for determining BSA have been determined in humans, these values cannot be applied for assessment of creatinine clearance in experimental animal models, such as mice.

With regard to laboratory methods for measurement of urea, the techniques commonly used do not suffer from analytical variation; however, these techniques are often used to assess samples collected at various temperatures and stored for different periods of time [7, 8], and, as already shown for canine and equine species, these variations in time and temperature may lead to different estimations of urea concentrations. Furthermore, although there are no significant discrepancies between the techniques, the variation of standard deviation in duplicate or triplicate in acquiring the mean values should be considered.

Thus, given that there may be variations in both the laboratory techniques and the methods used for determining creatinine clearance and urea concentration, the objective of this study was to determine an average factor from the murine BSA for the calculation of biochemical renal parameters, to determine the effects of storage and freeze-thawing of mice serum on plasmatic and urinary urea measurements and to evaluate the effects of using two different urea-measurement techniques that are in common laboratory use.

2. Methods

2.1. Animals. All experiments were conducted in accordance with the National Health guidelines for the welfare of experimental animals and with the approval of the Ethical Committee of the University Federal of Triângulo Mineiro (# 150/2010). Adult male C57BL/6 mice ($n = 40$) weighing 19–25 g, and aged 8–12 weeks, were housed in temperature-controlled rooms (22–25°C), with access to water and food ad libitum.

2.2. Biological Samples. After obtaining 24 h urine samples from the mice in a metabolic cage, the animals were fasted for 4 h; after this procedure the animals were heparinized (40 units of Hemofol, 5000 IU/mL) and euthanized in a CO_2 chamber. Then, blood was removed through the ophthalmic plexus with the aid of a glass Pasteur pipette. The blood was subjected to centrifugation at 1831 ×g for 10 min to obtain plasma.

2.3. Quality Control. We implemented internal quality control processes, where a clear definition of objectives, procedures, standards, and criteria for the tolerance limits, corrective actions, and registration of the activities, as well as the use of controls to evaluate the imprecision of the analysis, were stated and monitored. Control charts, that is, those of Levey-Jennings and the multiple Rules of Westgard were also implemented [9, 10].

2.4. Ratio of Weight and Height for Determining BSA. For the standardization of BSA, we used the following equation: BSA = weight $(W)^{0.425} \times$ length $(L)^{0.725} \times 0.007184$ [11].

2.5. Creatinine Clearance. The amount of creatinine in plasma and 24 h urine was determined in nine animals using a commercial kit (Biotechnical; Varginha, Minas Gerais, Brazil) based on a kinetic (two-point) colorimetric method (red-yellow) that employs picrate in an alkaline solution. Absorbance measurements were performed using a semiautomated method, using a spectrophotometer (Bioplus-2000 Barueri, São Paulo, Brazil) at a wavelength of 500 nm and a water bath at 37°C (Sieger-Stern 6, Campo Mourão, Paraná, Brazil), without diluting or concentrating the samples. Creatinine clearance was expressed in mL/min, obtained by the following equation:

$$\text{Clearance}\left(\text{mL/min/XmBSm}^2\right) = \frac{\left(D\ [\text{mL/min}] \times \text{XmBS}^2\right)}{\text{BS}}, \quad (1)$$

where D = depuration, which is equal to the concentration of urine creatinine (mg/dL)/concentration of plasma creatinine (mg/dL) × urinary volume in 24 h (mL), and $\text{XmBSm}^2 = \sum n\text{BS}/n$, where n = number of animals, and BS = body surface area.

2.6. Variables for Determination of Analytical Variations in the Concentration of Urea. To evaluate analytical changes in the quantification of urea, we performed three experiments.

(1) Plasma samples from two separate sets of experiments ($n = 10$ animals) were subjected to freezing (on the day of collection and on the 4th day after collection) and thawing (on the 4th and 90th days after collection); thereafter, the urea concentration was measured, without varying the temperature.

(2) Plasma and urine ($n = 10$ animals) were collected and immediately separated into 12 different aliquots to allow quantifying urea concentration after different periods of storage (0, 4, and 90 days) and different storage temperatures (room temperature, −20°C and −70°C).

(3) The concentration of urea from urine samples was determined using two different methods (enzymatic colorimetric and ultraviolet), without storage period or temperature variations.

2.7. Urea. Plasma and urinary urea were quantified using commercial kits (urea ultraviolet and the modified Berthelot reaction; Biotechnical, Varginha, Minas Gerais, Brazil). The absorbance readings were obtained using a semiautomated method, employing a spectrophotometer (Bioplus-2000 Barueri, São Paulo, Brazil) at wavelengths of 340 and

Table 1: Values for the calculation of body surface area ($n = 40$).

	W (kg)	L (cm)	$W^{0.425}$	$L^{0.007184}$	BSA
XM	0.021	7.79	0.20	4.43	0.006178561
Std. error	0.00026	0.056	0.00103	0.023	0.0000537
CV (%)	7.98	4.57	3.36	3.32	5.43

W: weight; L: length; BSA: body surface area; XM: mean; Std. error: standard error; CV: coefficient of variation.

Table 2: Data for the quantification of creatinine clearance ($n = 9$).

	PCr mg/dL	Ucr mg per 24 h	Uv mL/min	Ecc mL/min	CrCl*0.006179 mL/min
	$6.15E-01$	$4.71E-01$	$3.48E-03$	$5.32E-02$	$4.61E-02$
	$5.13E-01$	$3.69E-01$	$3.32E-03$	$5.00E-02$	$5.27E-02$
	$3.08E-01$	$2.22E-01$	$4.87E-03$	$5.01E-02$	$4.99E-02$
	$5.64E-01$	$8.25E-01$	$5.55E-03$	$1.02E-01$	$9.81E-02$
	$4.10E-01$	$4.43E-01$	$4.08E-03$	$7.50E-02$	$7.44E-02$
	$5.64E-01$	$5.32E-01$	$3.20E-03$	$6.55E-02$	$6.19E-02$
	$9.74E-01$	$2.67E-01$	$1.19E-03$	$1.90E-02$	$2.01E-02$
	$3.08E-01$	$1.62E-01$	$3.12E-04$	$3.66E-02$	$3.71E-02$
	$4.62E-01$	$3.10E-01$	$9.72E-04$	$4.66E-02$	$4.66E-02$
Median	$5.13E-01$	$3.69E-01$	$3.32E-03$	$5.01E-02$	$4.99E-02$
Maximum	$9.74E-01$	$8.25E-01$	$5.55E-03$	$1.02E-01$	$9.81E-02$
Minimum	$3.08E-01$	$1.62E-01$	$3.12E-04$	$1.90E-02$	$2.01E-02$

PCr: plasma creatinine; UCr: urinary creatinine; Uv: urinary volume; Ecc: endogenous creatinine clearance; CrCl: creatinine clearance.

580 nm, respectively, and using a water bath at 37°C (Sieger-Stern 6, Campo Mourão, Paraná, Brazil). All parameters of quality control were followed as described above.

2.8. Statistical Analysis. Statistical analysis was performed using Prism 4.0 software (GraphPad, La Jolla, CA, USA). The data were fist examined for nomality and comparison of the variances (Kolmogorov–Smirnov test or F-test). When the distribution was Gaussian the data were analyzed using a parametric test (paired t-test for two events, and Repeated Measures ANOVA with Tukey post-test for more than two events). In cases where the distribution was not Gaussian, nonparametric tests (Friedman test with Dunn's post-test for more than two events, and Wilcoxon matched pairs test for two events). Mann-Whitney test was used to test for differences between the duplicates by comparing the two methods, because the distribution was not Gaussian. The differences were considered significant when $P < 0.05$.

3. Results

Length and weight were measured in all 40 C57BL/6 mice at the start of the experiments. The mean ± standard deviation of weight and length is presented in Table 1. The BSA of each animal was calculated and an average factor (0.006179) was obtained, which was used for determination of creatinine clearance.

As shown in Table 2, the concentration of creatinine in plasma and urine and the volume of urine excreted in a period of 24 h varied markedly between the maximum and minimum levels, although not statistically significantly ($P > 0.05$).

A detailed standard procedure, which aimed to incorporate measures for internal quality control, such as acceptance adjustment or invalidation, was employed. Thus, we validated our analysis using the multirules of Westgard [10].

As depicted in Figure 1, none of the rules proposed by Westgard were violated for any of the parameters evaluated. The measurements of all 40 animals tested showed small variations in creatinine concentrations (Figure 1(a)), but the data fell within the average and standard deviation (mean [SD]: 1.18 [0.30] mg/dL). As shown in Figure 1(b), quantification of the concentrations of urea by the enzymatic colorimetric method (580 nm; mean [SD]: 35.5 [3.6] mg/dL) was performed with eight repetitions. For the analysis of urea concentration (Figure 1(c)), 20 plasma samples were quantified using the UV urea method (340 nm; mean [SD]: 29.8 [5.4] mg/dL) and the values fell within the average and standard deviation. Thus, altogether these data allowed us to assume that the results were within the limits of acceptance as described in the Westgard multirules [10].

In order to evaluate the effect of freeze-thawing on plasma urea concentration, the plasma samples were frozen at −20°C and thawed after 4 or 90 days after collection. As demonstrated in Figure 2, there was a significant decrease ($P < 0.05$) in the urea concentration of the thawed samples by 90 days after collection, as compared with the same samples thawed only 4 days after collection. This result demonstrated the importance of standardization and careful handling of biological samples in facilitating reliable determination of urea concentration.

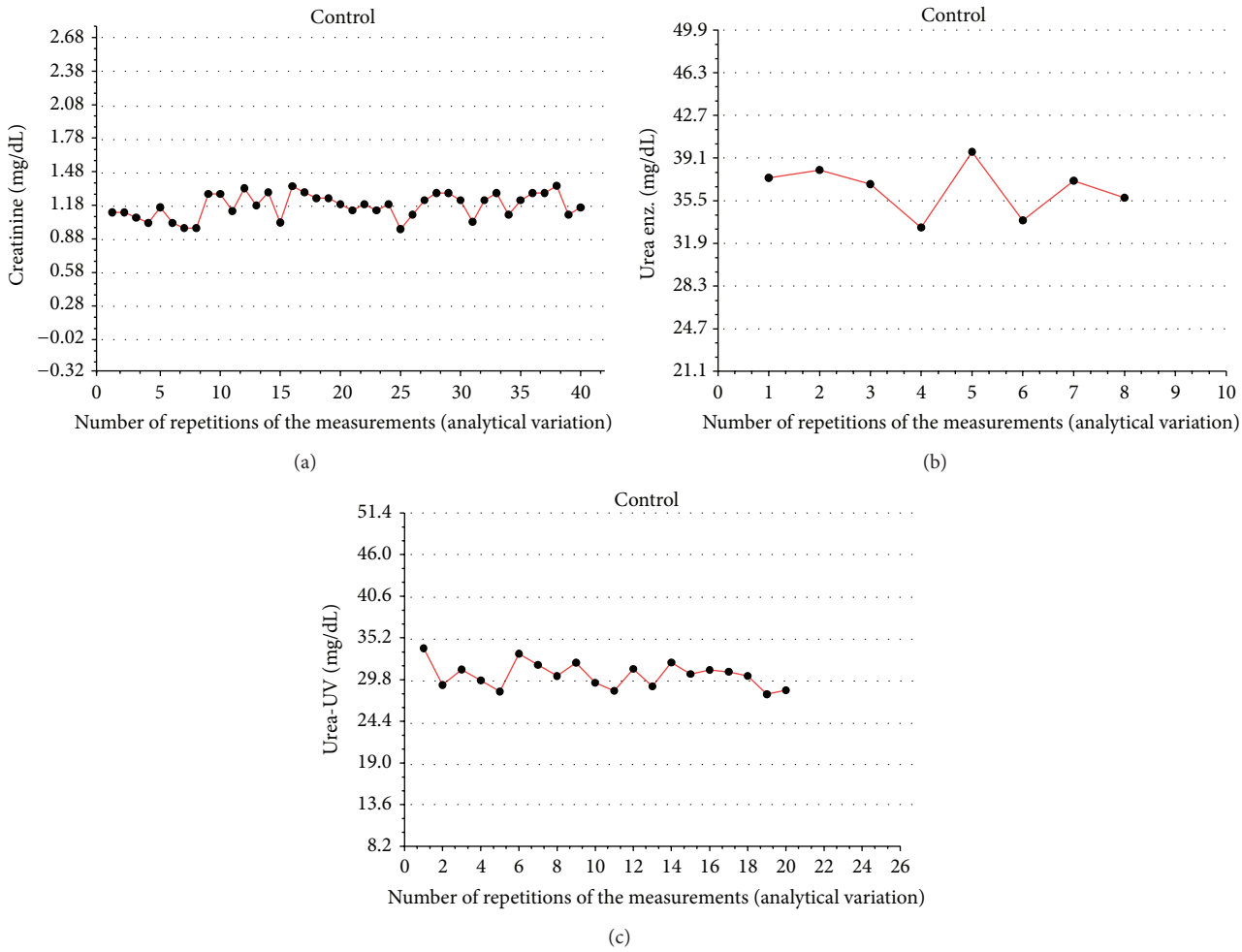

Figure 1: Levey-Jennings charts and evaluation of Westgard rules. The control samples were obtained from the biotechnical company and the variations (mean and standard deviation) were established and compared with those of the manufacturer, obtained from 20 different trials. After the collection and preparation of all biological samples, we inserted the control samples among the test samples, randomly, and quantified the concentrations of urea and creatinine by spectrophotometry. In (a), we evaluated the concentrations of creatinine by the colorimetric method (red-yellow), using picrate in an alkaline solution and reading at 500 nm, using 40 control points with an average of 1.18 and a 0.30 to 1 s deviation. In (b), we evaluated the concentrations of urea by the modified method of Berthelot (reading at 580 nm), using eight control points, with an average of 35.5 and a deviation of 3.60 to 1 s. In (c), we evaluated the concentrations of urea spectrophotometrically at 340 nm, using 20 control points, with an average of 29.8 and a deviation of 5.40 to 1 s. For statistical evaluation, we used the deviation distribution of samples (1 s, 2 s, and 3 s) as well as the Westgard rules.

After we investigated the variation in the analytical concentrations of urea with differences in the storage period, new measurements of the urea concentrations were made for different storage periods and storage temperatures. For this evaluation, samples were not frozen and thawed more than once, and we evaluated the samples immediately after collection (at room temperature). As shown in Figure 3, there were no significant differences in the urea concentration of blood or urine samples evaluated after different storage periods (0, 4, or 90 days after collection) or for different storage temperatures (room temperature, −20 or −70°C). Therefore, freezing is an important method of preservation, although standardization of standard operating procedures is still required in order to contribute to the reliability of the measurements, taking into consideration the analyte to be quantified.

After defining the best means for storage, we proceeded to assess two different commercial kits (absorbance read at 580 or 340 nm) as well as the variations between their duplicates (1st and 2nd absorbance reading of the same sample, using the same kit). Our results showed no differences between the duplicates using the same kit for both the enzymatic urea determination methods (reading at 580 nm or 340 nm; Figure 4(a)). However, after subtraction of the two absorbance readings (duplicates), for comparison of the two methods, we found significant differences, with a greater variation in the ultraviolet-based method (reading at 340 nm; Figure 4(b)). Thus, duplicate measurements favor

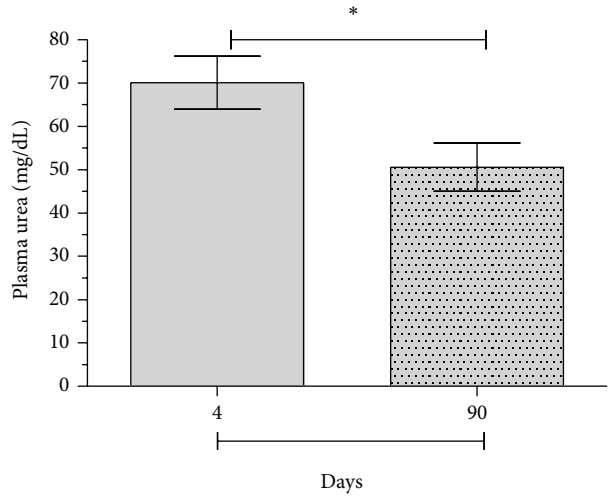

Figure 2: Influence of thawing on the measurement of plasma urea concentration. Blood was obtained from C57BL/6 mice for measurement of plasma urea. After centrifugation, the plasma was separated into tubes and frozen at −20°C for 4 days, followed by thawing and measurement of plasma urea by spectrophotometry. Samples were then again frozen at −20°C for 86 more days, when plasma urea was again evaluated. Values are expressed in mg/dL; (∗) statistically significant differences at $P < 0.05$.

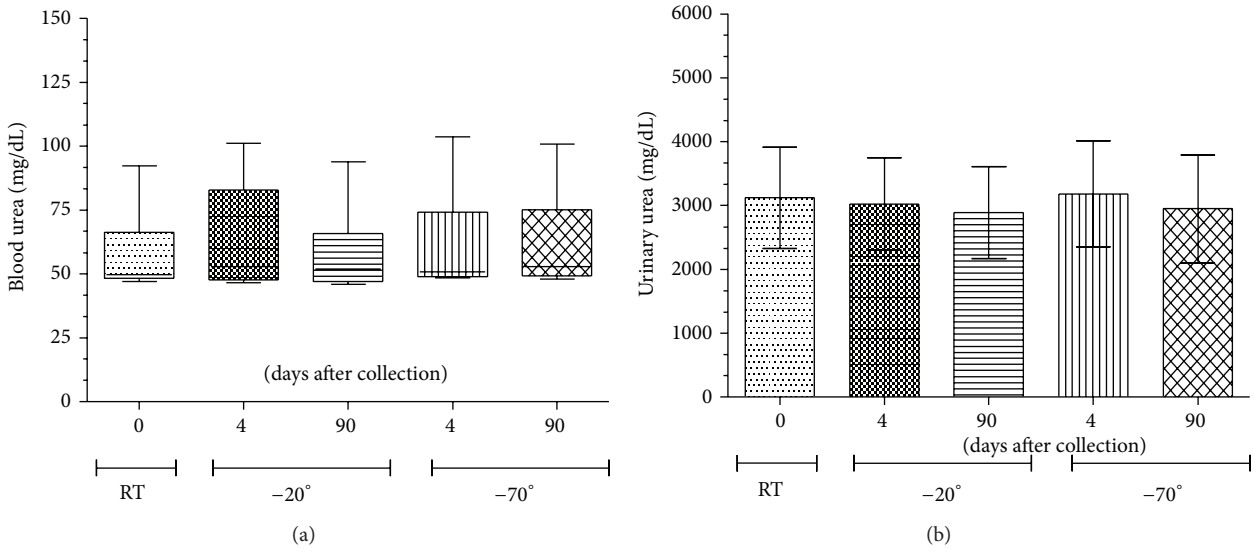

Figure 3: Influence of freezing on the quantification of plasma and urinary urea. Blood and urine were obtained from C57BL/6 mice and urea concentration was determined. Urine was obtained from mice maintained in metabolic cages for a period of 24 h. After urine collection, the blood was collected from the ophthalmic plexus. Both types of samples were centrifuged at 1831 ×g for 10 min and supernatants were divided into different aliquots. An initial evaluation of the samples was made at room temperature, before freezing, and further aliquots were frozen at −20°C or −70°C for 4 or 90 days, followed by quantification of the respective blood or urinary urea. In (a), we evaluated the concentrations of plasma urea by the colorimetric method (ultraviolet), following the time and temperature variations described above. In (b), we evaluated the concentrations of urinary urea at 24 h, using the same colorimetric method (ultraviolet) as for the plasma. Values are expressed in mg/dL. No significant differences at $P < 0.05$ were observed.

the accuracy of the evaluation of urea concentrations in the samples; but the ultraviolet method is more variable (Figure 4(c)).

4. Discussion

There is an increasing drive for researchers and laboratory services to guarantee accurate and reliable results in the analysis of patient as well as experimental animal samples [12]. When measuring kidney functional parameters, accurate assessment of biochemical changes in plasma and urine is essential. Yet, depending on the standard methodology, technique, origin, and quality of the samples used, the results may differ significantly, and therefore, measurements can be underestimated or overestimated [13]. In an attempt to reduce these variations, implementation of internal quality

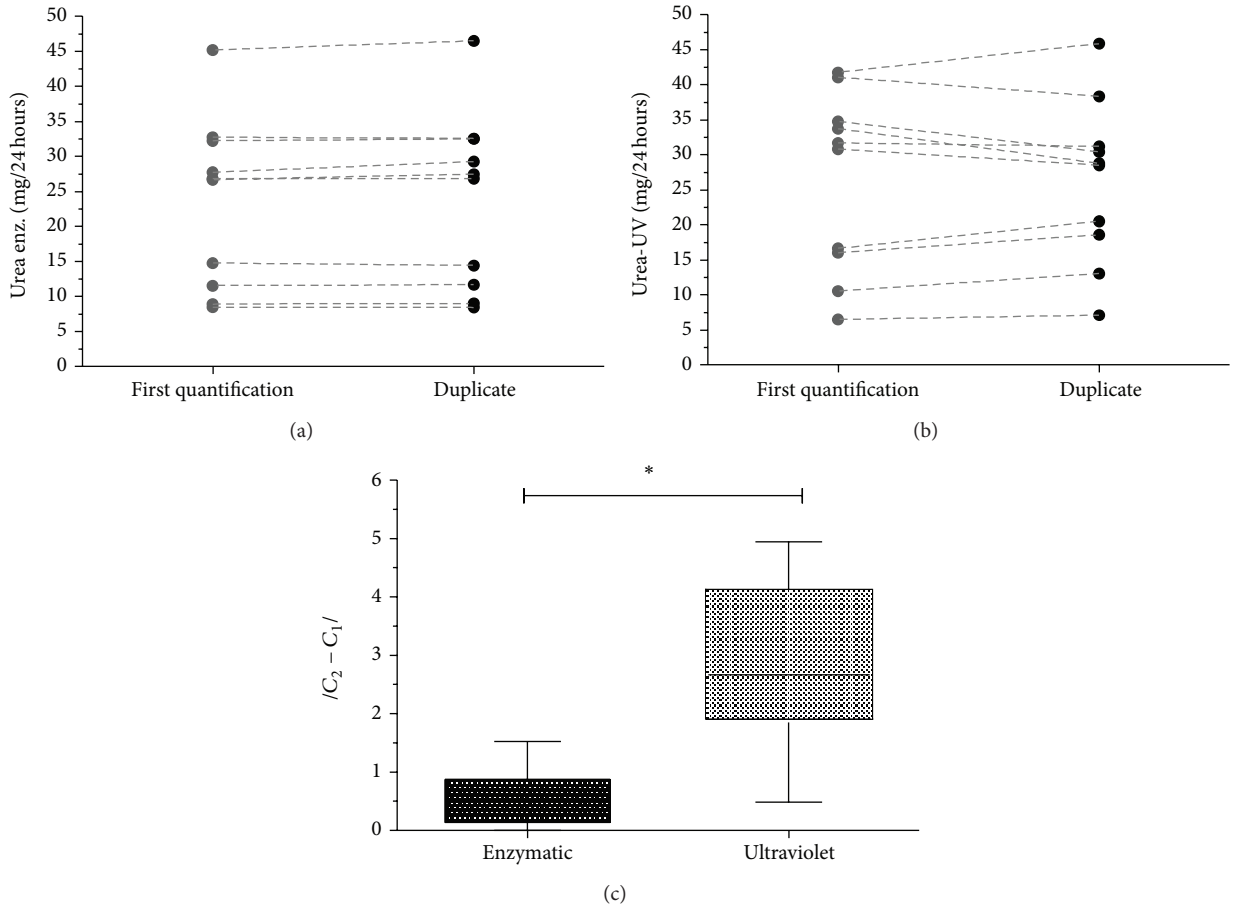

Figure 4: Methodological variation using duplicate samples. Urine was collected from C57BL/6 mice in metabolic cages for a period of 24 h. After centrifugation, the supernatant was removed for quantification of urea. The concentration of urea in the samples was quantified in duplicate, for each of two different methods, namely, the kinetic ultraviolet approach (kinetic reaction involving two time-points) and a colorimetric approach, using a fixed time period. (a) Assessment of the urea concentration in duplicate samples, measured by the enzymatic colorimetric method. (b) Assessment of the concentrations of urea in duplicate, measured by the ultraviolet method. (c) Evaluation of the differences between the duplicates by comparison of the two methodologies. The concentrations were expressed as mg per 24 h. Differences were considered significant when $P < 0.05$ (∗).

control procedures is crucial for ensuring accurate and reliable measurement of the analytes. Thus, choosing a good combination of decision criteria (control rules) to include in the quality control is essential for decreasing the inaccuracy of the analytical approach used.

In an attempt to better assess the renal function of mice, we here evaluated creatinine clearance, considering an average factor calculated from the BSA (determined from the weight and length of these animals) and used the Westgard rules [10] as a control strategy and the Levey-Jennings charts [14] to represent the data for each sample collection day. Although this approach has not been used much for murine samples, this strategy has already been adopted for reducing errors in the analysis of human and veterinary samples and has been used as an internal quality control for both a variety of samples and types of analyses [15–17].

As shown in Table 1, we evaluated the mean, standard deviation, and coefficient of variation in the length and weight of the mice, and from these data, we calculated the BSA and obtained an average factor of 0.006179. The results showed that when using the average factor to calculate creatinine clearance or urea, the values did not differ significantly. Thus, when we validated the data using the Westgard rules, none of the rules of quality control were rejected. Moreover, our data indicated that the urea and creatinine clearance measurements in mice should be adjusted to BSA as calculated based on the weight and length of these animals, to ensure that no systematic or random errors occur. Therefore, the results would be more precise and accurate than those evaluated without applying this internal quality control.

Concerning the effect of thawing on plasma urea concentration, we demonstrated that repeated freeze-thawing cycles affect the urea concentration in mouse samples. On the other hand, samples frozen at −20 or −70°C for 4 or 90 days, consecutively, showed no differences in the concentrations of plasma or blood urea. These results indicated that freeze-thawing cycles appear to be more problematic than long-term storage at −20 or −70°C in terms of sample maintenance.

The effects of freeze-thawing have been shown mainly in samples obtained from humans, nonhuman primates, and laboratory animals, such as rats and dogs [18–21]; however, controlled studies of the effects on mouse samples are in their infancy. According to Reynolds et al. [18], no clinically relevant changes are observed in different aliquots of canine plasma for all constituents, including urea and creatinine. Similar insignificant changes have been observed in cholesterol levels in baboon serum [22] and in cholesterol, micronutrients, and hormones in human plasma and serum samples [23]. However, Kale et al. [20] evaluated the effect of freeze-thawing on 18 different biochemical parameters of rat serum and showed that four of these were altered. In addition, a recent study also showed that after 90 days or 10 rounds of freeze-thawing, analytes such as glucose, creatinine, cholesterol, and triglycerides remain unchanged, but that concentrations of blood urea nitrogen, uric acid, lactate dehydrogenase, and so forth, changed significantly [21]. It is noteworthy that most of these studies had evaluated samples obtained from dogs, baboons, and humans only a few days after collection. In our case, the samples were evaluated within 90 days of collection, a storage period typical for research laboratories that need to collect a large number of samples before commencing biochemical evaluations. The fact that storage of our samples for 4 versus 90 days at −20 or −70°C did not result in significant differences in plasma or urine urea concentrations may suggest that the biggest problem arises from the repeated freezing and thawing of samples.

Thus, storage, freeze-thawing, and the use of internal quality controls are important steps in the preanalytical phase of laboratory testing and, depending on the implementation of these steps, the measurements of biochemical parameters may change considerably [21, 24].

With regard to variations between enzymatic and colorimetric methods for quantification of urea, we demonstrated that, although there were no differences between duplicate samples when using the same commercial kit, comparison of the subtracted values (between the two duplicates) revealed that the absorbance reading at 340 nm (ultraviolet method) presented greater variability in individual samples. Thus, our data indicated that the measurement of urea concentration is more reproducible when carried out by the enzymatic method.

5. Conclusions

Taken together, our results demonstrated that measurement of renal biochemical parameters in mice, such as urea and creatinine, can be measured with great accuracy when taking into consideration a factor calculated from the BSA. Moreover, repeated freeze-thawing cycles may induce important variations in the urea concentration. Additionally, the enzymatic method results in less variability in sample readings than does the ultraviolet method. Thus, we suggest that measurement of renal parameters need to be standardized and that samples, whether for laboratory testing or scientific research, must be appropriately handled prior to analysis.

Conflict of Interests

The authors declare that there is no conflict of interests regarding the publication of this paper.

Authors' Contribution

Wellington Francisco Rodrigues and Camila Botelho Miguel contributed equally to this work.

Acknowledgments

This work was supported by the Coordenação de Aperfeiçoamento de Pessoal de Nível Superior (CAPES), Fundação de Amparo à Pesquisa do Estado de Minas Gerais (FAPEMIG—rede mineira—20/12), and Conselho Nacional de Desenvolvimento Científico e Tecnológico (CNPq).

References

[1] M. Jaffe, "Ueber den Niederschlag, welchen Pikrinsäure im normalen Harn erzeugt und über eine neue Reaction des Kreatinins," *Zeitschrift fur Physiologische Chemie*, vol. 10, pp. 391–400, 1886.

[2] R. Bellomo, S. Bagshaw, C. Langenberg et al., "Pre-renal azotemia: a flawed paradigm in critically ill septic patients?" *Contributions to Nephrology*, vol. 156, pp. 1–9, 2007.

[3] K. Jung, C. Wesslau, F. Priem et al., "A. Specific creatinine determination in laboratory animals using the new enzymatic test kit, "Creatinine-PAP"," *Journal of Clinical Chemistry and Clinical Biochemistry*, vol. 25, no. 6, pp. 357–361, 1987.

[4] B. Kågedal and B. Olsson, "Determination of creatinine in serum by high-performance liquid chromatography: a comparison of three ion-exchange methods," *Journal of Chromatography*, vol. 527, no. 1, pp. 21–30, 1990.

[5] P. Yuen, S. Dunn, T. Miyaji et al., "A simplified method for HPLC determination of creatinine in mouse serum," *The American Journal of Physiology—Renal Physiology*, vol. 286, no. 6, pp. F1116–F1119, 2004.

[6] M. Palm and A. Lundblad, "Creatinine concentration in plasma from dog, rat, and mouse: a comparison of 3 different methods," *Veterinary Clinical Pathology*, vol. 34, no. 3, pp. 232–236, 2005.

[7] J. G. Donnelly, S. J. Soldin, D. A. Nealon et al., "Stability of twenty-five analytes in human serum at 22 degrees C, 4 degrees C, and -20 degrees C," *Pediatric Pathology & Laboratory Medicine*, vol. 15, no. 6, pp. 869–874.

[8] J. E. Logan, "The use of urograph for the determination of urea nitrogen concentration in serum and plasma," *Canadian Medical Association Journal*, vol. 89, no. 8, pp. 341–344, 1963.

[9] R. J. Henry and M. Segalove, "The running of standards in clinical chemistry and the use of the control chart," *Journal of Clinical Pathology*, vol. 5, no. 4, pp. 305–311, 1952.

[10] J. O. Westgard, P. L. Barry, M. R. Hunt, and T. Groth, "A multirule Shewhart chart for quality control in clinical chemistry," *Clinical Chemistry*, vol. 27, pp. 493–501, 1981.

[11] D. Du Bois and E. F. Du Bois, "A formula to estimate the approximate surface area if height and weight be known," *Archives of Internal Medicine*, vol. 17, pp. 863–871, 1916.

[12] C. D. Schons and R. G. Tavares, "Proposal for the use of a pool of whole blood as internal quality control in hematology," *Jornal*

Brasileiro de Patologia e Medicina Laboratorial, vol. 46, no. 3, pp. 181–186, 2010.

[13] P. Bonini, M. Plebani, F. Ceriotti, and F. Rubboli, "Errors in laboratory medicine," *Clinical Chemistry*, vol. 48, no. 5, pp. 691–698, 2002.

[14] S. Levey and E. R. Jennings, "The use of control charts in the clinical laboratory," *American Journal of Clinical Pathology*, vol. 20, no. 11, pp. 1059–1066, 1950.

[15] S. C. Hollensead, W. B. Lockwood, and R. J. Elin, "Errors in pathology and laboratory medicine: consequences and prevention," *Journal of Surgical Oncology*, vol. 88, no. 3, pp. 161–181, 2004.

[16] S. L. Liang, M. T. Lin, M. J. Hafez et al., "Application of traditional clinical pathology quality control techniques to molecular pathology," *Journal of Molecular Diagnostics*, vol. 10, no. 2, pp. 142–146, 2008.

[17] M. Waterhouse, R. Kunzmann, M. Torres, H. Bertz, and J. Finke, "An internal validation approach and quality control on hematopoietic chimerism testing after allogeneic hematopoietic cell transplantation," *Clinical Chemistry and Laboratory Medicine*, vol. 51, no. 2, pp. 363–369, 2013.

[18] B. Reynolds, B. Taillade, C. Médaille et al., "Effect of repeated freeze-thaw cycles on routine plasma biochemical constituents in canine plasma," *Veterinary Clinical Pathology*, vol. 35, no. 3, pp. 339–340, 2006.

[19] M. Plebani, "Exploring the iceberg of errors in laboratory medicine," *Clinica Chimica Acta*, vol. 404, no. 1, pp. 16–23, 2009.

[20] V. P. Kale, S. G. Patel, P. S. Gunjal et al., "Effect of repeated freezing and thawing on 18 clinical chemistry analytes in rat serum," *Journal of the American Association for Laboratory Animal Science*, vol. 51, no. 4, pp. 475–478, 2012.

[21] S. Cuhadar, M. Koseoglu, A. Atay, and A. Dirican, "The effect of storage time and freeze-thaw cycles on the stability of serum samples," *Biochemia Medica*, vol. 23, no. 1, pp. 70–77, 2013.

[22] C. Jennings, D. M. Weaver, and A. W. Kruski, "Effects of freeze-thawing on determinations of cholesterol and high-density lipoproteins in baboon sera," *Clinical Chemistry*, vol. 25, no. 3, p. 490, 1979.

[23] G. W. Comstock, A. E. Burke, E. P. Norkus, G. B. Gordon, S. C. Hoffman, and K. J. Helzlsouer, "Effects of repeated freeze-thaw cycles on concentrations of cholesterol, micronutrients, and hormones in human plasma and serum," *Clinical Chemistry*, vol. 47, no. 1, pp. 139–142, 2001.

[24] A. Simundic and G. Lippi, "Preanalytical phase—a continuous challenge for laboratory professionals," *Biochemia Medica*, vol. 22, no. 2, pp. 145–149, 2012.